A Framework to Simulate and Improve Terahertz Quantum Well Photodetectors

by

Simon Ferré

A thesis
presented to the University of Waterloo
in fulfillment of the
thesis requirement for the degree of
Master of Applied Science
in
Electrical and Computer Engineering

Waterloo, Ontario, Canada, 2013

© Simon Ferré 2013

I hereby declare that I am the sole author of this thesis. This is a true copy of the thesis, including any required final revisions, as accepted by my examiners.

I understand that my thesis may be made electronically available to the public.

Abstract

A wide range of applications have been recognized for terahertz radiations. In fact, medical imaging, homeland security screening, very high-speed wireless telecommunications systems and even drug and gas detection are boosting the development of terahertz emitters and receivers. The work of this thesis is among the efforts in that regard.

Actual terahertz detectors are suffering many drawbacks, they are bulky, very slow, not very sensitive or operates at non-practical temperatures. Combined with the complexity to realize terahertz emitters, it explains the difficulties of terahertz radiations to ensure market penetration with practicable civil applications. In that regard, we aim to better understand and improve a specific terahertz photodetector: the Terahertz Quantum Well Photodetector. Those devices working principle relies on a photocurrent created by the excitation of electrons from ground states of quantum wells to the continuum under terahertz impinging light. The intensity of the photocurrent is depending on the intensity of the radiation received by the device.

The device active region is made of a multiple quantum wells $GaAs/Al_xGa_{1-x}As$ system. By changing the design of the device, that is the thicknesses of each layer, the aluminum fraction of the doping concentration, we can modify its performances. Documented and commented Matlab functions and routines have been implemented in order to simulate a given structure and scripts have been written to find the optimum parameters for a target absorption frequency. Our model has been verified by comparison with experimental data reported in the literature.

Based on our model, we systematically study the impact of the active region and contact parameters on the device performances. In addition, innovative designs are proposed in order to reduce the undesirable dark current and thus increase the detectivity. They benefits from many-body effects, effects that are usually a constraint on the design. To our knowledge this is the first time those effects are used to realize innovative designs and increase the performances of quantum well infrared photodetectors.

Finally we expose other designs that have been tested in the infrared domain with QWIP and adapt them to the terahertz range. In particular, we propose a quantum cascade photodetector, a double barrier bound-to-miniband and a phonon-assisted band to miniband structures.

Acknowledgements

I would like to thank Drs Paul Friedel and Catherine Rosenberg for advising me to enroll to the University of Waterloo. Without them, I would not have had this opportunity.

This work would not have been possible without the guidance and support and my supervisor Dr Dayan Ban. I want to express to him my gratitude.

I would like to express my deepest appreciation for my committee and the readers of this thesis, Drs Zbig Wasilewski and Irene Goldthorpe.

For the knowledge I gained by taking their courses, I would like to deeply thank Dr Russell Thompson, for his passionate course on Solid State Physics, Dr Hany Aziz, for introducing me to the beauty of organic devices, Dr Karim Karim, for his meaningful explanation on displays and again Dr Dayan Ban and Irene Goldthorpe for their lectures on optoelectronic and modern transistors.

My deepest gratitude goes to the Electrical and Computer Engineering staff of the University of Waterloo, with special mention for Ken Gosselink for his gigantic help for moving to QNC.

I wish to thank all the students I get a chance to teach. It has been my pleasure to be your teacher assistant, you made this experience very enjoyable and interesting.

This works would not have been possible without the help and support of the other student of our group. Ghasem I would like to thank you, this work would not have been possible without you. I will miss our discussions whether on deep theoretical derivations or Farsi 101, Mersi. Chao I thank you for bearing me as an office mate for the length of this master and our helpful discussions about experimental setups. Mark, I express my gratitude to you for your expertise as regards fabrication of devices and sci-fi literature, may you write many novels. Nolan, thank you for the realization of the mechanical pieces and teaching me how to use a milling machine without fear. My gratitude also goes to the other members, past and present, or our group, that I did not have the opportunity to interact with as much as I would have had. Rudra, Alex, Eric, Jason, David, thank you. I especially express my gratitude to Dr Saeed Fathololoumi for representing me at CLEO

2013.

Many thank to all my friends at the University of Waterloo and abroad who have been a key support during my stay here. I will not take the risk to forget anybody by mentioning names. Thank you, mersi, muchas gracías, merci à tous.

Last but not least, I owe my thesis to my family, Grégoire, Juliette, Papa, Maman, thank you for all your support throughout all those years and to my girlfriend Céline. I can not write how much I thank you for everything.

Dedication

This is dedicated to Solange.

Table of Contents

List of Tables x

List of Figures xi

1 Introduction 1

1.1 Motivation and Objectives . . . 1

1.2 Imaging experiment . . . 4

1.3 Literature Review . . . 6

1.3.1 Terahertz detectors . . . 7

1.3.2 Quantum Well Photodetectors . . . 9

1.4 Thesis Overview . . . 14

2 Quantum Well Photodetector design 15

2.1 QWP mechanisms . . . 15

2.2 Active Region Model . . . 17

2.2.1 Structure parameters . . . 17

2.2.2 Energy state and wavefunction calculation . . . 19

2.2.3 Many-body effect . . . 20

2.3 Optical Coupling . . . 22

2.3.1 Polarization Rule . . . 22

2.3.2 Coupling structures . . . 23

2.4 Top Metal Coverage 24
2.5 Figures of merit 27
2.5.1 Absorption 27
2.5.2 Dark Current 29
2.5.3 Photocurrent 31
2.5.4 Macroscopic figures of merit: Responsivity and Detectivity 33

3 Simulation results **37**
3.1 Device Optimization 37
3.1.1 Well width 37
3.1.2 Barrier width 40
3.1.3 Operating temperature 42
3.2 New Designs 45
3.2.1 Potential calculation 45
3.2.2 Absorption spectrum 46
3.2.3 Transmission probability of the barrier 49
3.2.4 Dark current 51
3.3 Limits of bound-to-quasibound QWP and future designs 52
3.3.1 Very low frequency QWPs 52
3.3.2 New designs 54

4 Conclusion and future work **58**

APPENDICES **61**

A Imaging experiments **62**
A.1 Transmission mode 62
A.2 Reflection mode 63

B Transmission Coefficient Derivation in the WKB approximation **65**
B.1 Square barrier . . . 65
B.2 Arbitrary barrier . . . 66

C Interferences phenomenon in the active region **68**
C.1 Power density of the electric field growth axis component . . . 68
C.2 Interpretation . . . 69

D Fabrication **71**
D.1 Fabrication and packaging . . . 71
D.2 Mask . . . 75
D.3 Process sheet . . . 76

References **80**

List of Tables

1.1 Thermal detectors review 7
1.2 Photoconductive detectors review 8

2.1 WKB approximation of D(E) 31

3.1 Studied designs, $N_{2D} = 4 \times 10^{10}\, cm^{-2}$ for all devices 45

List of Figures

1.1 Wave terminology as regards their frequency and wavelength 1
1.2 Luminance of the sun (5750K) 2
1.3 Luminance at 36, 20 and 0°C 2
1.4 Available sources in and around the THz range. Novel devices under research are represented in ovals. Picture from[1] 3
1.5 Imaging experiment setup 5
1.6 Bank note in the visible (left) and the THz (right) range 5
1.7 Bound-to-bound 10
1.8 Bound-to-continuum 10
1.9 Miniband-to-miniband, graded collector 10
1.10 Miniband-to-Miniband, square collector 10
1.11 Bound-to-miniband 11
1.12 Bound-to-miniband, stepped 11
1.13 Four zone QWIP 11
1.14 Active region of a Quantum Cascade Detector 12

2.1 Structure of one QWP device. 15
2.2 Detail of the active region. 16
2.3 Two possible configuration for the optical transition. 17
2.4 Example of potential and wavefunctions calculated with the TM method. The wavefunctions are offset for more clarity. 20

2.5 45° facet configuration resulting in a standing wave. 25
2.6 Power density for an infrared and a terahertz QWP, the modules are represented in dashed green. 26
2.7 Dark current mechanisms in a QWP. 30
2.8 Evolution of the photocurrent with the capture probability for different absorptions. 33

3.1 Optimum well width without and including MBE. Absorption frequency is indicated without (black) and including corrections (red). Doping is 4×10^{10} cm^{-2}. 38
3.2 Evolution of Hartree, exchange-correlation potentials amplitude and depolarization shift with doping. Inset: Peak absorption frequency without MBE and with MBE for each fraction of Aluminum and different doping concentration. 39
3.3 Potential and wavefunctions with (solid lines) and without (dashed lines) taking into account the MBEs. 40
3.4 dark current density and it tunneling component for barrier thickness varying from 400Å to 1000Å with a step of 100Å. 41
3.5 Tunneling and thermionic components of the dark current for a temperature dependant and a constant mobility for temperatures varying from 7K (black) to 20K (red) with a 1K step. 42
3.6 Evolution of the detectivity with cut-off frequency for temperatures varying from 5 to 20 K with a 1 K step. 43
3.7 Evolution of the 3D thermally activated electron density above the barrier with cut-off frequency for temperatures varying from 5 to 20 K with a 1 K step. 43
3.8 Density of carriers in the continuum excited by the background photons (red) and responsible of the device dark current (blue). 44
3.9 Potential of the ideal design. 46
3.10 Potential of the design S01. 46
3.11 Potential of the design S02. 46
3.12 Potential of the design S03. 46

3.13 Spectra of absorption of each structure at $1.5 \times 10^4\,\mathrm{V.m^{-1}}$. 47
3.14 Peak absorption frequency evolution with the applied electric field. 47
3.15 Evolution of the absorption with the electric field for each studied structure. 47
3.16 Comparison between the theoretical (solid red) and numerical (blue circle) calculation of the transmission coefficient with the WKB approximation (left side). The difference is represented in solid black with the right axis. . . . 49
3.17 Comparison between the transmission coefficients numerically calculated with the WKB approximation for the proposed designs. 50
3.18 Total and tunneling part of dark current at 7K. By shifting the doping, we decrease the dark current by one order of magnitude. 52
3.19 Potentials calculated for the design presented in the text box, without including the MBEs (blue) and with them, doping being either in the center of the well (red) or in the barrier (black). 54
3.20 Quantum cascade detector in the terahertz range. 56
3.21 Band diagram of a bound-to-miniband THz QWP representing the energy states. 56
3.22 Band diagram of a bound-to-miniband THz QWP representing the wavefunctions. 56
3.23 Phonon-assisted band to miniband detector in the terahertz range. 57

A.1 20 euros banknote in transmission mode 62
A.2 50 Canadian dollars banknote in transmission mode 62
A.3 2 Argentinian pesos banknote in transmission mode 63
A.4 10 pesos Argentinian pesos banknote in transmission mode 63
A.5 Imaging experiments setup in reflection mode 64
A.6 Imaging experiments in reflection mode with a 1 Canadian dollar coin . . . 64

B.1 Square potential barrier and wavefunctions corresponding to each region . 65
B.2 Discretization of the potential barrier for an arbitrary shape 66

C.1 Variation of the power density through the device, $z = 0$ being the top contact 70

D.1 Disposition of the devices in one bar 71
D.2 Fabrication steps 72
D.3 Alignment mark after etching 73
D.4 Alignment mark after etching 73
D.5 Packaging steps 73
D.6 Position of the cold finger and device in the cryostat 74
D.7 Top view of the cold fingers used for QWP characterization 75
D.8 Mask used for the fabrication 76

Chapter 1

Introduction

1.1 Motivation and Objectives

The maximum spectral luminance of the sun is between 400 and 800 nm. In addition the atmosphere is transparent at those wavelength. The correlation of this two facts explains why the human eye is mainly sensitive to those specific radiations, that we therefore called "visible light". Nevertheless, it represents only a very small part of the wavelengths that are used in our lives. Figure 1.1 reminds the relative frequencies and terminology for usual radiations in photonics and electronics as well as the visible light range.

The link between the radiation emitted by one object and its temperature can be

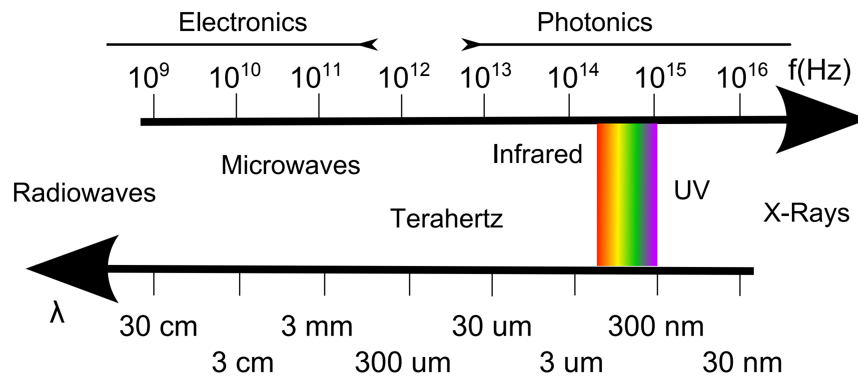

Figure 1.1: Wave terminology as regards their frequency and wavelength

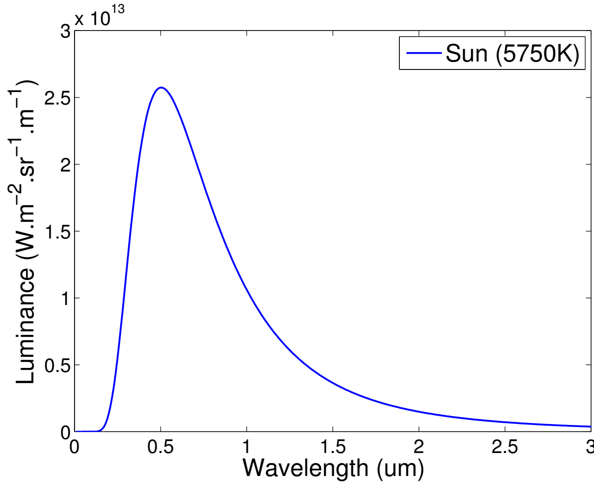

Figure 1.2: Luminance of the sun (5750K)

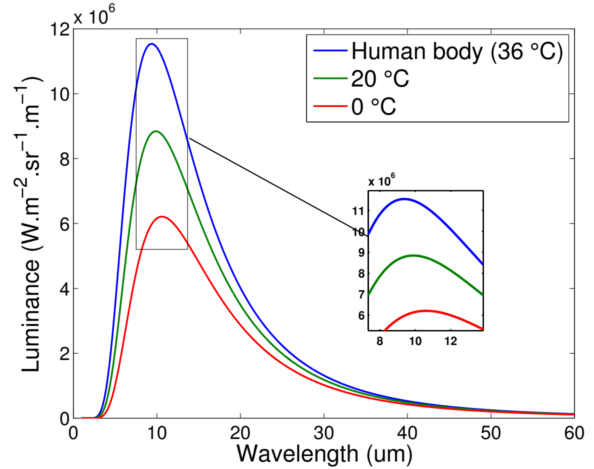

Figure 1.3: Luminance at 36, 20 and 0°C

described in a first approximation by the black body model, introduced by Kirchhoff in 1860. Figure 1.2 shows the luminance of the sun and figure 1.3 of objects at usual temperatures (0°C, 20°C and the human body temperature of 36°C). In fact, if we assume that the sun's temperature on its surface is 5750K, the maximum emitted wavelength is $\lambda_{max} = \dfrac{2.898 \times 10^{-3}}{T} = 504$ nm according to Wien's law, as we can see on figure 1.2. This confirms our previous discussion about the human eye sensitivity. Figure 1.3 displays the luminance for the human body (at 38°C) and environment at 20°C and 0°C. The wavelength corresponding to this temperature interval is around 9 to 10 μm. This has been one of the main reason for the research investment in the mid-infrared range, especially between 8 and 12 μm. Indeed thermal radiation detection promised many applications from military to civil domain like night vision[2], industrial component inspection[3], pedestrian tracking[4] or physiological activities monitoring[5].

Nevertheless, terahertz (THz) radiation has been forsaken for a long time. This frequency range is loosely defined as $\mathrm{f} = 0.3 - 30\,\mathrm{THz}$, equivalently $\lambda = 1000 - 10\,\mu\mathrm{m}$ in wavelength or $\mathrm{E} \approx 4 - 40\,\mathrm{meV}$ in energy. This is mainly due to the fact that it is not very present in natural events and usual technologies: it is far from the frequencies of visible light, usual photonics devices or electronics clock speeds. Frequencies below the THz range are mainly generated with semi-conductor based electronic devices and higher frequencies with photonics devices. Then, the development of terahertz waves emission, amplification and detection devices has not been explored until recently. Figure 1.4 highlights the lake of

practical devices between the electronics (up to 300 GHz) and photonics (down to 30 THz), the so-called terahertz gap. Indeed, every component has its own drawbacks: photomixers

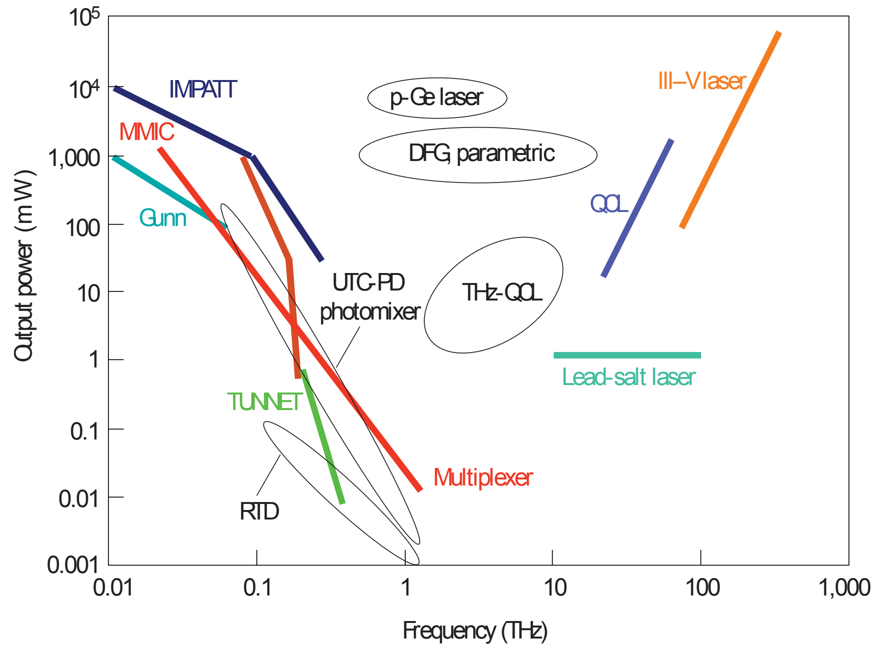

Figure 1.4: Available sources in and around the THz range. Novel devices under research are represented in ovals. Picture from[1]

suffer of very low output powers beyond 1 THz (in the order of μW), p-Ge laser is working in pulsed mode, free electron and gas lasers are bulky, Quantum Cascade Lasers operate at cryogenic temperatures, ...

Nevertheless, the development of THz will tackle various issues. First, to fill the THz gap raises many interesting challenges from the research point-of-view as regards theoretical modeling, fabrication technologies or characterization. Secondly, technological breakthroughs in the THz range will not only complete the already existing applications but also boost utterly new industrial outlets. A road map of THz applications has been established by Tonouchi[1]. As an example, research is pursued in the fields of medicine and biological (tumor imaging, non-destructive diagnosis, pharmacology, ...)[6, 7, 8] or industrial (wafer and LSI inspection, gas sensing)[9]. In addition to those applications usual in the infrared range, we can cite more innovative applications like open-space telecommunications[10], food control, drug detection and security screening[11]. Many chemical compounds and gases have characteristic rotational and vibrational absorption spectrum in the THz range, explaining that the first application for THz wave have been spectroscopy. The oldest use

of THz spectroscopy has been for spatial application, to identify the radiations received from space[12]. In fact, estimations have been made that an important part of the photons generated by the Big Bang fall into the THz domain[13]. Furthermore, some material are transparent in the THz range whereas they are opaque in the visible or infrared range leading to great application in imaging, called T-Ray by analogy with X-Ray imaging. To illustrate those new imaging possibilities, we led imaging experiments in transmission mode with different objects. They are described in section 1.2.

In addition, THz open-space telecommunications has been demonstrated for both audio and video[14] signals. It has been shown that even if an obstacle is in the signal path, the communication can still take place as long as this obstacle material does not entirely absorb THz radiations. In addition, higher band rate of 100 Gbps are expected in the short-run for both indoor and outdoor communications, which is much higher compared to usual microwave wireless system. Nevertheless, terahertz range faces a major problem: it is importantly absorbed by atmosphere, especially water, thus compromising long-distance open-space communications and experiments. As a result, terahertz is also studied in the scope of spatial applications, as there is no atmosphere in space, such as spectroscopy[15]. Many applications have been listed in Saeedkia's handbook[16] such as tomographic imaging, applications in the aerospace, wood, pharmaceutical and semiconductor industry as well as in art conservation.

1.2 Imaging experiment

In order to demonstrate the potential of terahertz radiations we realized a THz imaging setup. A THz Quantum Cascade Laser (QCL) emits THz radiations that are focused by a lens to a micro-bolometer THz camera. In fact, THz beam is very divergent and need to be focus by putting a lens at a focal distance from the QCL facet. The set up is described in figure 1.5 The QCL is emitting at 3 THz and is cooled down at 10K. The camera is the IRXCAM-THz developed by INO and is made up of a 160×120 pixels micro-bolometer Focal Plane Array (FPA)[17] optimized for 3 THz. Several objects have been studied in transmission mode. In fact, we studied hidden pictures in bank notes from different countries (Canadian dollars, euros, Argentinian pesos). Euro banknotes are made of cotton fiber, Canadian dollars of synthetic polymer (new banknotes) and Argentinian pesos of flax and cotton fibers. For example, we have been able to reveal concealed euro symbols, faces, building and numbers as shown on figure 1.6. Polymer banknotes turned out to yield better quality pictures.

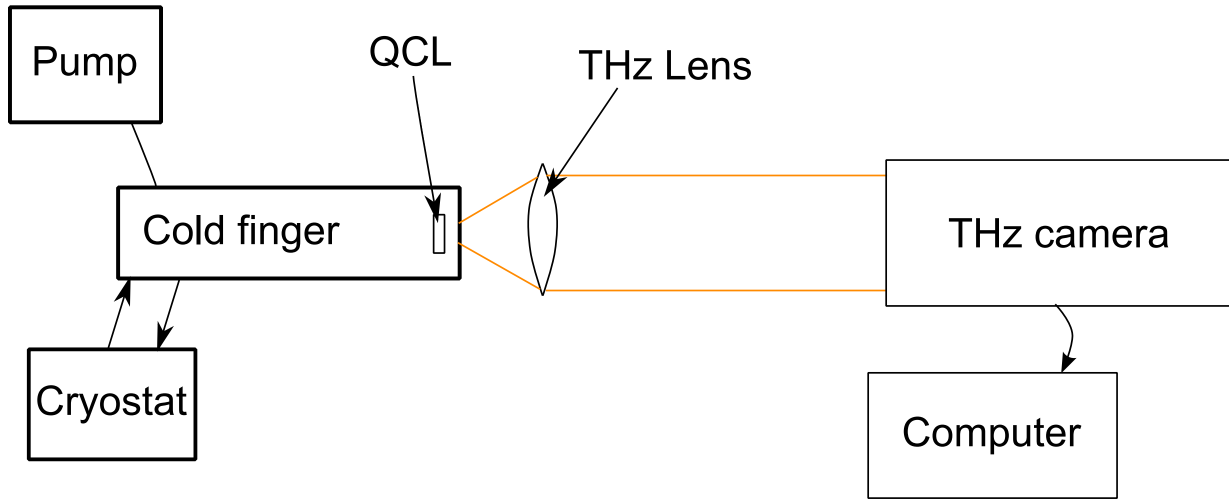

Figure 1.5: Imaging experiment setup

Results with the other banknotes are presented in appendix A. Similarly to infrared

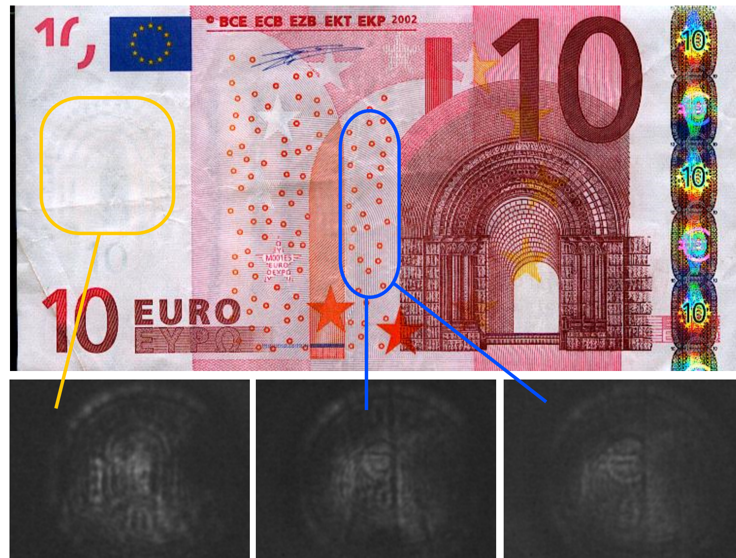

Figure 1.6: Bank note in the visible (left) and the THz (right) range

and ultraviolet ink, we can imagine to produce terahertz ink in order to limit banknote counterfeit.
In addition to this transmission mode setup, we also studied the possibility to realize

reflection mode imaging. To do so, the sample to image is placed after the lens, at 45° with the terahertz beam and the camera is moved to also be at 45° with the coin. The setup and an example of resulting image are shown respectively in figures A.5 and A.6 of appendix A.
We estimated the resolution of our system by measuring the smallest element that we could resolve in a repeatable way. We found it to be between 165 and 200 μm. Resolution broke down below 150 μm.

1.3 Literature Review

In this section, we review the main sensors used to detect terahertz radiations and quantum well photodetectors structures. Detectors are transducers that are characterized by interdependent parameters:

- the *band of response*. It is the spectral range for which the detector returns a signal. Depending on the application, either a wide or a very sharp spectrum can be desired.
- the *responsivity*. Most detectors produce an electrical signal under enlightenment, the responsivity is translating the current (or voltage) response per unit optical incident power: $R_\lambda = \Delta I / P_{opt}$. This parameters is to be maximized. The responsivity and detectivity derivations and deeper meanings will be given in section 2.5.4.
- the *response speed*. A common quantitative figure of merit for the speed of response is the time constant. It is the time taken by the signal to rise up to 63% of its maximum value. A definition with the falling time is also often encountered. The time rise is another parameter representative of the speed of response. It is the time needed to rise from 10% to 90% of the signal maximum value.
- the *noise* level. Noise can result from many different physical effects (Johnson-Nyquist noise, shot noise, Flicker noise). An exhaustive review of all those effects is behind the scope of this thesis. The noise is to be kept as low as possible.
- the *dimension* of the detectors. The physical dimensions of the device are a crucial parameter for some applications (spatial, portable sensors, ...). The sensitive area of the detector is also of importance.
- the *operating temperature*. This is a crucial parameter as it dictates the cooling system required to use the device. We can distinguish the detectors operating at room

temperature ($T > 300K$), at thermoelectric coolers temperature ($T > 240K$), at liquid nitrogen temperature ($T > 77K$) and at liquid helium temperature ($T > 4K$).

- the *cost*. The production and utilization cost will determine the market targeted by the detector.

We will explain how to quantitatively estimate the spectral response, the responsivity, the noise induced by the dark current as well as the operating temperature in chapter 2.

1.3.1 Terahertz detectors

As mentioned in section 1, Terahertz radiations have been a dynamic topic of research in the late decade. In fact, the conquest of this frequency range is supported by both scientific (fill the gap between electronics and photonics) and industrial motivations. We have seen that

We can sort terahertz detectors in subcategories depending on their operating principle:

Detector	Temperature	Response time	NEP ($W/\sqrt{Hz}$)	Year
Golay cell	Room Temperature (RT)	$\approx 0.1\,\text{s}$	2×10^{-10}	1947[18]
Pyroelectric	RT		2×10^{-10}	1950s[19, 20]
Thermopile	RT	$\approx 1 - 10\,\text{ms}$	5×10^{-9}[21]	
Power meters		$\approx 1\,\text{s}$[22]	5×10^{-6}	
Semiconducting bolometers	4.2 K	$\geq 10\,\mu\text{s}$ (Si) $\approx 5\,\text{ms}$ (Ge)	$10^{-13} - 10^{-12}$ (Si) 5×10^{-17} (Ge)[24]	1971[23] 1961[25]
Superconducting bolometers	95 mK	$40\,\text{ps}$[26]	3.3×10^{-17}	
Micro-bolometers	RT	$200\,\text{ns}$[27]	$\approx 1.6 \times 10^{-10}$[28]	1980s

Table 1.1: Thermal detectors review

- the thermal detectors such as Golay cells, pyroelectric detectors, thermopiles, power meters, semiconducting and supraconducting bolometers and micro-bolometers. In this case, the incoming photons produce a measurable temperature change. They are usually slow and their Noise Equivalent Power (NEP) is low. Their characteristics are summarized in table 1.1.

- the photoconductive detectors. Most of them are realized with extrinsic Germanium (Ge), Indium Antimonide (InSb), Gallium Arsenide (GaAs) or rely on block impurity band (BIB). For those devices, the incoming photons interact with electrons in the material which produce a readable current (or change in the resistance). Their response time is much faster and draw benefits of a lower NEP. Those devices are reviewed in table 1.2.

- the heterodyne detectors. By letting two signal with two frequencies f_1 and f_2 close but different interact together, they can produce two signals of frequencies $f_- = |f_1 - f_2|$ and $f_+ = f_1 + f_2$. If f_1 and f_2 are in the GHz range, it is possible for f_+ to fall in the THz domain.Schottky diode Mixer (SDM), Superconductor-Insulator-Superconductor Mixer (SISM) and Hot Electron Mixer (HEM) belong to this category. Those devices are usually preferred for the lower end of the THz frequency range, consequently we did not reviewed them in a table.

Detector	Temperature	Response time	NEP $(W/\sqrt{Hz})$	Year
Ge:Sb	< 4.2 K	$50 - 500\,$ns	10^{-12} down to 4.4×10^{-17}[29]	1959[30]
Ge:Ga	< 4.2 K	$\approx 10\,$ns	8×10^{-13} down to 10^{-17}[31]	1965[32]
Ge:Be	< 4.2 K		down to 10^{-16}	1983[33]
InSb	comparable to Ge:Ga			1960s[34]
GaAs		$23 - 250\,$ns[35]	4×10^{-14}[36]	1960s
BIB	6 K		5.23×10^{-15}[37]	1980

Table 1.2: Photoconductive detectors review

Recent literature reviews on THz photodetectors are available for further information[38, 39, 40].
Finally, efforts have also been made to reduce the dimensionality of the devices. Romeo reported a THz detector with excellent performances[41]. Operating at room temperature, its responsivity has been measured to be $10\,\mathrm{VW}^{-1}$, its NEP approximately $10^{-11}\,\mathrm{W}\sqrt{\mathrm{Hz}}$ and its response time less than 3 μm .

1.3.2 Quantum Well Photodetectors

Quantum Well Infrared Photodetectors

The discovery and development of intersubband transitions in quantum structures boosted optoelectronic research and technologies with the invention of novel devices. Among those devices we can cite the QCL and the Quantum Well Infrared Photodetector (QWIP). An advantage of intersubband transitions is the possibility to tune the device operating wavelength, either for emission or absorption, over a wide range. In fact, by changing the quantum structure size and material we can span from about $1\,\mu$m to $300\,\mu$m. As regards the QWIP, the material of choice is usually GaAs/$Al_xGa_{1-x}As$ and usual quantum structures then lead to an absorption range of about $3-14\,\mu$m. The operation of QWIP devices will be described in section 2.1. The main advantage of QWIP among other photodetectors in the same spectrum region, such as HgCdTe or InSb, relies on the maturity of GaAs and $Al_xGa_{1-x}As$ materials and growth and fabrication processes. In addition, QWIP have shown itself to be very flexible. As an example, it fits perfectly for high-speed and multicolor applications in addition of being very compact of easily integrable. As a consequence they are a perfect candidate for high-speed wireless telecommunications and imagers.
The first studies on intersubband transitions (ISBT) as been first summarized by Ando in the early eighties[42]. Suggestion to use ISBT to realize infrared photodetectors has been published in the late seventies[43]. First demonstration of infrared absorption in quantum well structures has been reported in 1983[44, 45] and the first QWIP experiments in 1985[46] and 1987[47]. In those papers, three QWIP devices have been characterized at room temperature and have peak absorption at 8.15 μm , 10.25μm and 10.8μm . The motivation at this time was to realize fast low-power optical logic, the response speed being very fast, around 30ps. After those forerunning experiments, QWIP has been widely studied and extensive literature reviews exist on the subject[48, 49] as well as books[50, 51].

Different active region designs have been followed to increase the performance of QWIP. We will here summarize them exhaustively. QWIP devices can be sorted in two categories: photoconductive QWIP and photovoltaic QWIP. Photoconductive need a bias to operate whereas photovoltaic can be used under zero bias condition. For single color devices, the active region is a repetition of one pattern that we call a module. We can distinguish the designs according to this module composition.
The first design, which is still the more common, relying on a single well module, each module being separated by a thick barrier It is also the main photoconductive device. The impinging photon can excite an electron from the ground state of the well to a state of

higher energy, either bound to the well (figure 1.7) or in the continuum (figure 1.8). This design is chosen for this work and it will be studied in detail in chapter 2. Asymmetric quantum wells has also been reported to tune the spectrum width[52].

Photoconductive devices benefit from a good responsivity but suffer from an electric-field

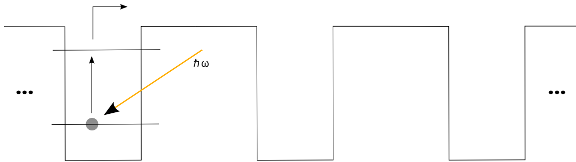

Figure 1.7: Bound-to-bound

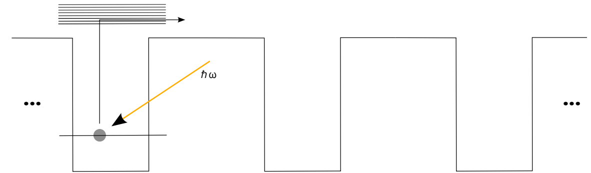

Figure 1.8: Bound-to-continuum

induced high dark current. Photovoltaic QWIPs tackle this issue as they do not need a bias to operate. The next presented designs belong to photovoltaic category. If we decrease the thickness of the barrier, the states are not localized anymore and couple together to extend into the whole active region. Doing so, we create minibands for both the ground and excited states. Different strategies have been studied to collect the electrons: a graded collector has first been used (figure 1.9)[53] before being replaced by a square collector (figure 1.10)[54]. A square collector avoid leakage current from the ground miniband to the collector.

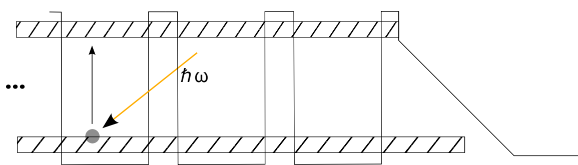

Figure 1.9: Miniband-to-miniband, graded collector

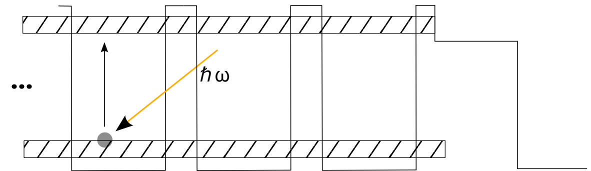

Figure 1.10: Miniband-to-Miniband, square collector

In order to keep a localized ground states and achieve bound-to-miniband transitions, digital graded superlattices have been used. First attempts were using only two materials (figure 1.11) and were suffering from an important interwell tunneling from ground state to ground state. To avoid this drawback, double-barrier structures have been designed with wells of higher energy for the digital graded superlattices (figure 1.12)[55]. Peak absorption wavelength lower than $2\mu m$ has been reached with this last design[56, 57].

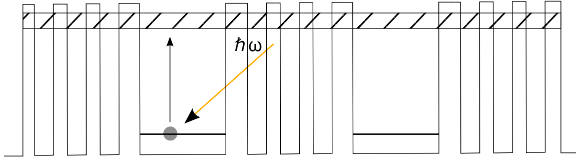

Figure 1.11: Bound-to-miniband

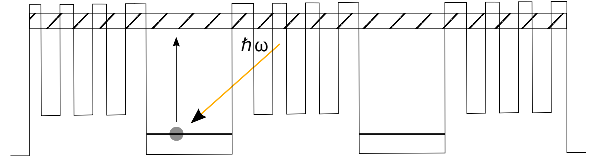

Figure 1.12: Bound-to-miniband, stepped

So as to reach higher detectivity, the four zone QWIP has been proposed by Schneider[58]. This design benefits from phonon-assisted tunneling taking place between the two wells of each module (figure 1.13). This photovoltaic design has shown similar detectivity compared to photoconductive QWIP. This design has been successfully combined with the single well module design to achieve two-color detection in the Mid-Wavelength Infrared (MWIR) and Long-Wavelength Infrared (LWIR)[59].

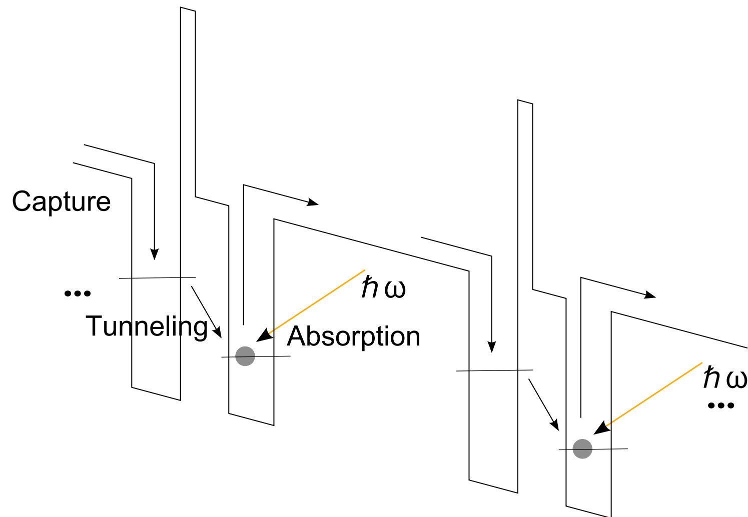

Figure 1.13: Four zone QWIP

Finally, one of the most recent and promising design is the Quantum Cascade Detector (QCD)[60]. In this case, the electron in the excited in not extracted to the next module through the continuum but it cascades to the next module ground state through a series of electronic relaxation (figure 1.14). Very low absorption wavelength of 1.7 μm has been reached with this design[61]. A review of the design, fabrication and characterization of

QCD has been published by Giorgetta[62].

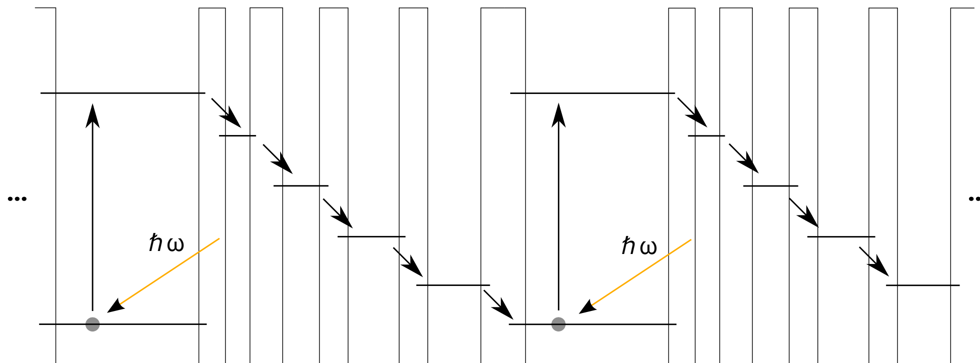

Figure 1.14: Active region of a Quantum Cascade Detector

Terahertz Quantum Well Photodetectors

The first fruitful attempts to sense THz radiation by using GaAs/$\mathrm{Al_xGa_{1-x}As}$ QWP has been reported in 2004 by both Liu[63] and Graf[64]. Liu chose the single well module approach whereas Graf used a QCD device. One motivation to widen the spectral range sensed by QWP to the THz range is the possibility to exploit the background acquired on QWIP, either about their design, fabrication, characterization as well as the maturity of GaAs material. Beside from study of its behavior under high magnetic field[65], QCD design has not been push further after this first attempt. In fact, the energy of the optical transition ($\approx$ 10 meV) being lower than the phonon energy in GaAs ($\approx$ 36 meV), the extraction of the electron through the cascade is solely relying on electron-electron scattering instead of Longitudinal Optical phonon (LO-phonon) scattering. In addition, those devices did not show good performances: the responsivity has been measured to be $8.6\,\mathrm{mAW^{-1}}$ and the detectivity was $5 \times 10^7\,\mathrm{cm}\sqrt{\mathrm{Hz}}\sqrt{\mathrm{W}}$ with a peak absorption wavelength of $\lambda = 84\,\mu m$ at 10 K[64].
More usual bound-to-quasibound THz QWP device has been more studied. State-of-the-art regarding the performance, design of the active region and light coupler as well as an imaging experiment have been reported by Cao in 2011[66] and Guo in 2013[67]. The polarization rules applies exactly the same way as for the n-type QWIP and then we need a light coupling structure for the light to be absorbed by the device. Both usual 45°and surface plasmon induced by metal grating have been experimented. Simulations showed

that metal gratings for the top contact are to increase the absorption efficiency by a factor 30 according to theoretical studies[68, 69]. No p-type THz QWP has been found in the literature. Most of the recent research on THz QWP has been led by H.C. Liu's group.They obtained the best performances for THz QWP: a response time lower than 1 ns and an NEP lower than $10^{-11}\,W/\sqrt{Hz}$ for temperature lower than 20 K over a spectral range of 3.0-7.0 THz. At low temperatures, a responsivity comparable to QWIP $(0.4 - 1.0\,\mathrm{AW}^{-1})$ has been measured.
Other material are also considered for THz QWP. For example, $\mathrm{GaN/Al_xGa_{1-x}N}$ based devices have been studied from 2013 and are expected to cover $\mathrm{GaAs/Al_xGa_{1-x}As}$ Reststrahlen forbidden band from 5 to 12 THz[70, 71]. In fact the phonon energy in GaN is much higher (92 meV) compared to GaAs (36 meV). In addition, such devices are expected to be very fast (the relaxation is around 150 fs) and they could theoretically operates at room temperatures. Nitride-based devices are nevertheless very challenging as regards the growth quality and theoretical simulations, as a consequence no grown THz QWP has been reported yet.

Realistic application relying on THz QWP have yet been reported. THz imaging experiments proofed that it is possible to detect concealed metallic objects such as keys or surgical blades[72, 73]. Besides from imaging, THz free space telecommunications channels using a QCL as a source and a THz QWP as a receiver has been demonstrated[74, 75].

As mentioned previously, the ideal detector would be fast, sensitive, cheap, reproducible and integrable. Apart from its necessity to be cooled down to cryogenic temperature, Terahertz Quantum Well Photodectors appear to be a relevant candidate. In fact, it exhibits a potential very fast response time, a good responsivity, detectivity and NEP. In addition, by being an adaptation of the Quantum Well Infrared Photodetector (QWIP) to longer wavelengths, it is possible to capitalize on the important research that has been done to develop their performances. Especially, the active region design and the light coupling structure has been widely studied in the literature. In addition, we expect that it is possible to integrate THz QWP in Focal Place Arrays (FPAs) like QWIP. Finally, we choose $\mathrm{GaAs/Al_xGa_{1-x}As}$ system as those are well-known materials and the technology is mature.

This thesis focuses on the modeling and design of different structure for THz QWP devices. Discussion on the calculation and the improvement of the performances of this devices will be followed. In particular, the main bottleneck in device performance is the dark current which is too high because of thermal limitations. Designs relying on many-body effects reducing the dark current will be presented.

1.4 Thesis Overview

The focus of this thesis is to describe the physics, simulation and fabrication of THz QWPs and propose new designs that improve their performances.
Chapter 2 theoretically describes the operation of THz QWP. After explaining the operating principles of QWPs, we focus on the design of the active region. We discuss how to choose the optimum well and barrier thickness, fraction of aluminum and doping concentration. The light coupling structure and top metal coverage are studied. We show that, unlike for QWIP device, a metal coverage of 50 % is not necessary optimum. In order to reach more accuracy and better match the experimental results, many-body effects are included in the energy potential calculation. Finally, we highlight the figures of merit that reflect the performances of the device: absorption intensity and spectrum, (termionic and tunneling) dark current, photocurrent, responsivity, detectivity and operating temperature.
In chapter 3, we report our simulation results. First we report the impact of the well and barrier thicknesses and explain how to find their optimum values. The impact of the operating temperature on the performances is then discuss. The calculated potentials and figures of merits for different design are reported. New designs are proposed to increase the performances of THz QWP. By modifying the doping profile we show that we can reduce the dark current by one order of magnitude. We also calculate the absorption spectrum and the peak absorption of those devices.
Information about the fabrication of THz QWPs is given in appendix D.
The main output of this master project is an ensemble of MATLAB routines and functions that are simulating the performances of given active region. In addition to those codes simulating devices, scripts have been written to design the optimum devices for a target absorption frequency.

Chapter 2

Quantum Well Photodetector design

2.1 QWP mechanisms

Quantum Wells Photodetectors (QWPs) are Multiple Quantum Wells (MQWs) structures. One complete device is represented in figure 2.1. The light is impinging through a 45° facet

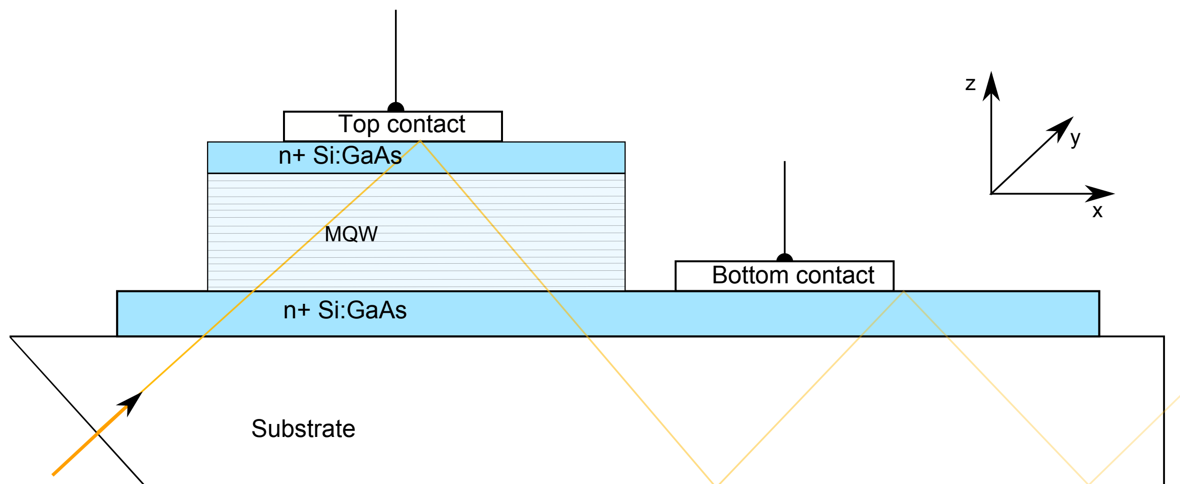

Figure 2.1: Structure of one QWP device.

in the substrate. In fact, a light shining in the z direction can not be absorbed because of the polarization rule. This need of a light coupling structure will be detailed in section

2.3. The radiation is then penetrating in the substrate and the active region, which made of periodic repetitions of barriers and wells of the same thickness sandwiched between two highly doped layers. In the active region, the absorption of light generates photocurrent that can be read at the metal contacts.
The two n+ layers are undergoing different limitations. First, they have to be doped high enough to ensure a good electronic transport from the active region to the electrodes. The high doping (with the help of the extra doping introduced by the contact structure) reduces the depletion region at the metal-semiconductor junction, thus allowing a tunneling-assisted ohmic contact. Second, the doping has to be kept low enough to avoid Thz absorption from the free-carriers.
For THz QWP, materials of choice for the active region are GaAs and $Al_xGa_{1-x}As$ for the wells and barriers respectively. This choice is justified by the fact that the growth technology for GaAs and $Al_xGa_{1-x}As$ is mature, our devices being grown by Molecular Beam Epitaxy. In addition the conduction band-edge discontinuity is easily tunable by changing the Aluminum fraction and matches the energy of THz radiations. In fact, $\Delta E_c = 0.904x$ which yields, for example, a barrier of 9.04 meV (2.2 THz) for 1% of Aluminum , 18.08 meV (4.4 THz) for 2% and 45.2 meV (10.9 THz) for 5%. The active region is then made of a repetition of identical quantum wells and barriers as pictured in figure 2.2. When a photon is absorbed, its energy excites an electron from the ground state of one well to a state of higher energy. The photocurrent generation is in other word relying on an intrasubband transition in the conduction band.

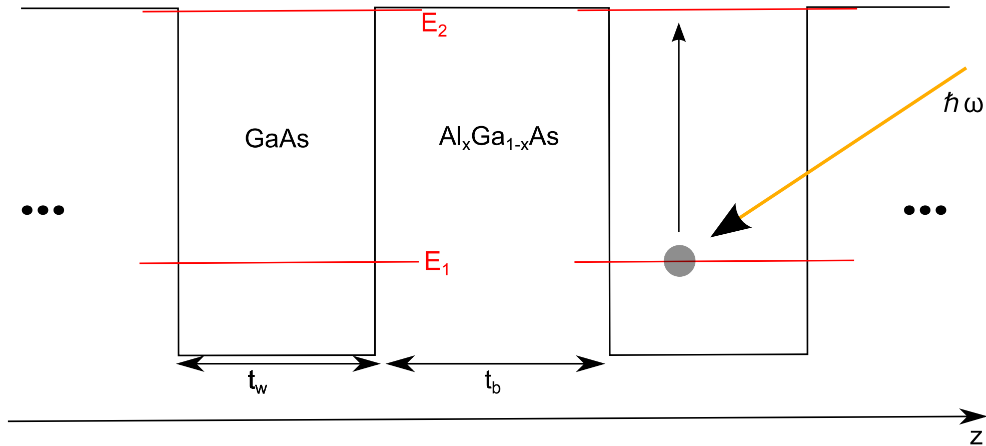

Figure 2.2: Detail of the active region.

Two different kind of active region can be distinguished from the optical transition point-of-view:

- the transition occurs two bound states (figure 2.3.a). Both wavefunctions are then localized which causes a high absorption, a poor escaping efficiency for the electron and a sharp absorption spectrum.
- the transition occurs between the ground state and the continuum (figure 2.3.b). The absorption is then lower, the escaping efficiency higher and the absorption spectrum broader.

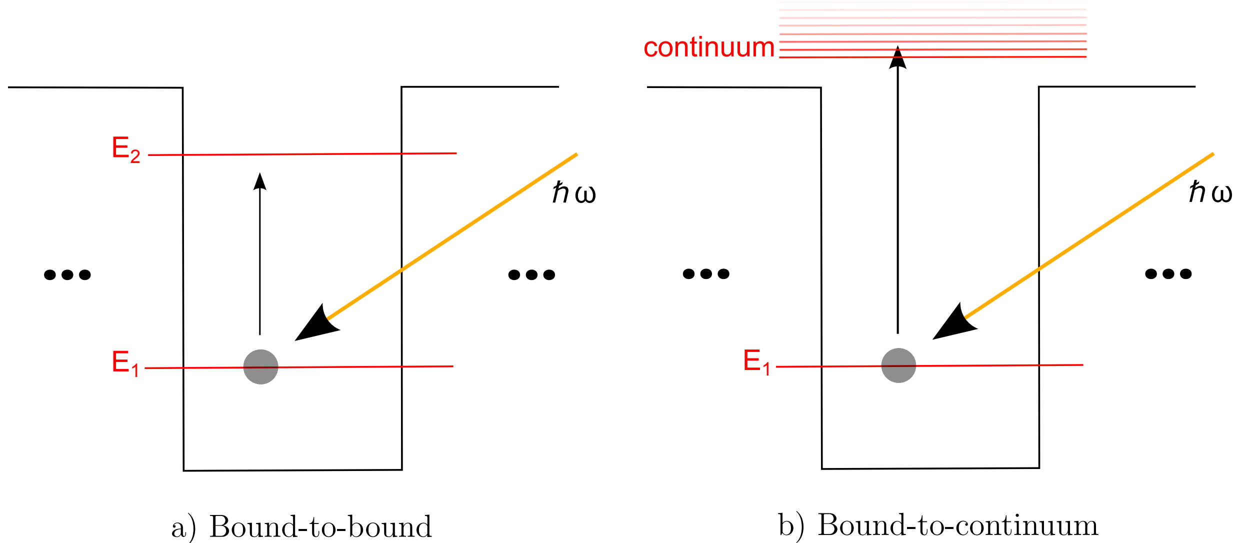

a) Bound-to-bound b) Bound-to-continuum

Figure 2.3: Two possible configuration for the optical transition.

It has been demonstrated with QWIP that to ensure an optimum detection, we have to use an intermediate situation between those two designs with the second energy state at resonance with the top of the barrier.

2.2 Active Region Model

2.2.1 Structure parameters

All the QWPs in this thesis are based on the GaAs/$Al_xGa_{1-x}As$ material system, in which GaAs is the quantum well layer and $Al_xGa_{1-x}As$ is the barrier layer. As n-type QWPs are relying on unipolar intrasubband transitions within the conduction band, we can omit

the valence band and limit the scope of the simulation to the conduction band in a first approximation. The first parameter we have to choose is the fraction of aluminum x. It will define the potential barrier height and thus the achievable energy for the optical transition. The conduction band offset between $\mathrm{Al_xGa_{1-x}As}$ and GaAs is approximated by:

$$\Delta E_c = 0.904x\,(eV) \tag{2.1}$$

The effective mass is taken to be $m_w = 0.067m_0$ in GaAs and $m_b(x) = (0.067 + 0.083x)m_0$ in $\mathrm{Al_xGa_{1-x}As}$. The targeted device total thickness has to be around $3.5\mu m$. Actually, we can not grow thicker devices as it would increases growth defects but have to fit enough wells to ensure strong enough absorption. We usually grow THz QWP with around 10 to 50 wells in the active region. For example if the well thickness is 200 Å and the barrier is 800 Å wide, the highly doped layers are 500 nm each, we can put 26 wells. Devices are under bias while it is operating, this is included in the simulation by tilting the potential. This potential is supposed to be uniform across the active region. We did not include electric field domains that are observed in QWIPs. In fact, when we have electric field domain, we usually observe a plateau-like IV curve[76, 77]. This behavior has not been reported for THz QWPs[78, 79, 80] for absorption frequencies below the Reststrahlen band and as a result we did not take electric field domain into account. In addition, we neglected the electric field non linearity for the wells close to the contacts, induced by electronic recharging effects. The resulting tilted potential is refined by including Many-Body Effects (MBEs). This part will be detailed in subsection 2.2.3. In addition, so as to be able to calculate the states in the continuum and have more accurate calculations, we add two high padding potential barriers on each sides of the simulated wells. Furthermore, despite it is common to only use one well for the simulations in the literature, we took into account multiple wells to run our calculation and then consider the states in the center well. Those states are then repeated periodically to the neighboring wells, shifted in energy accordingly to the electric field. For example, under an electric field F, the $\mathrm{i^{th}}$ energy states of the $\mathrm{k^{th}}$ well is:

$$E_i^k = E_i^0 - keFL_p \tag{2.2}$$

E_i^0 being the $\mathrm{i^{th}}$ energy states of the central well, e the electron charge and $L_p = t_w + t_b$ being the length of one period.

Another important structure parameter is the doping of each module. Traditionally THz QWPs has been uniformly doped at the center of each well, typically over 100 Å. No device with δ-doping or doping not in the center of the wells has been reported. The amount of dopant to be used in THz QWP has been studied and confirmed[78], but to our knowledge

no work has been realized on the impact of the doping profile. The doping concentration is calculated the same way as for QWIP devices. The Fermi level has to be equal to:

$$E_f = \alpha k_B T \tag{2.3}$$

where T is the temperature, k_B is the Boltzmann constant, and α is a constant. We choose $\alpha = 1$ if we want to maximize the BLIP temperature and $\alpha = 2$ if we are looking to optimize the highest dark-current-limited detectivity[81]. The 2-dimensional doping density is then deduced by:

$$N_{2D} = \frac{m_e E_f}{\pi \hbar^2} = \frac{\alpha m_e k_B T}{\pi \hbar^2} \tag{2.4}$$

In this equation, m_e is the effective mass of the electron, E_f is the Fermi level and $\hbar$ is the reduced Planck constant. Further explanations on this choice will be given in section 2.5.4

2.2.2 Energy state and wavefunction calculation

The energy levels and wavefunctions in the structures has been obtained by using the transfer matrix (TM) method[82]. To ensure a more realistic calculation of the energy states and reduce the boundary effects, we run the simulation not only for one sole quantum well, but for multiple modules with a higher potential on the sides as a virtual boundary. We then consider the well in the center as it is the less affected by the boundaries. These procedures has been used for QWIP simulation in the literature[83]. We represent an example in figure 2.4. As we can see, the higher states are more affected by the side-effects as their wavefunctions are less localized.

In order to have a more accurate simulation, we have included the effective mass nonparabolicity[84, 85]. It is then energy and position dependant within the wells and barriers. The nonparabolicity coefficient for GaAs is assumed to be $4.9 \times 10^{-19}\ m^2$. This value has been successfully used for THz QCLs.

An issue with this procedure is the subdivision of the energy range. In fact, if we use a linear subdivision of the energy range, the required computational time becomes too long for low electric fields. Indeed the barrier being very thick, the ground state level do not coupled together and as a consequence they do not split significantly. For an example, for very low electric field, the spacing between the ground states of neighboring wells can be lower than 10^{-3} meV while we have to look for energy states over more that 20 meV. The use of a linear subdivision would induce to calculate the transfer matrix for at least 10^6 points. To avoid this non realistic computational time and because we usually run our simulation over a wide range of applied electric field, we start with the higher electric field

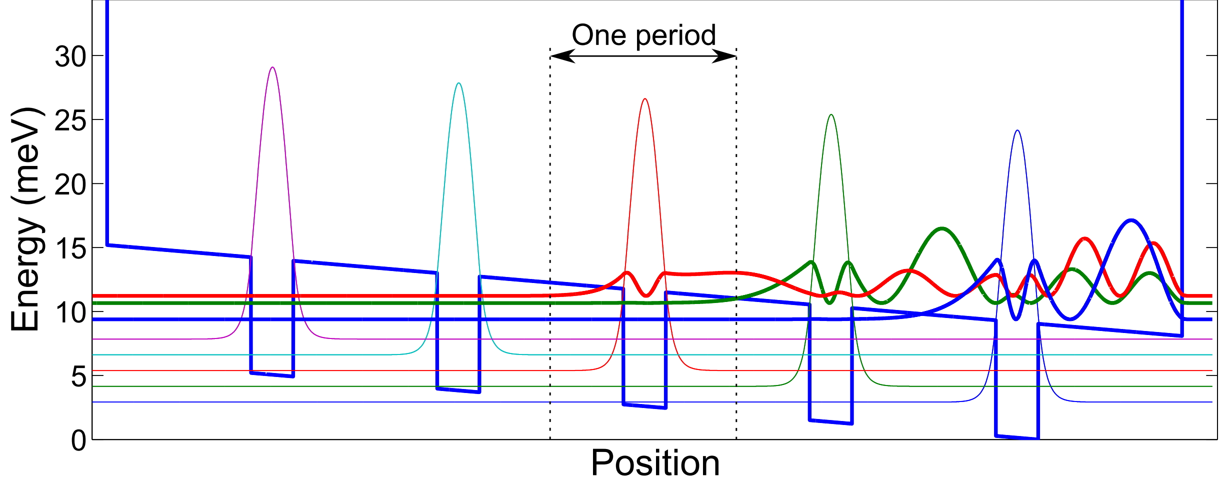

Figure 2.4: Example of potential and wavefunctions calculated with the TM method. The wavefunctions are offset for more clarity.

for which the energy states are spaced enough to use a coarse linear subdivision. We then benefit from those energy states to narrow the energy range to study for the next electric field. With this method, we reduced the number of energy states to use below 10^4. As a consequence the computational time is reduced by two orders of magnitude.

2.2.3 Many-body effect

Exchange-correlation potential for electron gas has been developed in the frame of the local density theory[86]. Many-body effects on intersubband transitions in multiple quantum wells structure has been theorized by Bloss[87]. The first observation of many-body effects on the peak absorption frequency of THz QWP has been reported by Graf[88]. The energy states and wavefunctions are calculated from the one-dimensional Schrödinger equation:

$$\frac{-\hbar^2}{2m_e}\nabla^2\Psi(r) + V(r)\Psi(r) = E\Psi(r) \tag{2.5}$$

with a total potential $V(r) = V_{cr}(r) + V_H(r) + V_{xc}(r) + eFz$ and an electron effective mass m_e.
V_{cr} represents the ideal square potential of the crystal, V_H is the Hartree potential resulting from the electron gas and the ionized donors, V_{xc} is the exchange-correlation potential, and

the last term eFz represents the voltage induced potential drop.
The Hartree and the exchange-correlation potentials are calculated within the local density approximation[87, 88]:

$$V_H(z) = \frac{e^2}{\epsilon_s \epsilon_0} \int_{-\infty}^{z} (z - z')(N_D(z') - n(z'))\mathrm{d}z' \tag{2.6}$$

where ϵ_s (ϵ_0) is the static (vacuum) permittivity, $N_D(z)$ is the doping profile and $n(z)$ represents the electronic distribution:

$$n(z) = \frac{m_e k_B T}{\pi \hbar^2} \sum_i \ln\left(1 + e^{\frac{E_f - E_i}{k_B T}}\right) |\Psi_i(z)|^2 \tag{2.7}$$

T is the temperature, E_f the Fermi level, E_i the ith bound state, $\Psi_i(z)$ is the ith wavefunction, m_e is the effective mass of the electron, k_B is Boltzmann constant, $\hbar$ is Planck constant. The Hartree potential is then determined by both doping profile and carriers distribution. As a consequence the dopant position is critical. The doping concentration is not a degree of freedom as we have seen in section 2.2.1. Furthermore, it is also not possible to exploit the electron distribution as they sit at the ground state of each well which wavefunction is not alterable easily. The effective mass is imposed by the choice of the material.

$$V_{xc} = \frac{-2}{\pi \alpha r_s} \left(1 + \frac{B r_s}{A} \ln(1 + \frac{A}{r_s})\right) \quad \text{(Ryd)} \tag{2.8}$$

where $\alpha = (9\pi/4)^{-1/3}$, $r_s = \frac{m_e}{m_0 \epsilon_s}(4\pi n(z)/3)^{-1/3}$, $A = 11.4$, $B = 0.6213$. It is important to emphasize that the exchange-correlation potential is only depending on the carrier distribution $n(z)$ through r_s and on the effective mass. We do not have a control on those two parameters and on V_{xc} as a result.
Accordingly, the dopant position is the only parameter we can play with to change the potential corrections induced by the MBEs. This idea will be exploited in section 3.2 to propose new designs.

In addition to these two effects on the band structure, we can refine our model by including two dynamic effects: depolarization and exciton shifts. The corrected transition energy is then given by:

$$E'_{21} = E_{21}\sqrt{1 + \alpha - \beta} \tag{2.9}$$

where E'_{21} and E_{21} are the optical transition energies respectively with and without the dynamic corrections and α represents the depolarization shift:

$$\alpha = \frac{2e^2 N_{2D}}{\epsilon_s \epsilon_0 E_{12}} \int_{-\infty}^{+\infty} \left(\int_{-\infty}^{z} \Psi_2(z')\Psi_1(z')dz' \right)^2 dz \quad (2.10)$$

N_{2D} is the two-dimensional sheet carrier density. β is the exciton shift:

$$\beta = -\frac{2N_{2D}}{E_{12}} \int_{-\infty}^{+\infty} dz \Psi_2(z)^2 \Psi_1(z)^2 \frac{\delta V_{xc}(n(z))}{\delta(n(z))} \quad (2.11)$$

2.3 Optical Coupling

2.3.1 Polarization Rule

The transition rate $W_{i \to f}$ between an initial state $|i\rangle$ (of energy E_i) and a final state $|f\rangle$ (of energy E_f) is quantified by Fermi's golden rule:

$$W_{i \to f} = \frac{2\pi}{\hbar} |\langle f|H'|i\rangle|^2 \delta(E_f - E_i - \hbar\omega) + \frac{2\pi}{\hbar} |H'_{fi}|^2 \delta(E_f - E_i + \hbar\omega) \quad (2.12)$$

The first term stands for the absorption of a photon of energy $\hbar\omega$ by the material and the second one for the emission of a photon of energy $\hbar\omega$. More details about this derivation is found in textbooks[89]. For an optical transition, the interaction Hamiltonian is:

$$H'(\mathbf{r}) = -\frac{eA_0 e^{i\mathbf{k}_{op}.\mathbf{r}}}{2m_0} \hat{e}.\mathbf{p} e^{-i\omega t} - \frac{eA_0 e^{-i\mathbf{k}_{op}.\mathbf{r}}}{2m_0} \hat{e}.\mathbf{p} e^{i\omega t} \quad (2.13)$$

$\hat{e}$ is a unit vector in the direction of the electric field, A_0 is the amplitude of the potential vector, $\mathbf{k}_{op}$ is the wavevector of the radiation and $\mathbf{p}$ is the momentum operator. The transition rate for the absorption becomes:

$$W^{abs}_{i \to f} = \frac{2\pi}{\hbar} |H'_{fi}|^2 \delta(E_f - E_i - \hbar\omega) \quad (2.14)$$

The matrix element can be rewritten as a function of the electric field representing the light:

$$H'_{fi} = -e\langle f|e\mathbf{r}.\mathbf{E}|i\rangle \quad (2.15)$$

From this last equation, we can see that the matrix element, and then the transition rate, vanishes when the light is shining perpendicularly to the top facet, in the growth direction. This natural configuration being not possible, we have to use a light coupling structure. So far, three main light coupling structure have been widely used for QWIPs and under investigation for THz QWPs:

- we tilt the device at the Brewster angle
- one facet is etched at 45° and the light is shone orthogonally to this facet
- a metal grating is deposited below the top metal contact and the light is shone along the growth direction.

A light coupling structure is not needed for p-type QWP and Quantum Dots Photodetectors (QDPs)[90]. In fact, for those devices the polarization rule is different and is not forbidding absorption of light in the growth direction. In p-type QWP, a large absorption is possible thank to valence-band mixing effects between the light and heavy-hole bands[91].

2.3.2 Coupling structures

Aware of this polarization rule, different schemes to couple the light into the device have been studied.
The easiest configuration is to tilt the device at the Brewster angle. The refractive index of GaAs is $n_r = 3.3$ which yield a Brewster angle of approximatively 73°. This is a useful way to do prototyping and experiments in transmission mode. Nevertheless in this configuration the light is coupled with the active region with a relatively small angle of 17° that gives a low absorption.
The 45° facet structure has been the first to be used due to its simplicity. Indeed we glue the device on top of a 45° mount by the mesa side, substrate being exposed, and we lap it horizontally. Additional information are given in section D. In addition, in this configuration, the light experiences total internal reflection at the top contact and at the bottom of the substrate and the absorption is taking place each time the light passes through the active region. Absorption can be typically multiplied by 4 to 6 times this way. Nevertheless with this structure, it is not possible to integrate devices in a FPA. Those advantages and drawbacks make it mainly used for prototyping.

If we want to realize a QWP FPA, the light has to impinge perpendicularly to the devices. As a consequence, it is not possible to use a 45° facet to couple the light into

the device. The strategy adopted for QWIP devices is to realize a metal grating on top of the mesa. They have been widely studied in the infrared range[92, 93, 94] and rely on the diffraction of the light by the grating. They have also been shown to increase the absorption [95]. As a general rule, the grating period L_g should be related with the wavelength in vacuum λ and refractive index of GaAs n_r by $L_g = \lambda/n_r$ and their depth d should be the fourth of the period $d = L_g/4$. Doing so the zero-order diffraction is suppressed and the first-order diffracted beam can be absorbed. Even tough this procedure has been successful in the infrared range, it is not usable as is in the terahertz range. In fact, if we assume we want to sense a wavelength of $\lambda = 330\mu m$, we should etch a grating of period $L_g = 100\mu m$ but this is the typical pixel size. To cope with this problem we capitalize on another physical effect: the surface plasmon. Surface plasmons correspond to carrier oscillations at the interface between a metal and a dielectric that can be excited by light thus creating a polariton. We refer to the literature for more theoretical information[96, 97]. Such subwavelength gratings have been very recently studied for THz QWP and are expected to yield tens of time more efficient coupling structures compared to the 45° facet[68, 69].

Recently the corrugated coupling structure has been proposed and studied by Choi[98]. They consist in V-shaped mesas realized by anisotropic chemical etching. The light impinges from the bottom of the devices and reflects twice onto this so-etched 45° facets.

2.4 Top Metal Coverage

If we use the 45° configuration, the light is bouncing back inside the QWP at the metal top contact such as shown in figure 2.5. The reflected wave is then interfering with the incident wave which result in a standing wave inside the cavity[99]. As a result, the density of light in the active region is changing along the growth axis and we can estimate its variation with a simple electromagnetic model. We assume that the light is impinging with a wave vector $\mathbf{k} = k_x sin(\theta)\hat{x} + k_z cos(\theta)\hat{z}$ and $|\mathbf{k}| = 2\pi/\lambda$ where λ is the wavelength of the radiation. The top contact is considered as a perfect metal. If the top metal contact was covering 100% of the surface, the electric field would be:

$$\mathbf{F}^m = \begin{pmatrix} F_x \\ F_y \\ F_z \end{pmatrix} = 2F \exp\left(ik_x x - i\omega t\right) \begin{pmatrix} i\cos\theta\sin(k_z z) \\ 0 \\ \sin\theta\cos(k_z z) \end{pmatrix} \tag{2.16}$$

On the other side, we can virtually derive what would be the electric field if no metal was present on top of the active region. The critical angle between GaAs ($n_{GaAs} = 3.3$) and

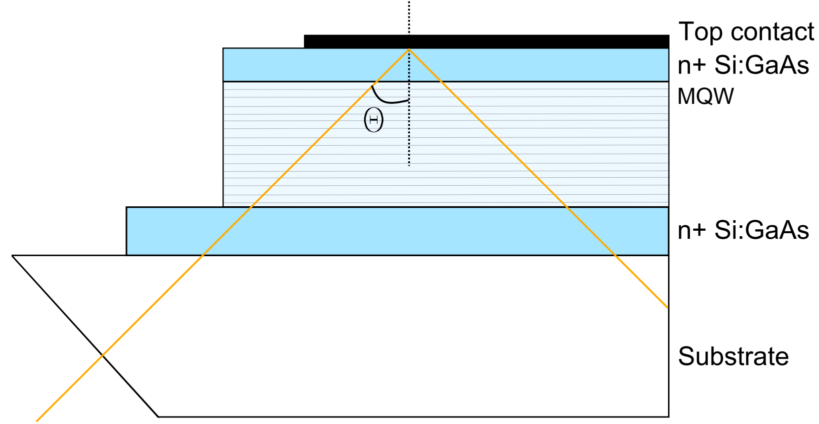

Figure 2.5: 45° facet configuration resulting in a standing wave.

the air ($n_{air} \approx 1$) is around:

$$\theta_c = \arcsin\left(\frac{n_{air}}{n_{GaAs}}\right) \approx \arcsin\left(\frac{1}{n_{GaAs}}\right) \approx 16.1° \tag{2.17}$$

As the angle of incidence is much higher than the critical angle, the impinging light experiences dielectric reflection that introduces an additional $\pi/2$ phase shift. The total electric field is then:

$$\mathbf{F}^d = 2F \exp\left(ik_x x - i\omega t\right) \begin{pmatrix} \cos\theta\cos(k_z z) \\ 0 \\ i\sin\theta\sin(k_z z) \end{pmatrix} \tag{2.18}$$

If we have an intermediate situation where only x % of the device is covered by metal, the rest being surrounded by air, we write the resulting electric field as:

$$\mathbf{F}^t = \mathbf{F}^m\sqrt{x} + \mathbf{F}^d\sqrt{1-x} \tag{2.19}$$

According to the polarization rule, only the electric field in the growth direction, $\hat{z}$, can be absorbed. By using the previous equations, we can derive the modulus of the z component of the resulting electric field:

$$|F_z^t|^2 = |2F\sin\theta|^2\left(x + \sin^2\left(k_z z\right)(1-2x)\right) \tag{2.20}$$

Calculations to reach this result and additional details are shown in appendix C.
We plotted the power density $|F_z^t|^2$ for a QWIP and a THz QWP on figure 2.6. The

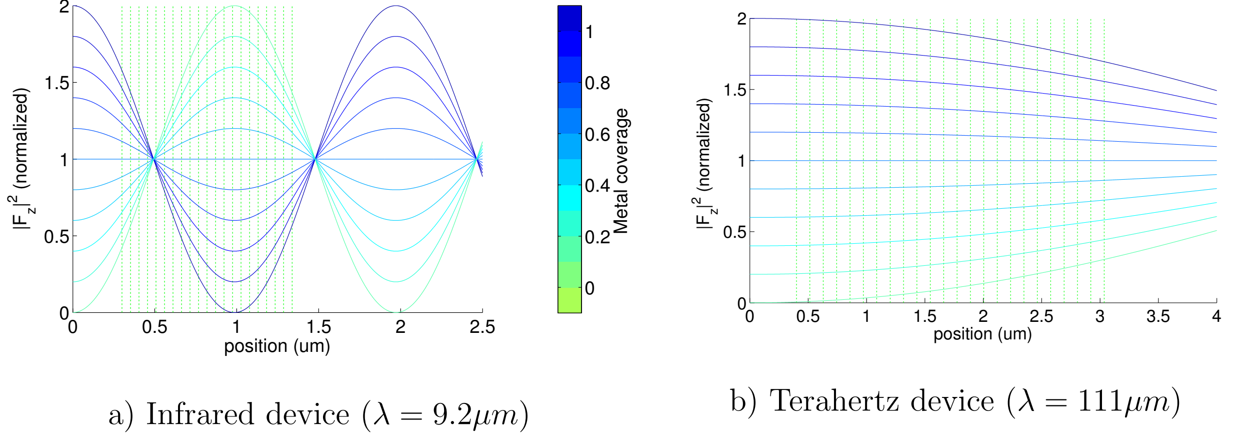

a) Infrared device ($\lambda = 9.2\mu m$)

b) Terahertz device ($\lambda = 111\mu m$)

Figure 2.6: Power density for an infrared and a terahertz QWP, the modules are represented in dashed green.

structure of this QWIP has been used to highlight the effect of interferences[99]. Our result differ from the paper as we considered the material index of GaAs to be $n = 3.3$ instead of 3.6. For the second device (THz QWP), we have 23 modules with a well width of $t_w = 19.5\,\mathrm{nm}$ and a barrier thickness of $t_b = 95.1\,\mathrm{nm}$ (20 modules with $t_w = 4.4\,\mathrm{nm}$ and $t_b = 47.5\,\mathrm{nm}$ for the QWIP). The frequency of the incoming light in the vacuum is set to $f_0 = 2.7\,\mathrm{THz}$ ($\lambda_0 \approx 111\,\mu m$). In addition, the GaAs spacer between the top contact and the first barrier is set to 400 nm, compared to 300 nm for the QWIP. As the wavelength is much shorter in the case of the QWIP, the power density is varying much faster compared to the THz QWP. This effect is not desirable as:

- detection non linearities are introduced. In our QWIP example (figure 2.6 a)), the power density is changing from 80% to 0% of its maximum value if we set $x = 100\%$. The number of electrons excited by photo-absorption would drastically different for each well.

- the absorption becomes spatial dependant and the thickness of great importance. In our example for QWIP, the potential wells are located at a minimum of the power density if we assume that the metal covers the whole surface ($x = 100\%$). As a consequence, the resulting absorption would be very low.

The usual way to avoid those unwanted effects in QWIP is to cover 50 % of the device with the metal top contact. In fact, in this special value, the power density becomes uniform:

$$\left|F_z^t\right|^2 = \frac{\left|2F\sin\theta\right|^2}{2} \tag{2.21}$$

When the light impinges with an angle $\theta = 45^\circ$ this yield $\left|F_z^t\right|^2 = |F|^2$.
Accustomed to this practice, the impact of the metal coverage has never been studied for THz QWPs. Nevertheless, the wavelength being much larger in the THz domain (by an order of magnitude), the first extremum of the power density inside the device is far from the quantum wells region. It varies much slower than with a QWIP device. Figure 2.6 b) shows that even with a full metal coverage ($x = 100\%$), the power varies only from almost 100% to 85% of its maximum value. For a metal coverage of 60%, the variation ranges from 60% to 57%. Compared to QWIP, we can consequently increase the power density inside the THz QWP up to a factor 2 by increasing the metal proportion with respect to the area of the mesa without increasing too much the non linearities.

2.5 Figures of merit

2.5.1 Absorption

The absorption of THz QWP devices is very low, typically a fraction of percent for each well. As a results it is essential to optimize this parameter. Not only the magnitude of the absorption is critical, but so is it spectrum. The absorption spectrum of QWPs is usually very sharp and they are designed to operate at a specific frequency. The absorption of one well is expressed by:

$$\eta(\omega) = \frac{e^2 \mathrm{h} N_{2D}}{4\pi\epsilon_0 n_r m_e \mathrm{c}} \frac{\sin^2\theta}{\cos\theta} \sum_{n=2} f_{1,n} \frac{\Delta E}{(E_{1,n} - \hbar\omega)^2 + (\Delta E)^2} \tag{2.22}$$

In this equation, h, m_e, c and n_r are respectively Planck constant, the electron effective mass, the speed of light and the refractive index of GaAs. At optical frequencies $n_r = 3.3$ for GaAs. N_{2D} is the sheet doping density calculated with equation 2.4. ΔE is a parameter that reflects the broadening of the energy states (we assume the usual value of 10 meV), θ is the incident angle of the light. We assume to be using a 45° facet ($\theta = 45^\circ$) configuration. $E_{1,n}$ is the energy spacing between the ground and the n$^{\mathrm{th}}$ state and $f_{1,n}$ is the oscillator

strength between the ground and the n$^{\text{th}}$ state, defined in a first approximation by:

$$f_{1,n} = \frac{2m_e E_{1,n}}{\hbar^2} |\langle \Psi_n | \hat{z} | \Psi_1 \rangle|^2 \tag{2.23}$$

Ψ_n is the wavefunction associated with the ith state and $\hat{z}$ is the position operator. This equation holds when the effective mass of the electrons is constant across the barrier. A more detailed calculation has been used taking into account the effective mass nonparabolicity[100] as mentioned in section 2.2.2. It yields slightly lower oscillator strength compared to equation 2.23.
The total absorption of a structure with N wells is $\eta = \sum_i \eta^i = N\eta^i$ if we assume all the well to be identical.
From equation 2.22 we can identify the main parameters that affect the absorption.

- The parameter showing the most immediate dependence is the doping N_{2D}. The dependence of the absorption on the doping is linear. Even though is seems favorable to increase N_{2D}, we will explain in section 2.5.4 that an optimum value should not be overcome. In fact, it would increase the dark current and thus reduce the detectivity or the maximum operation temperature.

- The next parameter having an impact on the absorption is the oscillator strength between the ground state and the higher energy states $f_{1,n\geq 2}$. From equation 2.23, it linearly depends on the optical transition energy, making it harder to reach lower frequencies, and the spatial overlap of the wavefunctions associated with the optical transition. If we target a specific wavelength, we can only exploit the wavefunctions shape, which means vary the potential shape. This is the approach that we followed in section 3.2: we took advantages of the MBEs to tailor the potential and tune the parameters.

- Finally, the linewidth of the spectrum is determine by the parameter ΔE that represents the energy states broadening. This absorption linewidth has been allocated to the roughness and phonon scattering after both theoretical and experimental investigations by Unuma[101, 102]. Throughout this project we assume that $\Delta E = 10\,\text{meV}$, we also sometime choose non-realistic very small values (below $1\,\text{meV}$) to identify clearly the role of each optical transition as regards the absorption spectrum.

2.5.2 Dark Current

Different models has been developed to estimated the dark current. Monte-Carlo, rate equations, 3D carrier drift, emission-capture models, self-consistent drift-diffusion and self-consistent emission-capture has been used with some success. We decided to focus on the emission-capture and 3D carrier-drift model as they are the only model that has shown good results in the THz range. Nevertheless, even within the framework of this model, no definitive agreement has been accepted as regards some parameters.
The total dark current can be expressed has:

$$j_d = \int_{E_1}^{\infty} \rho(E) f_{FD}(E) D(E) dE \tag{2.24}$$

where E_1 is the ground state energy, ρ is the density of states and $f_{FD}(E)$ is the Fermi-Dirac distribution. $D(E)$ is the transmission probability. In our case, we just have one bound state in the well, then we can simplify this expression into:

$$j_d = \frac{m_e}{\pi \hbar^2 L} \int_{E_1}^{\infty} f_{FD}(E) D(E) dE \tag{2.25}$$

In fact, the 2D density of states is given by:

$$\rho = \rho_{2D} = \frac{m_e}{\pi \hbar^2 L} \sum_n H(E - E_n) = \frac{m_e}{\pi \hbar^2 L} \tag{2.26}$$

H is the Heaviside function, m_e the effective mass and $\hbar$ the Planck constant. No general consensus has been reached as regards the value of L. According to Levine[103], Liu and Schneider[81], $L = L_p = t_w + t_b$ is the period of the MQW region. Nathan[104] considers it is only the well width t_w as it is not possible to decrease the dark current indefinitely by increasing the barrier thickness.
Dark current can be decomposed in three different components: interwell tunneling j_{tu}, tunneling assisted thermionic emission j_{tat} and direct thermionic emission j_{th}:

$$j_d = j_{tu} + j_{tat} + j_{th} \tag{2.27}$$

The interwell tunneling is taking place between the ground states of adjacent wells, tunneling assisted thermionic emission is when an electron from the ground state reach the continuum after tunneling through the barrier and direct thermionic emission is when an electron gain enough thermal energy to jump direct from the ground state to the contin-

uum. Those dark current mechanisms are pictured in figure 2.7. Those leakage path for the current are pictured in figure 2.7.

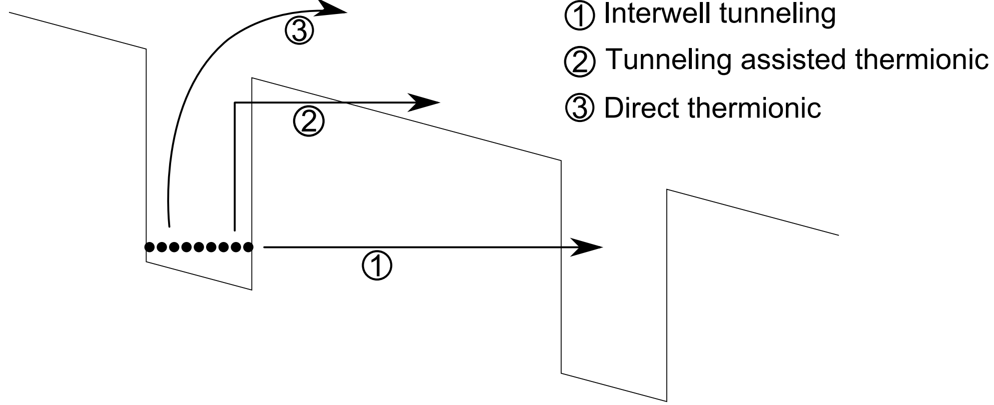

Figure 2.7: Dark current mechanisms in a QWP.

According to Nathan[104], the tunneling dark current can be expressed as:

$$j_{tun} = \frac{evm_e D(E_1)}{\pi\hbar^2 t_w} k_b T \ln\left[\frac{1+\exp\left(E_f/k_bT\right)}{1+\exp\left((E_f-eV)\right)/k_bT)}\right] \tag{2.28}$$

This equation takes into account both interwell tunneling and tunneling-assisted thermionic emission.

The direct thermionic dark current is caused by the electrons distributing above the barrier. For those electrons, $D(E) = 1$ as they belong to the continuum. The direct thermionic dark current then write:

$$j_{th} = \frac{evm_w}{\pi\hbar^2 L}\int_{V_b}^{+\infty} f_{FD}(E)\mathrm{dE} \tag{2.29}$$

$$= \frac{evk_bT\ln\left(1+\exp\left(\frac{E_f-V_b}{k_bT}\right)\right)}{\pi\hbar^2 L} \tag{2.30}$$

$D(E)$ is the transmission probability and has been calculated in the framework of the WKB approximation. In the case of an ideal square well potential, we obtain the formula presented in table 2.1 for an electric field F.

The calculation of $D(E)$ in the framework of the WKB approximation is detailed in appendix B for arbitrary potential shapes. It is exponentially dependant on the barrier

Energy E	transmission probability D(E)
$E < V_b - eFL_p$	$\exp\left\{\left(-\frac{4}{3eF}\right)\frac{\sqrt{2m_b}}{\hbar}[(V_b - E)^{3/2} - (V_b - E - eFt_b)^{3/2}]\right\}$
$V_b - eFL_p \leq E < V_b$	$\exp\left[\left(-\frac{4}{3eF}\right)\frac{\sqrt{2m_b}}{\hbar}(V_b - E)^{3/2}\right]$
$E \geq V_b$	1

Table 2.1: WKB approximation of D(E)

thickness t_b, and as a result so is the tunneling dark current. This will be illustrated in subsection 3.1.2. V is the voltage drop across the barrier and v is the drift velocity related to the electric field F by:

$$v(F,T) = \frac{\mu(T)F}{\sqrt{1 + (\mu(T)F/v_{sat})^2}} \tag{2.31}$$

For the mobility $\mu(T)$ we used the values reported by Tan[80] as well as his derivation of the total dark current:

$$j_{da} = \frac{em_b}{\pi\hbar}\sqrt{\frac{m_b k_b T}{2\pi}}\int_{E_1}^{+\infty}\frac{D(E)\mathrm{dE}}{1 + \exp\left((E - E_f)/k_b T\right)} \tag{2.32}$$

One goal to achieve when designing the QWP is to keep the thermionic dark current higher than the tunneling component in order to avoid bottom-out effect. This challenge will be develop in section 3.1.2.

2.5.3 Photocurrent

The total photocurrent is given by:

$$I_{photo} = e\eta\Phi g_{photo} = e\eta\Phi\frac{p_e}{Np_c} \tag{2.33}$$

where $g_{photo} = \dfrac{p_e}{Np_c}$ is the photoconductive gain, p_e and p_c are respectively the escape and capture probabilities:

$$p_e = \frac{\tau_{relax}}{\tau_{relax} + \tau_{esc}} \tag{2.34}$$

$$p_c = \frac{\tau_{trans}}{\tau_{trans} + \tau_c} \tag{2.35}$$

$$\tag{2.36}$$

Each well is creating a photocurrent:

$$i^i_{photo} = e\Phi\eta^i p^i_e \tag{2.37}$$

The total photocurrent is deduced to be:

$$I_{photo} = e\phi\eta g_{photo} \tag{2.38}$$

$g_{photo} = p_e/Np_c$ is the photoconductive gain and ϕ the number of incident photon per unit time. From this equation, we can see that we can maximize the photocurrent by increasing the absorption and the escape probability. This explains why we have to use bound-to-quasibound devices. With a bound-to-bound transition the absorption is high, due to the strong oscillator strength, but the escape probability is low as the electron have to tunnel through the barrier to reach the continuum. The opposite takes place with a bound-to-continuum QWP: the escape probability is maximum but the absorption is low as the excited state is not localized. A new structure relying on many-body effects is described as device S03 in section 3.2 to finely tune this trade off between optical absorption and electronic escape from the well to the continuum.
As an example we estimate the evolution of the photocurrent with the capture probability p_c for a THz QWP designed to absorbed a light of energy 10 meV. The one well absorption is ranging from 0.01% to 0.1% (typical values for a THz QWP) with a step of 0.01%. The pixel size is taken to be 100 $\mu m \times 100$ $\mu m = 10^{-4}$ cm^2. To calculate the incident number of photons per unit time we consider a laser with an output power of 1 mW, achievable with actual THz QCLs. The resulting photocurrent is shown in figure 2.8. We can note the linear dependence of the photocurrent on the absorption. The expected currents range between approximately 100 μA to 1 mA. It agrees with the responsivity reported in the literature[79].

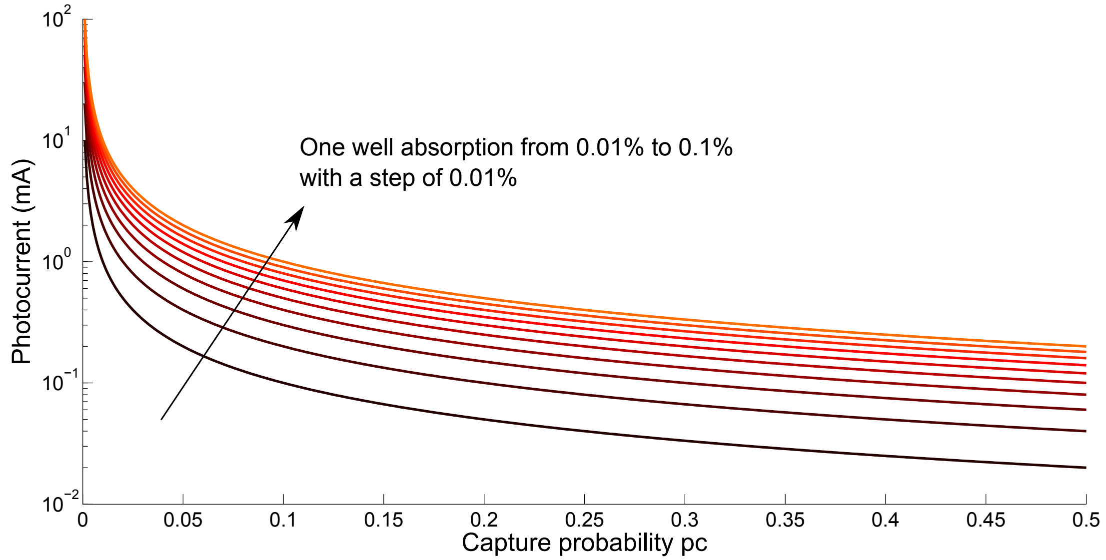

Figure 2.8: Evolution of the photocurrent with the capture probability for different absorptions.

2.5.4 Macroscopic figures of merit: Responsivity and Detectivity

Two main factor of merits are usually calculated to quantify the QWP performances: the responsivity and detectivity. They translate the microscopic and mesoscopic parameters, such as the energy states position, the absorption and the dark current, at the macroscopic scale. A better understanding and a formal derivation of those quantities allow us to identify the parameters that we have to optimize to improve THz QWP performances. They have been widely studied and derived in the past, more information can be found in the literature[81].

Responsivity

The responsivity measures the amount of photocurrent I_{photo} that can be generated for a given input enlightenment energy $h\nu\phi$, where h is Planck constant, ν the photon frequency and ϕ the number of incident photon per unit time and $\eta(\lambda)$ is the absorption spectrum.

It is calculated with:

$$R(\lambda) = \frac{I_{photo}}{h\nu\phi} \tag{2.39}$$

$$= \frac{e}{h\nu}\eta(\lambda)g_{photo} \tag{2.40}$$

In the case of a bound-to-quasibound (or bound-to-continuum) device, we have $p_e \approx 1$ and then by measuring the responsivity we can experimentally deduce the capture time p_c from equation 2.40:

$$p_c = \frac{e}{h\nu}\eta\frac{1}{NR} \tag{2.41}$$

where N is the number of wells in the active region.

Detectivity

Even tough the responsivity gives valuable information on the detector performances, it fails to take into consideration the amount of dark current. The detectivity links the responsivity R and relevant dark current processes. For a detector of surface A, it is defined as:

$$D^* = R\sqrt{\frac{A}{S}} \tag{2.42}$$

$S = 4egI_{dark}$ is the dark current power spectral density (we assume that the gain is close to the photoconductive gain: $g \approx g_{photo}$).
Depending on the operation temperature, the main source of dark current is different.

- At high temperature the dark current primarily rises from the detector active region. The electrons are excited from the ground states of the wells to the continuum not by absorbing a photon energy but by gaining thermal energy. In this case, we can write the detectivity depending either on the 2D or 3D concentration of electrons above the barrier (respectively N_{2D}^{ab} and N_{3D}^{ab}):

$$D_{det}^* = \frac{\lambda}{2hc}\frac{\eta}{\sqrt{N}}\sqrt{\frac{\tau_c}{N_{3D}^{ab}L_p}} \tag{2.43}$$

$$= \frac{\lambda}{2hc}\frac{\eta}{\sqrt{N}}\sqrt{\frac{\tau_{scatt}}{N_{2D}^{ab}}} \tag{2.44}$$

  In those equation, τ_c is the electron capture time in the well and τ_{scatt} is the electron scattering time to the continuum. The 3D concentration of carriers above the barrier

is usually written as:

$$N_{3D}^{ab} = 2\left(\frac{m_w k_B T}{2\pi\hbar^2}\right)^{3/2} \exp\left(-\frac{hc}{\lambda_{cut} k_B T} + \frac{E_f}{k_B T}\right) \tag{2.45}$$

Where $\lambda_{cut} \triangleq 1.1\lambda_{peak}$ is the cut-off wavelength and E_f the Fermi level.
It has been shown that $D^*_{det} \propto E_f \exp(-E_f/2k_BT)$, as a consequence D^*_{det} is maximized when $E_f = 2k_BT$ (in order to have $\partial D^*_{det}/\partial E_f = 0$). It imposes a value for the doping as it is related to the Fermi level by:

$$N_{2D} = \frac{m_e E_f}{\pi\hbar^2} \tag{2.46}$$

- At low temperature, typically below 15K, the detector dark current becomes smaller than the noise induced by the fluctuation of the photocurrent caused by background photons. This is the background limited performance, or BLIP, regime. The sensitivity of the detector is optimal under BLIP conditions. The critical temperature for which the dark current equalizes the background photocurrent is called the BLIP temperature, written as T_{BLIP}. If we want to maximize T_{BLIP}, we have to verify the condition $E_f = k_BT$. In BLIP condition, the detectivity becomes:

  $$D^*_{BLIP} = \frac{\lambda_{peak}}{2hc}\sqrt{\frac{\eta_{peak}}{\phi_{back}}} \tag{2.47}$$

  In this expression, λ_{peak} and η_{peak} are respectively the peak absorption wavelength and value, ϕ_{back} is the flux of photon emitted by the background per unit area that impinges on the QWP. Equation 2.47 shows that the only free parameter we can tune to optimize D^*_{BLIP} is the peak absorption η_{peak}, as we usually target a specific wavelength and the background photon flux is imposed by the operation environment.

According to the definition of T_{BLIP}, which is the temperature for which the photocurrent generated by background temperature equals the dark current, we can estimate it by finding the temperature for which the photocurrent generated by the background photon equalizes the device dark current. It verifies:

$$\eta_w \tau_c \phi_{back} = 2\left(\frac{m_w k_B T}{2\pi\hbar^2}\right)^{3/2} \exp\left(-\frac{hc}{\lambda_{cut} k_B T} + \frac{E_f}{k_B T}\right) \tag{2.48}$$

where η_w is the absorption of one well. We know that η_w is linearly proportional to the doping, and then the Fermi level. We deduce that we have the maximum BLIP temperature when $E_f = k_B T$. We refer the reader to the literature for further detail on this calculation[81].

In this chapter we derived a model to estimate the main parameters translating the performances of QWP devices. Within our framework, we can calculate the potential taking into account the MBEs, the energy states, the absorption, the dark current and photocurrent, the responsivity and detectivity and the BLIP temperature. This model can be used to simulate existing structures or to design new optimum structures. For example, in the next chapter we will use it to present new designs and show that we can benefits from MBEs to improve the device performances. We also discussed the impact of the top metal coverage on the absorption and showed the important difference between the infrared and terahertz cases.

Chapter 3

Simulation results

3.1 Device Optimization

3.1.1 Well width

The THz QWPs in this study are based on the GaAs/$Al_xGa_{1-x}As$ material system, in which GaAs is the quantum well layer and $Al_xGa_{1-x}As$ is the barrier layer. The main task of THz QWP device design is to find the optimum well width for a given barrier height to maximize device detectivity at a design frequency. It is defined as the well thickness at which the first excited state in the well is in resonance with the top of the energetic barrier, under no bias condition. First, we calculated the the optimum well width for a given barrier height by using the ideal square potential only and ignoring the many-body effects. In a second step, MBEs were included in simulations to obtain self-consistent new wave functions and energy states and determine the optimum well width for each Al fraction. MBEs that are taken into account are detailed in subsection 2.2.3.

Figure 3.1 shows the correlation between Al fraction and well thickness when only the ideal potential (black curve) is taken into account as well as the corresponding absorption frequency (black values). The corrected peak absorption frequencies are written in red in figure 3.1. Peak absorption frequency is blue shifted after taking MBEs into account, agreeing with Graf[88]. The blue shift is slightly overestimated because the simulation does not include the exciton effect on the intersubband transition, which tends to red shift the absorption frequencies. Simulations also show that the first excited state becomes off resonance with the top of the energetic barrier under the influence of MBEs, thus significantly elongating carrier escape time and reducing photocurrent. To re-install the

resonance, new optimal well width needs to be identified in the context of MBEs. The blue curve in figure 3.1 shows this revised well thickness along with the corresponding corrected peak absorption frequency. MBEs render the quantum well effectively deeper, thus a narrower well is needed to raise the first excited state so as to re-align with the barrier top.

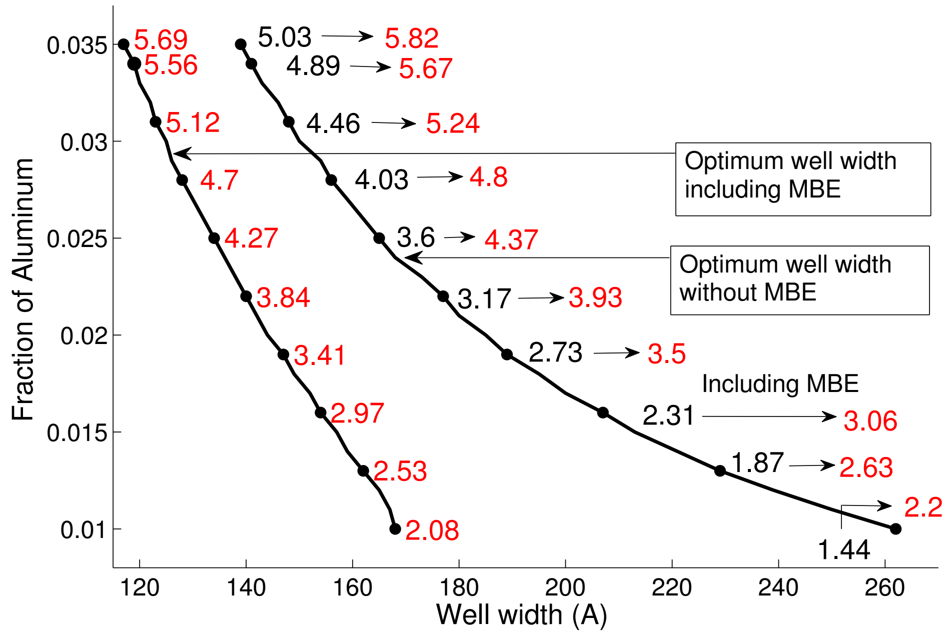

Figure 3.1: Optimum well width without and including MBE. Absorption frequency is indicated without (black) and including corrections (red). Doping is 4×10^{10} cm^{-2}.

For example, at Al fraction of 1.5 % one can note that the optimum well width is reduced from 213 Å to 157 Å before and after the consideration of MBEs. For a device with 23 modules[105], this well-width reduction means that total growth would be 1288 Å less or an extra module (1108 Å) can be fit in within the same target device thickness to increase the total absorption.

To better understand the impacts of doping density, designs with different sheet doping densities ranging from 10^9 cm^{-2} to 10^{11} cm^{-2} are simulated. The results are shown in figure 3.2. As expected, larger correction to the peak absorption peak is observed at higher doping densities. For commonly-used doping densities (mid-10^{10} cm^{-2}) and Al fraction (1% to 3%) the peak absorption frequency is blue-shifted by up to 20% before and after

considering . As the doping concentration increases to 10^{11} cm^{-2}, this blue shift becomes more prominent (dotted vs solid curves in the inset of figure 3.2).

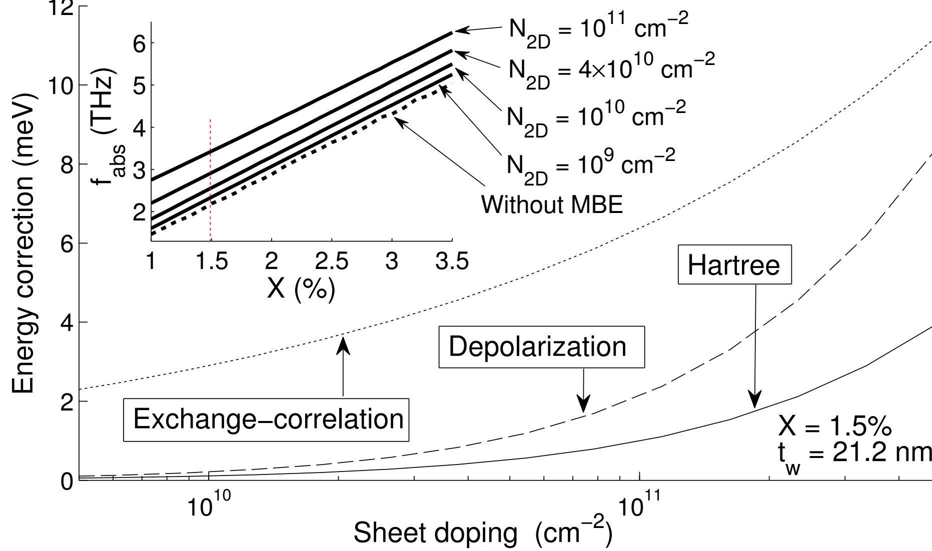

Figure 3.2: Evolution of Hartree, exchange-correlation potentials amplitude and depolarization shift with doping. Inset: Peak absorption frequency without MBE and with MBE for each fraction of Aluminum and different doping concentration.

The red curves in figure 3.2 shows the contribution of each part of many-body effects to the correction of intersubband transition energy (proportional to the peak absorption frequency shift). It represents the magnitude of V_H and V_{xc} as well as the depolarization shift defined by:

$$\Delta E_{dep} = E'_{21} - E_{21} = E_{21}\left(\sqrt{1+\alpha} - 1\right) \tag{3.1}$$

In this equation, E'_{21} is the optical transition energy when taking the depolarization into account and E_{21} is the transition energy without, α is the depolarization coefficient given by equation 2.10.

Exchange-correlation is shown to be the dominant effect, especially at low doping densities. The figure shows MBEs are clearly playing an important role in THz QWP designs, especially for low barrier heights. In this case V_H and V_{xc} tend to be comparable to, and even greater than, the natural conduction band offset (intrinsic energetic barrier height). Another important impact of the many-body effects is the energy state burying. In fact, the first excited state is below and thus lose its alignment with the top of the barrier because

of the additional Hartree and exchange-correlation potentials such as pictured in figure 3.3. This causes the wave functions to decay much faster in the barrier and increases the

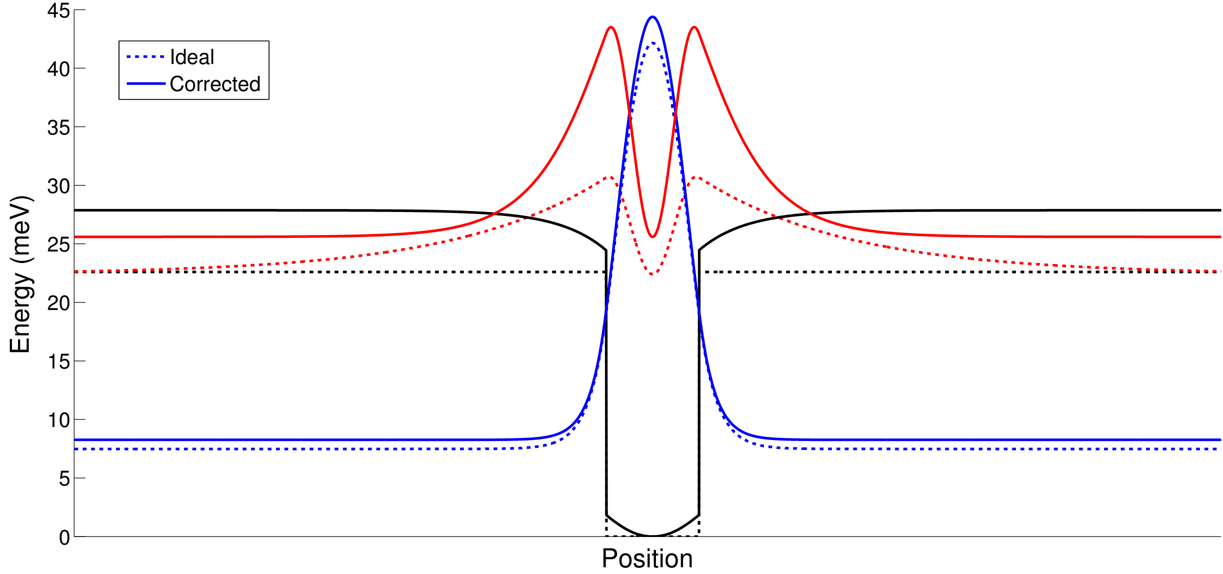

Figure 3.3: Potential and wavefunctions with (solid lines) and without (dashed lines) taking into account the MBEs.

oscillator strength by 60-70%. On the other hand, carrier escape time is much elongated, and as a result photocurrent decreases drastically. To address this issue, the well width has to be decreased to bring the excited state back to resonance. The left curve (blue) in figure 3.1 shows this new optimum well width.

3.1.2 Barrier width

In THz QWP[79] as in QWIP, the thickness of the barrier is of critical importance as regards the dark current. The thicker the barrier is, the smaller is the tunneling probability and then the tunneling component of the dark current. If the barrier is too thin, the tunneling component can become predominant compared to the direct thermionic emission. In this case the dark current does not decrease when we lower the temperature below a specific value. This is the "bottom-out" phenomenon[78]. In this situation, the device may not reach BLIP operation. In fact, the dark current is exponentially dependent on the temperature as we can see with equation 2.32, whereas the tunneling component is

constant with temperature. To avoid such a bottom-out behavior, a rule of thumb is to keep the simulated tunneling component one order of magnitude below the estimated dark current.

We represented on figure 3.4 the dark current and its tunneling component for barrier

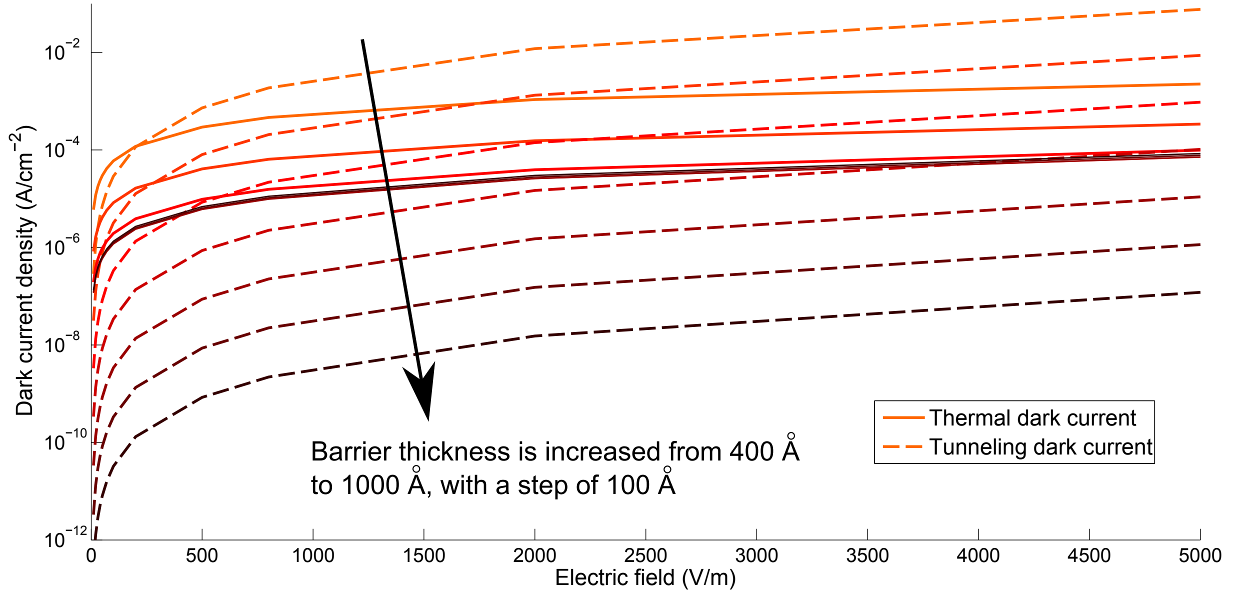

Figure 3.4: dark current density and it tunneling component for barrier thickness varying from 400Å to 1000Å with a step of 100Å.

thickness ranging from 400Å to 1000Å with a step of 100Å at a temperature of 7K.
From the figure, we verify that the thermionic emission is constant with barrier thickness for a barrier thickness greater than 600Å. While increase the barrier thickness from 400Å to 1000Å, the tunneling dark current density is reduced from 7.6×10^{-2} A/cm^2 to 1.2×10^{-7} A/cm^2, or more than 5 orders of magnitude. The value of 700Å appears to be a critical thickness for the barrier, below it the tunneling is more important than the thermionic emission and bottom-out phenomena will definitely occur.
As the barrier thickness is very large for THz QWP, the energy states of the neighboring wells are not coupled and then are not affected by the barrier thickness. If we reduce the barrier thickness, this assumption does not hold anymore. This explained that the thermionic emission for the two thinnest barriers (400Å and 500Å) is higher.

3.1.3 Operating temperature

Due to the shallow potential barrier which is typically around 25 meV, many parameters are very sensitive to temperature. In comparison, for a temperature of 11 K, $k_B T \approx 1\,\text{meV}$. This is especially noticeable with the dark current and the detectivity.
A correct estimation of the dark current dependence on the temperature is important to understand the behavior of the device at low temperature. For example it is required to estimate the detectivity at a given temperature or the BLIP temperature. As mention in subsection 3.1.2, the tunneling component of the dark current is weakly sensitive to the temperature unlike the thermionic emission which strongly depends on the temperature.

Figure 3.5 represented the dark current as well as its tunneling component for temper-

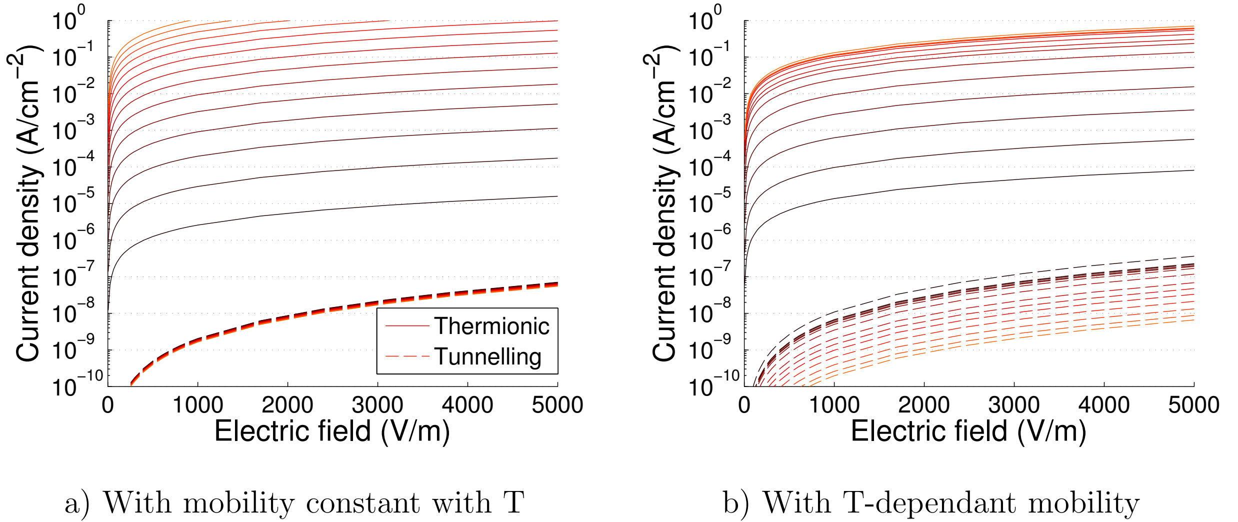

a) With mobility constant with T

b) With T-dependant mobility

Figure 3.5: Tunneling and thermionic components of the dark current for a temperature dependant and a constant mobility for temperatures varying from 7K (black) to 20K (red) with a 1K step.

atures from 7K to 20K with a step of 1K (red is for higher temperatures and black for colder temperatures).
If the mobility is assumed to be constant, as we expect from low temperature GaAs [106, 107], important discrepancy with the experimental data is faced. The usual value that is chosen in the literature is $\mu = 1 \times 10^4\,\text{cm}^2\text{Vs}^{-1}$. The resulting dark current is displayed in figure 3.5 a). As expected, we find that the tunneling component is independent of the temperature. Nevertheless the thermionic emission is importantly overestimated for high temperatures ($T > 12K$) and underestimated for low temperatures ($T < 11K$).

Tan reported that the multiple quantum well structure may introduce a temperature dependent mobility. As a consequence, he used the mobility as a fitting parameter to match the experimental data[80]. After reproducing his results, which are not taking the MBEs into account, we use this value of the mobility to estimate the dark current components. Results for both thermionic and tunneling components are reported in figure 3.5 b). The values for the dark current (solid lines) now match the experimental data. Furthermore, the tunneling component decreases by two orders of magnitude as the temperature increases from 7K to 20K. Nevertheless we can not entirely rely on this model for the mobility to design new structures. In fact, it has not been validate by other experiments involving different devices. In addition it would make the mobility changes over more than one order of magnitude, from 5.3×10^4 cm^{2}Vs^{-1} to 1.2×10^3 cm^{2}Vs^{-1}. This is very far from the expected constant value of $\mu = 1 \times 10^4$ cm^{2}Vs^{-1} for a small range of temperatures. Resulting simulation of the dark current using this model for new designs will be reported in subsection 3.2.4.

The detectivity is also very sensitive to the temperature. We simulated it for wavelengths

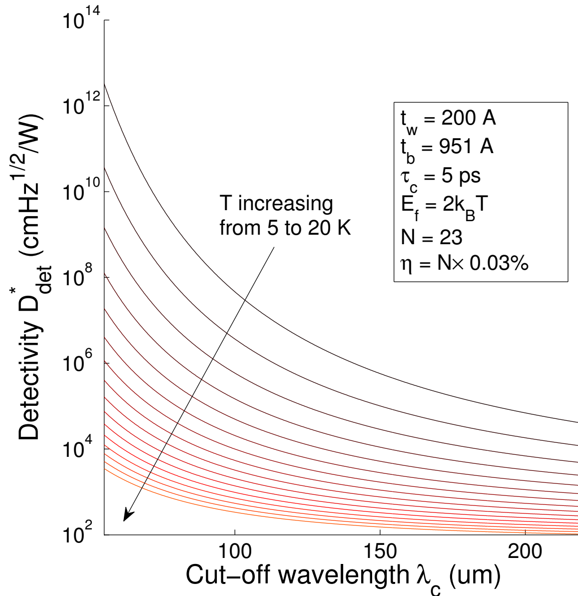

Figure 3.6: Evolution of the detectivity with cut-off frequency for temperatures varying from 5 to 20 K with a 1 K step.

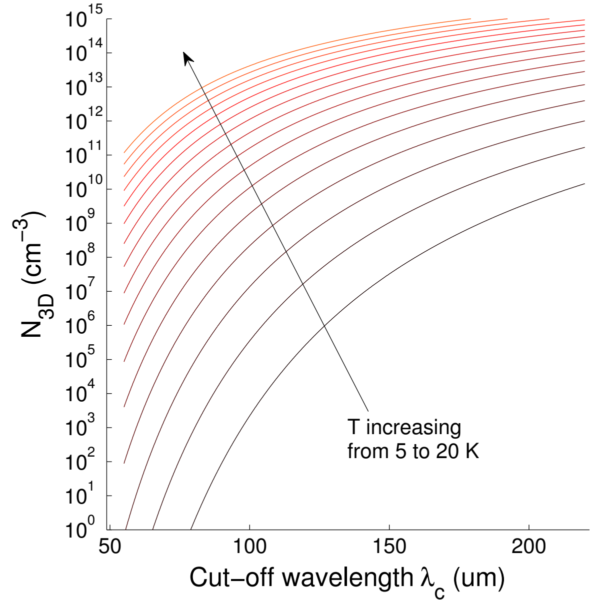

Figure 3.7: Evolution of the 3D thermally activated electron density above the barrier with cut-off frequency for temperatures varying from 5 to 20 K with a 1 K step.

ranging from 50 μm to 200 μm. The resulting detectivities are shown in figure 3.6. The

important and quick decrease of detectivity with the temperature is strongly correlated by the number of electrons thermally excited to the continuum. Their evolution is represented in figure 3.7 depending on the wavelength of absorption. The higher the target wavelength of absorption, the shallower is the barrier, and the easier it is for the carrier to escape to the continuum because of thermal energy. For this estimation, we assumed that we have 23 modules of length $L_p = t_w + t_b = 200 + 951 = 1151\mathring{A}$, a capture time of $\tau_c = 5\,\mathrm{ps}$, an absorption of 0.03% for each well and an optimum doping inducing $E_f = 2k_BT$. Within those approximations and in order to give a comparison, we obtain the same detectivity for a THz QWP with a cut-off wavelength of $80\,\mu m$ at 5 K and a QWIP with a cut-off wavelength of $14\,\mu m$ at 80 K. For a cut-off wavelength of $\lambda_{cut} \approx 110\mu m$ the detectivity decreases from $1.375 \times 10^7\,\mathrm{cm}\sqrt{\mathrm{Hz}}/\mathrm{W}$ to $266.9\,\mathrm{cm}\sqrt{\mathrm{Hz}}/\mathrm{W}$ when the temperature increases from 5 K to 20 K. A more accurate estimation should calculate the real capture time taking into account all the scattering processes, and the fact that the well width, barrier thickness as well as the absorption are not constant for different wavelengths.
Finally, we estimated the BLIP temperature of device V267[105] as we can compare our model to the experimental value of $T_{BLIP} \approx 12K$[80]. For our calculation we used the reported values of $\eta_w = 0.16\%$, $\lambda_{cut} = 1.1 \times \lambda_{peak} = 1.1 \times 80\mu m = 88\mu m$ and we assumed $\tau_c = 5$ ps, typical value for QWIPs (not measured yet for THz QWPs)[66]. Left-hand and right-hand side of equation 2.48 are shown in figure 3.8. The intersection of the curves gives T_{BLIP}. For our example we find $T_{BLIP} = 9$ K which is to compare to the experimental value of $T_{BLIP} = 12$ K. This is a satisfying result given the simplicity of the model and our assumptions.

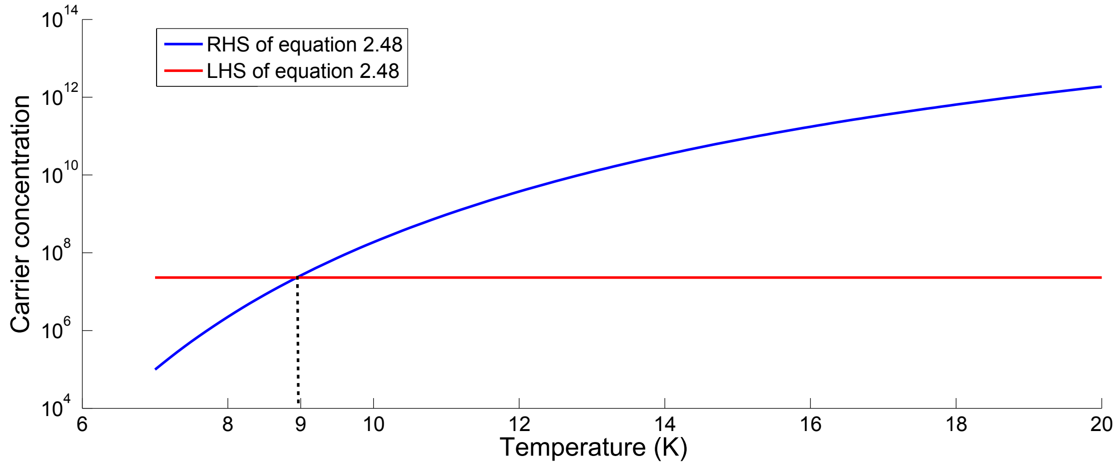

Figure 3.8: Density of carriers in the continuum excited by the background photons (red) and responsible of the device dark current (blue).

3.2 New Designs

3.2.1 Potential calculation

As seen in section 3.1.1 the many-particles effects have a dramatic impact on device performance of THz QWPs. By changing the doping distribution, the effective potential profile can be engineered to exploit MBEs and new device structures with improved performance is thus proposed and designed.

Device	t_w (Å)	t_b (Å)	X	L_{dop} (Å)	L_{space} (Å)	f_{abs}(THz)
S01	157	951	1.5	100	0	2.72
S02	180	951	1.8	100	$3.8\times L_{dop}$	2.77
S03	200	951	1.9	200	$4\times L_{dop}$	2.87
Ideal	188	951	1.9	100	0	2.73

Table 3.1: Studied designs, $N_{2D} = 4 \times 10^{10}\, cm^{-2}$ for all devices

Three THz QWPs designs with different doping profiles are designed with a target peak absorption frequency around 2.75 THz. Their design parameters are summarized in Table 3.1. S01, S02 and S03 are doped respectively in the center of the well, into and further into the barriers. For comparison, a fourth THz QWP (Ideal) was also simulated without MBEs. Their effective potentials and the lowest two wavefunctions are plotted in figures 3.9 to 3.12.

Those figures show the additional MBE potentials deviate the effective potential profile substantially from the ideal square potential (see figure 3.9 and 3.10). By splitting the dopant profile into two parts and move them symmetrically into the barriers, the deviation in potential profile can be substantially reduced (figure 3.11). In fact, V_{xc} is not changing as it depends mainly on the ground wave function, whereas V_H becomes positive in the center of the well when moving the doping out of the well and into the barriers, thus compensating for V_{xc}. The total effective potential is therefore modified back to the ideal square potential. If the doping profile is shifted further into the barriers (S03) V_H can overcome V_{xc} in the barrier, thus creating potential bumps close to the well as shown in figure 3.12. Then the structure could behave like a double barrier QWP[108] without having two barriers with different Al concentration, which simplifies the growth process.

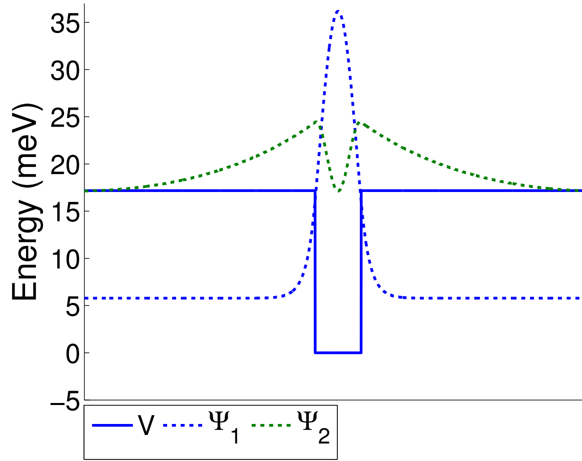

Figure 3.9: Potential of the ideal design.

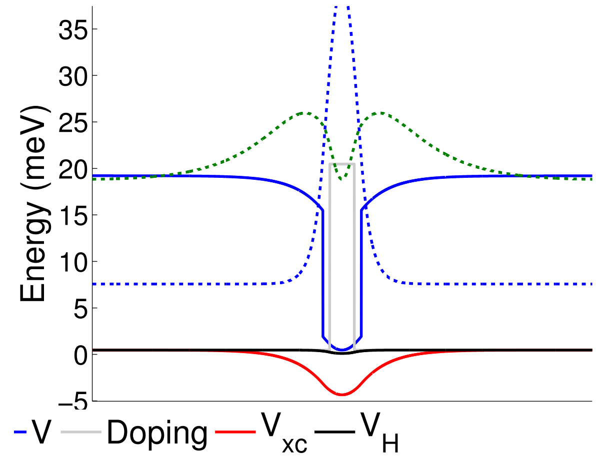

Figure 3.10: Potential of the design S01.

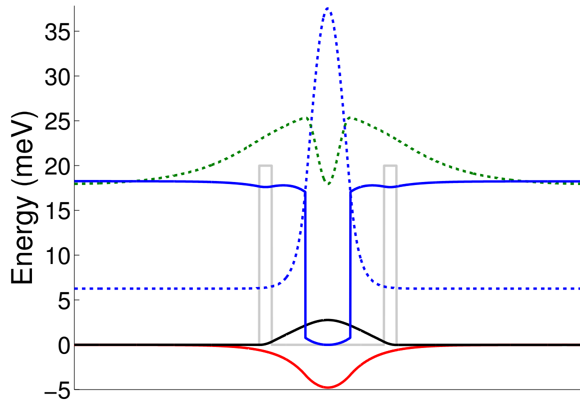

Figure 3.11: Potential of the design S02.

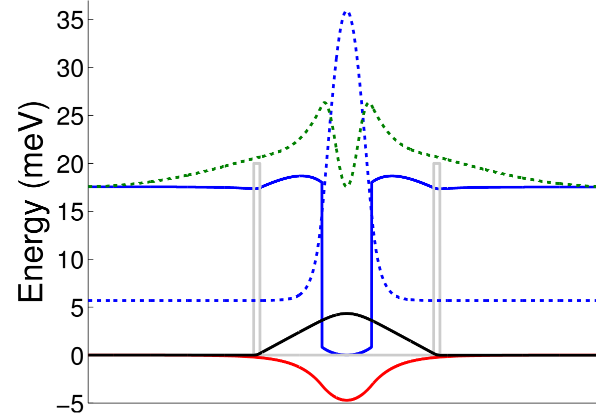

Figure 3.12: Potential of the design S03.

3.2.2 Absorption spectrum

The absorption spectrum has been calculated for each structure under a bias of $1.5 \times 10^4\,\mathrm{V.m^{-1}}$ and is represented in figure 3.13.

From this figure, we verify that the design peak absorption frequency is around 2.75 THz. The peak absorptions are slightly off 2.75 THz as the optimization of the well widths has been done at zero bias condition. Indeed the peak absorption frequency is not constant as the bias applied to the device increases. Figure 3.14 shows the dependency of the peak

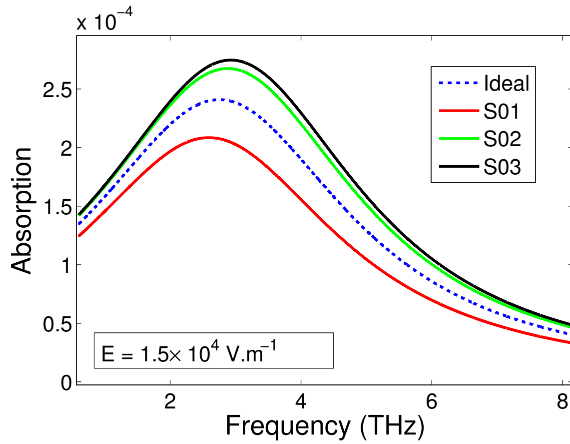

Figure 3.13: Spectra of absorption of each structure at $1.5 \times 10^4\,\mathrm{V.m^{-1}}$.

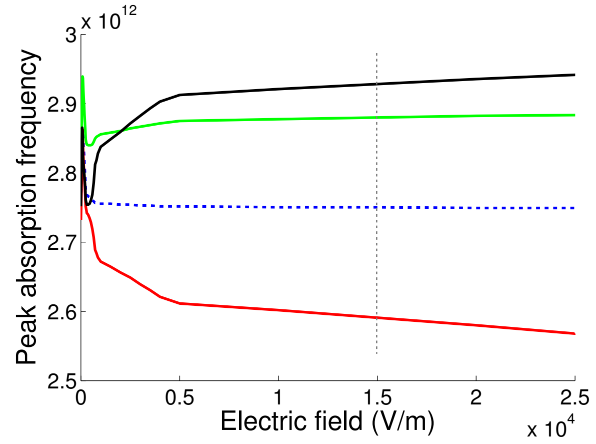

Figure 3.14: Peak absorption frequency evolution with the applied electric field.

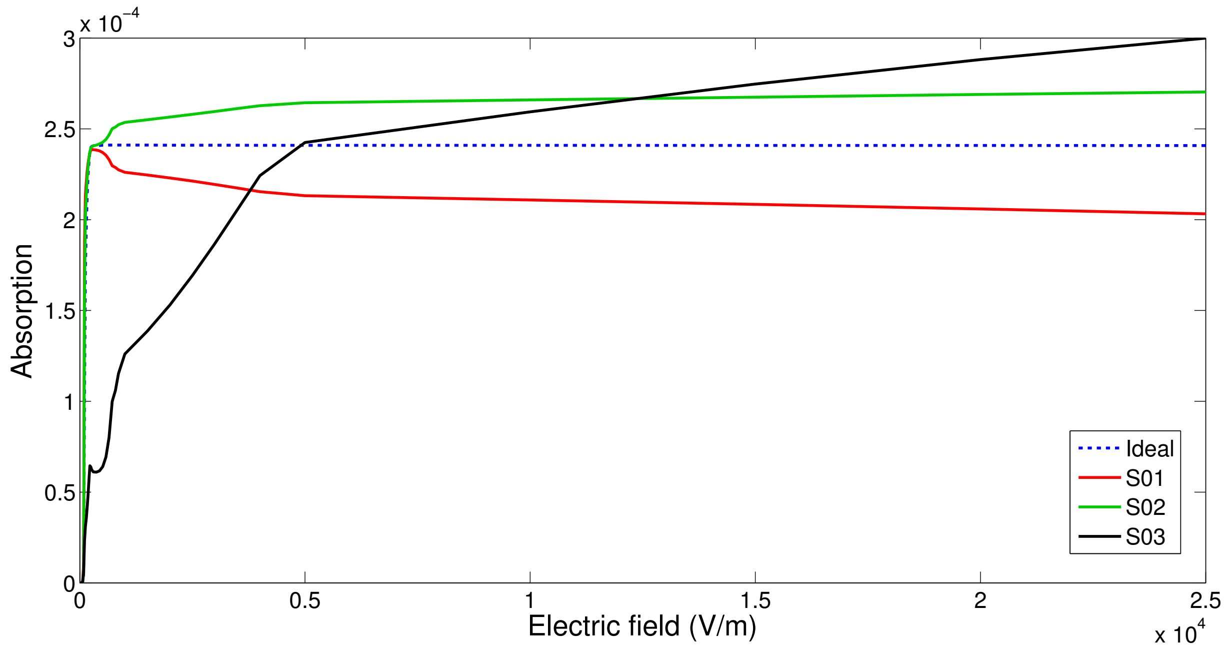

Figure 3.15: Evolution of the absorption with the electric field for each studied structure.

absorption on the electric field. We can notice that the absorption is lower than the ideal case when we include the many-body effects (S01). This is attributed to the fact that

the wavefunctions are more weakly confined as the potential barriers are thinner. S02 brings the peak absorption back to a value comparable, and even slightly higher than the ideal structure. This is because the potential barrier of S02 is very close to an ideal square barrier. The wavefunctions are then similarly confined for the both structures, thus resulting in a comparable oscillator strength and absorption. For the ideal structure as well as for S01 and S02, the absorption quickly converges to a stable value. Both S03 absorption and peak absorption frequency appear to be highly electric-field dependant. Actually, the wavefunction shape is strongly determined by the position of the energy state compared to the potential bump. Three cases can be distinguished:

- The excited energy state is below the potential bump. In this situation, the state is well localized inside the well in a similar way as with a square barrier.
- The state energy is located between the bottom and the top of the bump. In this case, special attention has to be given to the design. For specific well width, the wavefunction can be mainly localized between the right and left bumps of two adjacent modules, outside of the well. It would drastically reduce the oscillator strength and consequently the absorption.
- The energy state is above the bump, in the continuum. The results are then similar to bound-to-continuum devices.

If we want to maximize the confinement of the wavefunction, the energy state should be at the bottom of the bump. To rise it to higher energy allows to find a trade off between the absorption and the escape probability. In this sense, the potential bumps can be used similarly to the extra barriers of the double-barrier QWIP[108].
The evolution of the absorption with the electric field is represented in figure 3.15. Several observations can be made from this figure. First the ideal structure absorption is constant and equals to 2.4×10^{-4}. If we assume that we have 25 wells in our device, it yields a total absorption of 0.625%. This is a small value compared to QWIP that typically reach absorption around 25% but it agrees with the literature. The only restriction on the tuning of peak absorption frequency is the limitation of the growth quality. In fact, we assume that the smallest variation of the fraction of Aluminum that we can achieve with a good control is of 0.1%. As we have to change the well width to keep the excited state in resonance with the top of the barrier, it induces a discontinuous variation of the peak absorption frequency. For example, if a fraction of aluminum X_1 yields a peak absorption frequency of f_1 and the fraction $X_2 = X_1 + 0.1\%$ a frequency f_2 the frequencies between f_1 and f_2 will not be reachable.

3.2.3 Transmission probability of the barrier

The transmission coefficient $D(E)$ is a key parameter in the value of both the interwell tunneling and tunneling-assisted thermionic dark currents. This dependence is highlighted in the definition of the dark current by formula 2.24, and more specifically for the tunneling component by equation 2.28. We can note that the tunneling dark current is linearly proportional to the transmission coefficient. Considering that it varies over a broad order of magnitude range (typically from very small values, around $10^{-12} - 10^{-11}$, to unity), it is critical to achieve an accurate estimation of this coefficient. It is even more challenging as no simulation results as been reported for the transmission coefficient of QWP with non-squared potential barriers. Therefore, we chose to confirm the procedure described in appendix B with the ideal square potential barrier corresponding to the ideal structure detailed in table designs. In figure 3.16 we superimpose both the theoretical and numerical curves obtained respectively in solid red and blue circles.

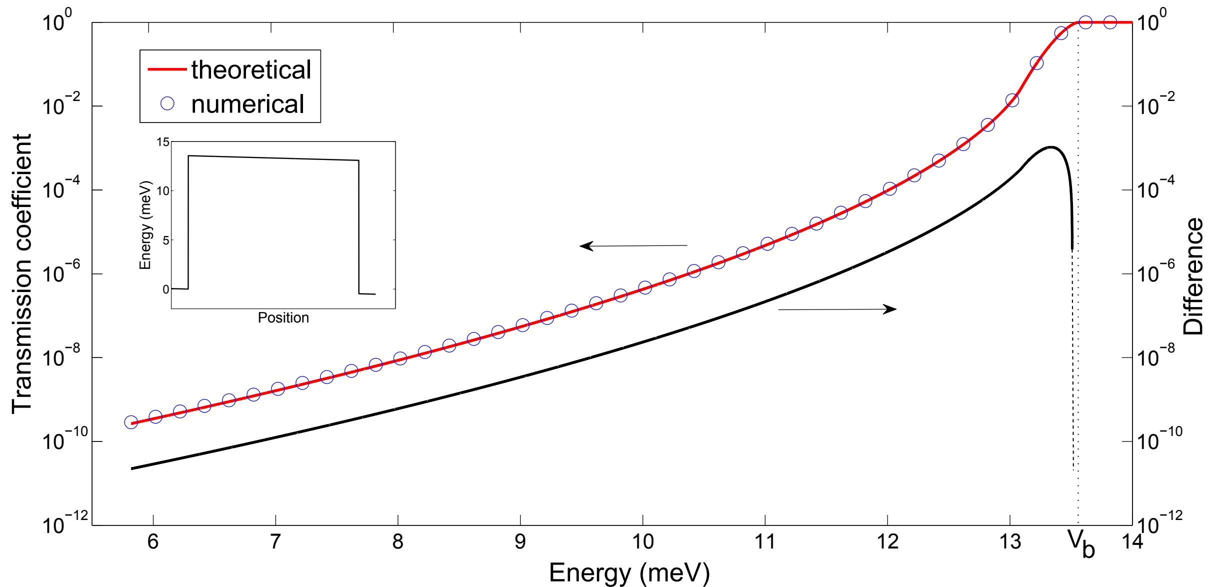

Figure 3.16: Comparison between the theoretical (solid red) and numerical (blue circle) calculation of the transmission coefficient with the WKB approximation (left side). The difference is represented in solid black with the right axis.

The values of the transmission coefficient are given on the left axis and span from $\approx 10^{-11}$ to 1. We do not start to calculate $D(E)$ at $E = 0$ but at $E = E_1 = 5.82\,\text{meV}$. In fact, the density of states below E_1 is zero, there is no electron to tunnel through the

barrier. As a consequence the knowledge of $D(E < E_1)$ is not required. On the right-side axis, we report the absolute difference between both approaches and represent it with the solid black curve. Good agreement is reached between the two estimations.
Our procedure being ascertained by this verification, we can calculate the transmission coefficients for the new design proposed in table 3.1. We represented them together in figure 3.17.

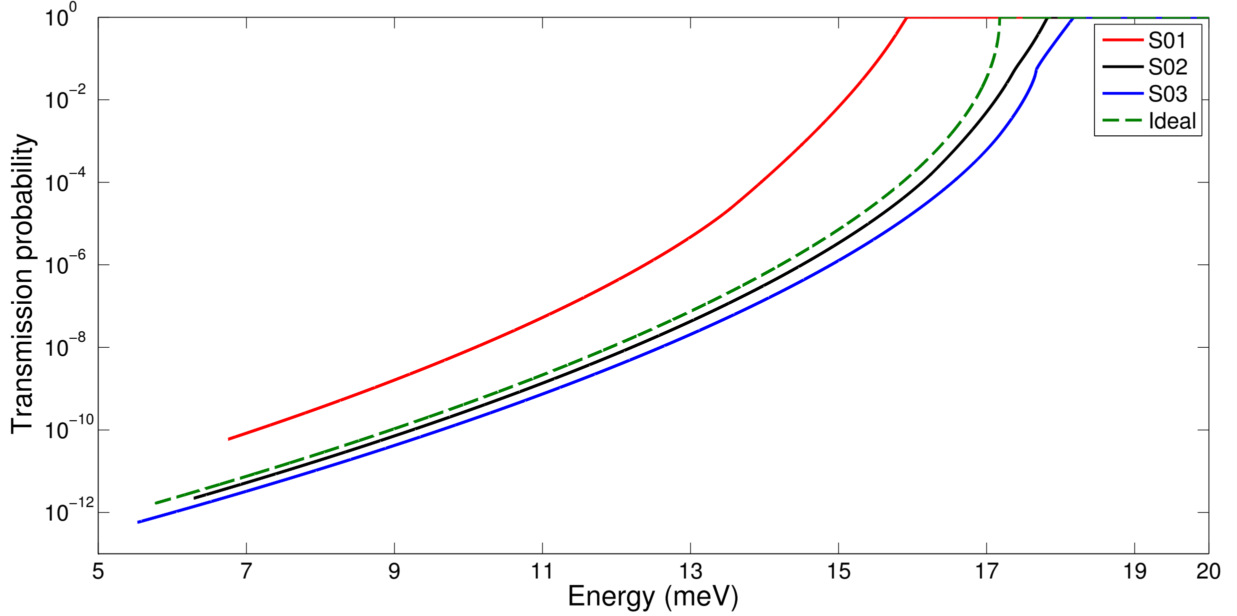

Figure 3.17: Comparison between the transmission coefficients numerically calculated with the WKB approximation for the proposed designs.

In light of this figure, several observations can be done about the transmission coefficient $D(E)$:

- it is importantly underestimated if we don't take into account the MBEs. $D(E)$ increases by more than one order of magnitude when the MBEs are included in the simulation ($D_{01}(E < V_b) \gg D_{id}(E < V_b)$). This is because the effective barrier thickness becomes smaller at the top of the barrier.
- the slope of $D_{01}(E < 0.9V_b)$ is larger than $D_{id}(E < 0.9V_b)$. The fact that the effective barrier thickness decreases with energy for structure S01 explains this trend.

- by shifting the doping to the side as with structures S02 and S03, we reduce $D(E)$ and its derivative away from V_b back to a value comparable to the square potential barrier. Here again it is because the effective barrier width is almost constant with energy and close to the ideal design.

- the differences between $D_{id}(E)$, $D_{02}(E)$ and $D_{03}(E)$ are located close to their respective barrier heights V_b, as in the case for their potential. As an example, the potential bumps on S03 barrier's sides make $D_{03}(E)$ reaches unity slower, translated by a lower slope close to V_b, compared to the ideal case.

We will see in subsection 3.2.4 that the impact of the transmission coefficient on the dark current is justified.

3.2.4 Dark current

The total dark current as well as its interwell tunneling component at 7K of the four structures in Table 3.1 were calculated and the results are plot in figure 3.18. As a rule of thumb, the tunneling component of the dark current should be kept sufficiently low (i.e. about one order of magnitude below the total dark current) to avoid bottom-out effects[78]. From the figure, one can note that this rule is satisfied in the ideal square potential case where MBEs are not included in the simulation. When the MBEs are included and the doping profile remains the same (such as S01), both the total dark current and its tunneling component are drastically increased, leading to deteriorated device performance. The overall effective potential in S02 is getting closer to the ideal square potential, thus its tunneling current component is reduced comparing to S01. Shifting dopant further apart into the barriers in S03, the tunneling component is further reduced to a level that is very similar to that of the ideal square potential case. More importantly, the total dark current in S03 is now lower than that of the ideal case, partially to its effective double barrier potential profile. According to section 3.2.2, the absorption is similar for S01 and S03, but the dark current of S03 is one order of magnitude lower than that of S01. As a result, the detectivity of S03 will be at least three times as that of S01 ($D \propto \eta/\sqrt{j_{dark}}$).
We can note that the correlation between the dark current and the transmission coefficient that we expect from subsection 3.2.3 is justified.
In the light of this results, we can underline another consequence as regards the design of the barrier thickness. In fact, if we compare S02 dark current and the tunneling component we can see that the later one is lower by more than one order of magnitude. It means that the barrier is unnecessarily thick and it length can be reduce. By doing so, we can either

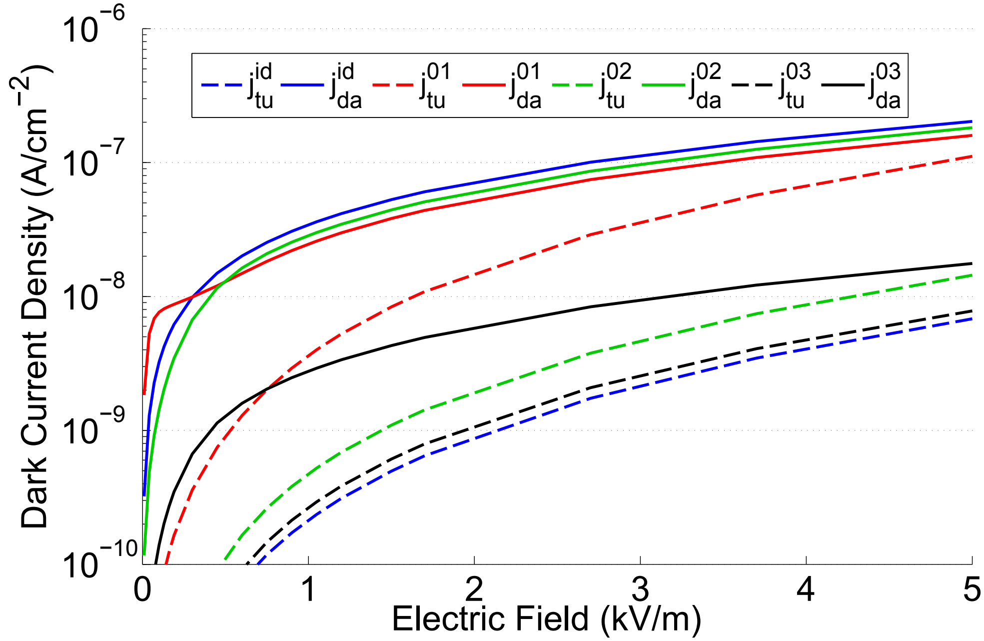

Figure 3.18: Total and tunneling part of dark current at 7K. By shifting the doping, we decrease the dark current by one order of magnitude.

reduce the total length of the device or fit more wells inside the active region without fear of experiencing bottom-out effect at lower temperatures.

3.3 Limits of bound-to-quasibound QWP and future designs

3.3.1 Very low frequency QWPs

One challenge for the next generation of QWIP is to reach lower frequencies of absorption. In fact it becomes very difficult to efficiently design devices targeting peak absorption frequencies below 3 THz for several reasons.
The first hurdle we meet when lowering the absorption frequency is related with the height of the barrier. In fact, as the excited state as to be in resonance with the top of the barrier, the potential becomes very shallow. This has different drawbacks related with the design and fabrication.

- The control of the aluminum fraction and migration during the growth is even more critical. To reach very long wavelength, typical fraction of aluminum is below 1%.
- The barrier being lower, thermionic emission is easier which causes an important increase of the dark current. To reduce this thermally-activated dark current to a practical value, the device has to be cooled down to lower temperature. Liquid Helium is reaching its limits and other cooling systems have to be taken into account. Nevertheless, these systems are bulkier, more expensive and more difficult to set up, which shifts further away THz QWP from commercial applications.
- The absorption is also importantly lowered. In fact, according to equation 2.22 and 2.23, the absorption of each well linearly depends on the doping and the energy of the optical transition with are both diminishing. In addition the barriers and wells thickness are increased, as a consequence less wells can be used as we do not want to increase the total width of the device. It results an additional reduction of the total absorption.
- In relation with the decrease of those parameters, we have seen in subsections 2.5.4 and 3.1.3 that the detectivity decreases exponentially as the wavelength of detection increases.

Another concern is that when we target such low frequencies of absorption, it can be hard to even reduce the height of the potential barrier because of the many-body effects. Indeed, the MBEs introduce a potential that is superimposed to the ideal square potential. This effect is maximum is we uniformly dope the center of the well. To illustrate this limitation we simulated a non-realistic device with a well width of 280, a barrier thickness of 951, an aluminum fraction of 1% and a sheet doping density of $4 \times 10^{10}\,\mathrm{cm}^{-2}$. We calculate the potential without including the MBEs and taking them into account with a uniform doping in the center of the well and inside the barrier. Results are shown in figure 3.19. If the doping is in the center of the well, as it is usual with the THz QWPs presented in the literature, the accumulated additional potential introduced by the MBEs is around 4.93 meV whereas the ideal potential barrier is 9.06 meV. In other word, the barrier height is increased by 54.3%. If we adopt the strategy developed in section 3.2 and shift the doping to the barrier we can reduce this discrepancy. The extra potential added by the MBEs is now only of 0.84 meV, or 9.32% of the ideal barrier.

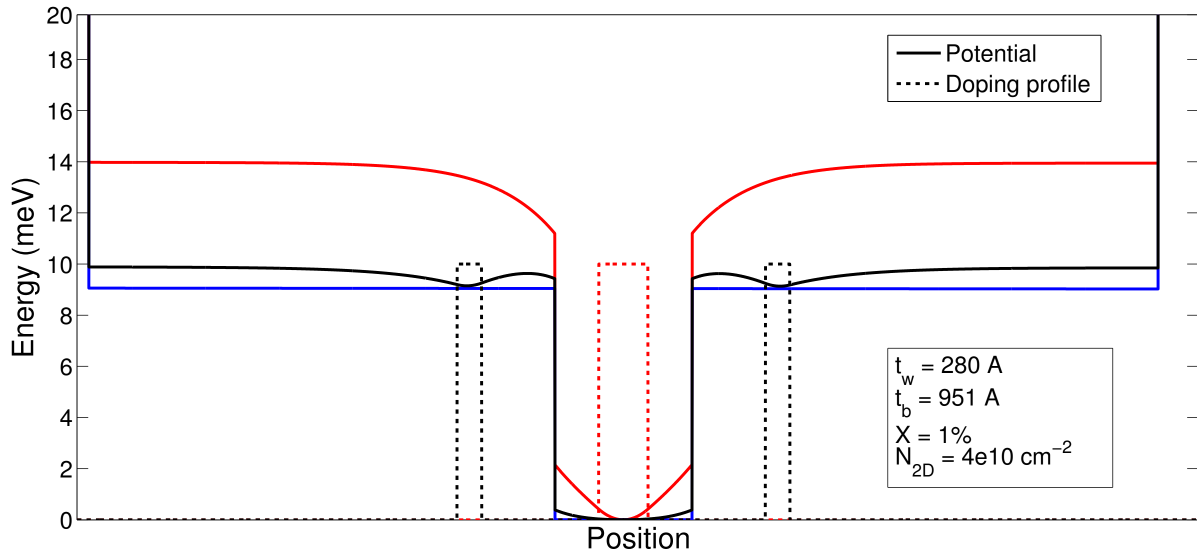

Figure 3.19: Potentials calculated for the design presented in the text box, without including the MBEs (blue) and with them, doping being either in the center of the well (red) or in the barrier (black).

3.3.2 New designs

The very shallow barrier appears to be a problem as seen in the previous part. This limitation is inherent in the actual THz QWP and QWIP structure. Innovative devices have to be develop in order to alleviate this issue. In this section, we study the possibility to adapt designs used in the infrared region, and mentioned in section 1.3.2, to the terahertz range. The potentials, energy states and wavefunctions of three of them have been simulated: the THz QCD and the bound-to-miniband and phonon-assisted band-to-miniband THz QWP. For those devices, the barrier is much higher than for a standard THz QWP. In fact the fraction of aluminum is varying from 8% to 15% compared to 1% to 3% for a THz QWP. In particular it induces that the impact of MBEs is much less in comparison with the shallow barriers THz QWPs.

Terahertz Quantum Cascade Detectors

A first alternative is to turn to the THz QCD. In fact it has been the first design proposed to sense THz radiation with a MQW structure, reported by Graf *et al*[64]. They achieved

a good detectivity (5×10^7 cm$\sqrt{\text{Hz}}$/W) despite the low responsivity (8.6 mA/W) and managed to detect signals up to 50 K.
For the device we simulated, the layers are (in Å): **24**/ 300 / **35** / 140 / **50** / 155 / **40** / 172 / **38** / 190 / **36** / 220 where barriers are in bold characters. The aluminum fraction is $x = 15\%$. The resulting potential and wavefunctions of one module are plotted in figure 3.20. The energy of the optical transition is 14.39 meV (3.48 THz).
The optical transition happen between the states $A7$ and $B1$, the excited electron then cascades along the states $B1$ to $B7$. For the QCD operating in the infrared range, the transition between two states of the cascade relies mainly on LO-phonon transition. Nevertheless, the energy of the optical transition is below the LO-phonon energy for terahertz absorption. It is typically around 5-15 meV whereas the LO-phonon energy is of 36 meV for GaAs . Then, this cascading is taking place by electron-electron scattering which is much slower than the LO-phonon scattering, as a result it is difficult to efficiently extract the electrons from the excited state $B1$ to the next ground state $B7$.
The greatest advantages of this structure is that it can be operated at zero bias, as a consequence the dark current is much lower leading to higher potential maximum temperature and better detectivity (despite a lower responsivity). In addition, the continuum does not have to be taken into account as the transitions always occur between bound-states. It greatly reduce the complexity of the modeling. We also benefits from the work done on QCL as they have a nearby operation principle and theoretical modeling. However QCDs are facing a lower quantum efficiency compared to QWIPs. QCD theory has been recently studied by Delga[109, 110].

Bound-to-miniband THz QWP

Another design that has been tried in the infrared range is the bound-to-miniband active region. We have adapted this scheme to the THz range and propose a design for THz GaAs bound-to-miniband QWP. It is based on the following layer thicknesses for one module: **70** / 320 / **60** / 195 / **70** / 195 (in Å, barriers are in bold). The corresponding fraction of aluminum are 8 / 0 / 8 / 0.8 / 8 / 0.8 in %. A different fraction of aluminum has been used for wells that are not involved in the absorption but only in the carriers transport in order to reduce the tunneling between adjacent ground states. The resulting potential and energy states are shown in figure 3.21 and the corresponding wavefunctions in figure 3.22. The energy of the optical transition is between 10.8 meV and 12.5 meV (corresponding to 2.61 THz and 3.02 THz). In fact, as they couple together, excited energy states are splitting and occupy a broad range of frequency, over 1.7 meV (or 412 GHz). Even more spreading of the excited miniband is expected for realistic devices with more modules.

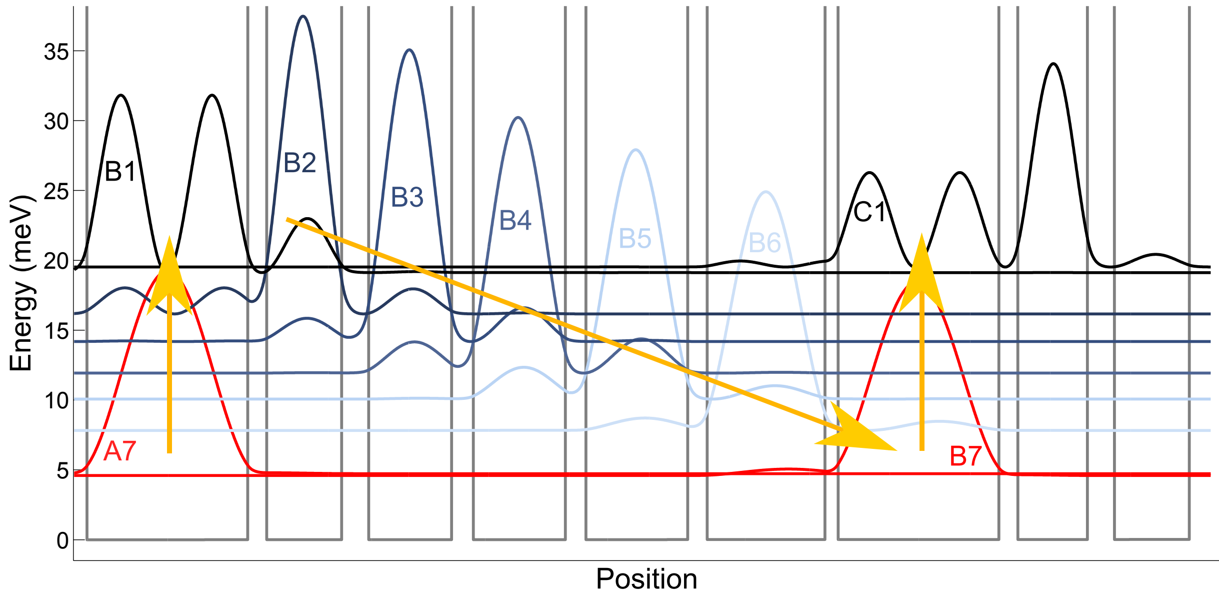

Figure 3.20: Quantum cascade detector in the terahertz range.

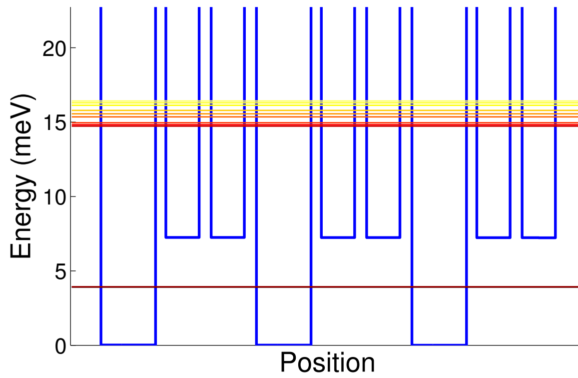

Figure 3.21: Band diagram of a bound-to-miniband THz QWP representing the energy states.

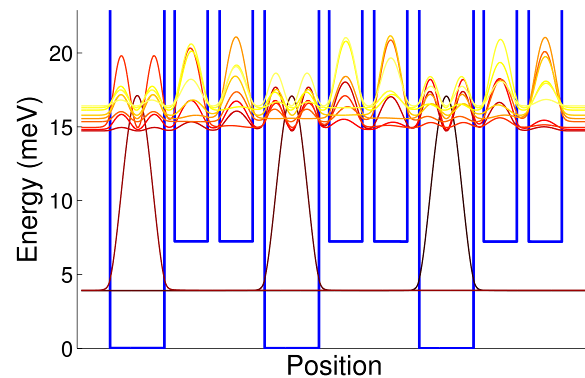

Figure 3.22: Band diagram of a bound-to-miniband THz QWP representing the wavefunctions.

Phonon-assisted band to miniband

This innovative design is relying on a bound-to-miniband followed by a phonon transitions and operates under an electric-field. It is closer to the mechanism of a QCL. We show in

figure 3.23 a proof of concept device potential and wavefunctions. The layers are 318 / **85** / 92 / **85** / 86 / **85** / 75 / **85** / 68 / **85** / 62 / **85** and the fraction of aluminum is of 9%. A realistic design would require design optimization. The electron is excited from the ground state of the larger well to the excited state of the same well, couple with a miniband. The electron is then extracted from this miniband to the next ground state by LO-phonon relaxation. In fact, the energy difference of the miniband and the ground state of the next module is equal to the LO-phonon energy in GaAs , $E_{LO} = 36$ meV. An issue could be the leakage paths indicated in red, from miniband to miniband through states 2 or 3 of the larger well.

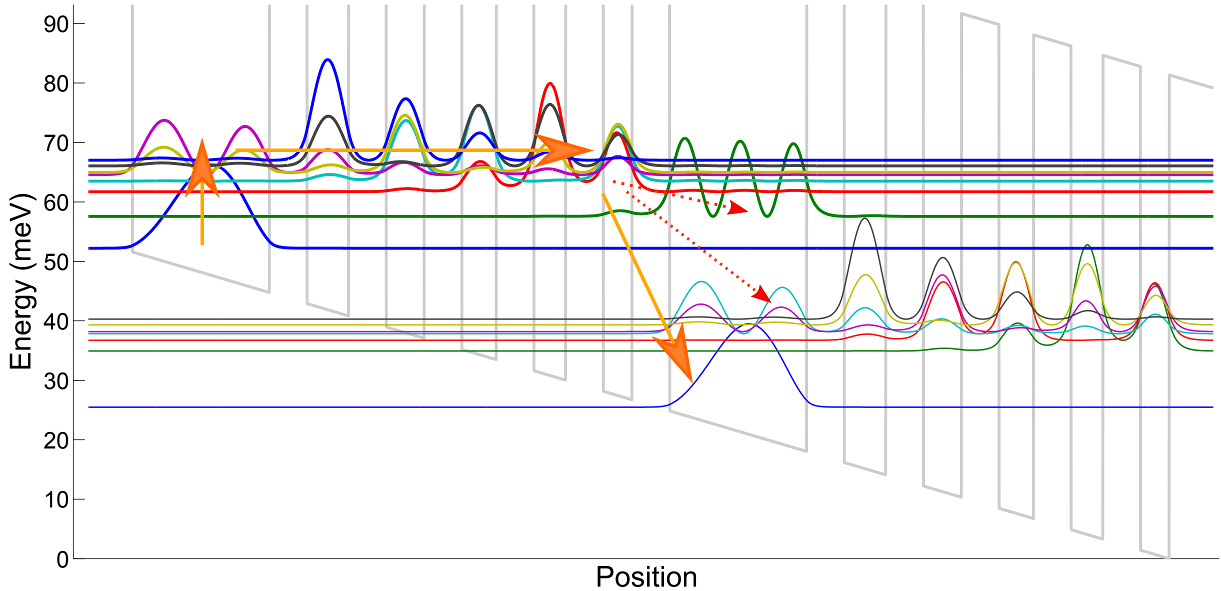

Figure 3.23: Phonon-assisted band to miniband detector in the terahertz range.

In chapter 3 we reported the simulation results we obtained with our framework. First we showed how to design structures with optimum well and barrier width as well as the possibility to quantify the impact of the temperature on the performances with our model. These results have been presented at CLEO 2013 conference[111]. We then proposed new designs that benefits from MBEs to reduce the dark current and thus increase the detectivity. To our knowledge, this is the first time MBEs are used as an advantage to design QWP devices, they are usually an obstacle that moves away the devices from the targeted performances. We reported this principle to take advantages of MBEs to improve the performances in *Applied Physics Letters*[112]. Finally, we adapted some devices that had been used in the infrared range to the terahertz domain.

Chapter 4

Conclusion and future work

The technologies to detect THz radiations are still underdeveloped. This is in part due to the lack of convenient devices to emit at those frequencies, but to the lack of practical detectors. The development of thus components would boost the use of THz technologies for many applications, including homeland security, biomedical imaging, very high-speed wireless telecommunications or spectroscopy. In regards to fill this "THz gap" the performances of actual detectors need to be improved. Considerable progress has been made with the development of THz QWP devices. Nevertheless, the underlying physics and the impact of the active design on the performances remain not completely understood or predictable.

In this thesis we reported the implementation of a framework to simulate and improve the design of QWP devices in the THz range. Matlab code was written not only to simulate given active region but also to find optimum design parameters. The functions that were implemented are commented and reusable for potential future work on this subject.

We first described the working principles of QWPs. We derived one model to design THz QWPs main parameters, especially the well and barrier thicknesses, the doping and the fraction of aluminum. Special attention was given to the energy potential calculation by including the MBEs. Light coupling into the devices was discussed. The profile of the electric field power density inside the devices was estimated and shown to be totally different compared to QWIP devices. To the opposite to actual habit, it is shown that the top contact can cover more than half the mesa area. Finally methods to calculate the usual figures of merit were given. It includes the absorption, dark current and photocurrent,

responsivity, detectivity and operating temperature of the devices. Compared to models in the literature, we were able to calculate the dark current for arbitrary potential shapes, in particular the transmission coefficient could be calculated for non-square potentials. This is the first time that dark current simulations for THz QWPs taking into account the many-body effects are reported.

In a last chapter, we reported simulation results obtained within this framework and compared them to the literature. Therefore, we were able to simulate ab initio the peak absorption frequency, the dark current and especially its tunneling component and the electric field power density distribution in the device. We also wrote routines to estimate the absorption spectrum, the detectivity and the BLIP temperature by building on experimental parameters reported in the literature. New designs benefiting from MBEs were presented. They were shown to reduce the dark current by one order of magnitude and thus increase the detectivity by three times. Relying on our simulations, we shed the light on some limitations that will be encountered for lower peak absorption frequencies. We proposed designs with different carrier transport mechanisms that could palliate those shortcomings.

Overall, this work showed how to more accurately model THz QWPs. Especially, progresses were made for the simulation of the dark current components. Thus, for the first time to our knowledge the transmission coefficient was calculated for arbitrary potentials, leading to better estimation of the tunneling and thermionic dark current paths. To be able to include arbitrary potentials is critical when we take into account the many-body effects. In fact, they make the potential to be non-square and thus it was not possible to calculate the dark current with the state-of-the-art models. For the first time to our knowledge, a side-doped Thz QWP design was proposed showing better performances from our framework. Indeed, by shifting the doping we were able to change the potential by using the many-body effects. According to our simulations, the dark current was reduced by one order of magnitude and then the detectivity increased by a factor 3. Designs to realize bound-to-miniband and phonon-assisted band-to-miniband are proposed for the first time.

Finally to follow the research on THz QWPs we can distinguish two directions to work on in the future.

On the one hand, the model can be changed in order to be more accurate and to be able to calculate more parameters. Especially, we think that rate equations and density matrix models could lead to better results and understanding of the physics behind THz QWPs, as it has been the case for THz QCLs. The rate equation model has been mainly studied

by Jovanović *et al.*[113, 114] and Trinité *et al.*[83] for QWPs in the infrared range. To our knowledge it has never been applied to THz QWPs. Likewise, the density matrix model has never been used for THz QWPs. Further improvement of the model might also be reached by taking into account the diffusion of the dopant during the growth of the device. In fact, the doping profile has been shown to have a critical impact on the potential shape and, as a consequence, on the design. In addition, it has been shown that QWIPs undergo electric field domains, causing non periodicity in the potential shape, especially for the wells close to the contacts. Deeper understanding of these phenomena would also help to design devices with better performances.

On the other hand, samples have to be grown, fabricated, packaged and characterized to confirm, or invalidate, our new designs. In fact, we have been able to confirmed our model with experimental data reported in the literature for standard designs. Nevertheless we are not sure how accurately the MBEs can be manipulated to tailor new designs. We made THz QWP devices and their fabrication is detailed in appendix D. The device characterization is ongoing and the resulting experimental data will be used to confirm our simulation results in near future.

APPENDICES

Appendix A

Imaging experiments

A.1 Transmission mode

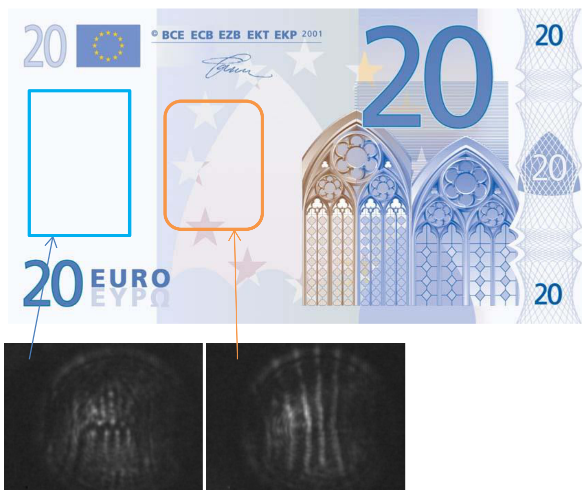

Figure A.1: 20 euros banknote in transmission mode

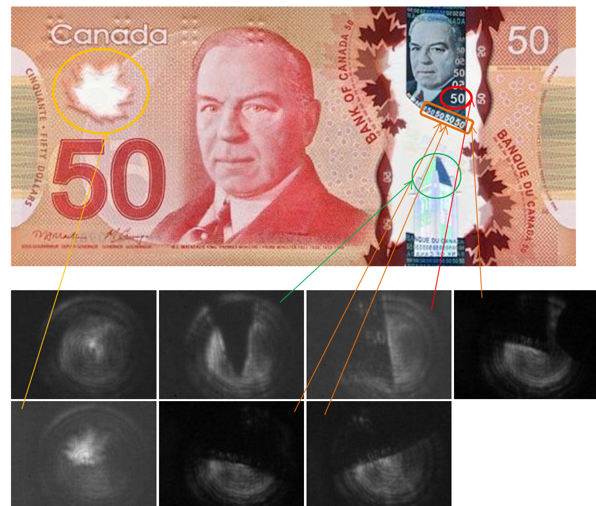

Figure A.2: 50 Canadian dollars banknote in transmission mode

In this section we report additional results that we obtain as regards terahertz imaging. We studied in transmission mode banknotes from different countries made of various materials. In 20 euros banknote (figure A.1) we manage to identify architectural structures such as an abbey and pillars. Through new polymer-made 50 Canadian dollars banknote,

we resolved tower steeple, numbers and maple leaf such as indicated in figure A.2. With

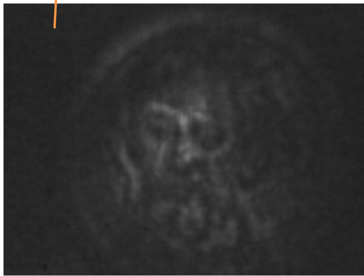

Figure A.3: 2 Argentinian pesos banknote in transmission mode

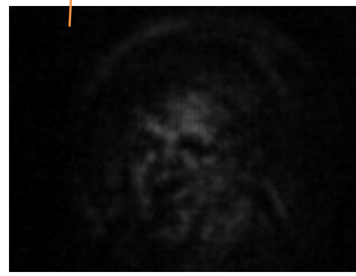

Figure A.4: 10 pesos Argentinian pesos banknote in transmission mode

2 and 10 Argentinian pesos banknote, we recognize respectively the watermarked faces of Bartolomé Mitre and Manuel Belgrano.

A.2 Reflection mode

We also conducted experiments in reflection mode. The setup is described in figure A.5. A piece of wafer has been used to align the system. The studied sample was a 1 Canadian dollar coin. From figure A.6 we see that we can resolve the duck. In reflection mode, the difficulty to align correctly the system and the diffraction effects tend to decrease further the image quality.

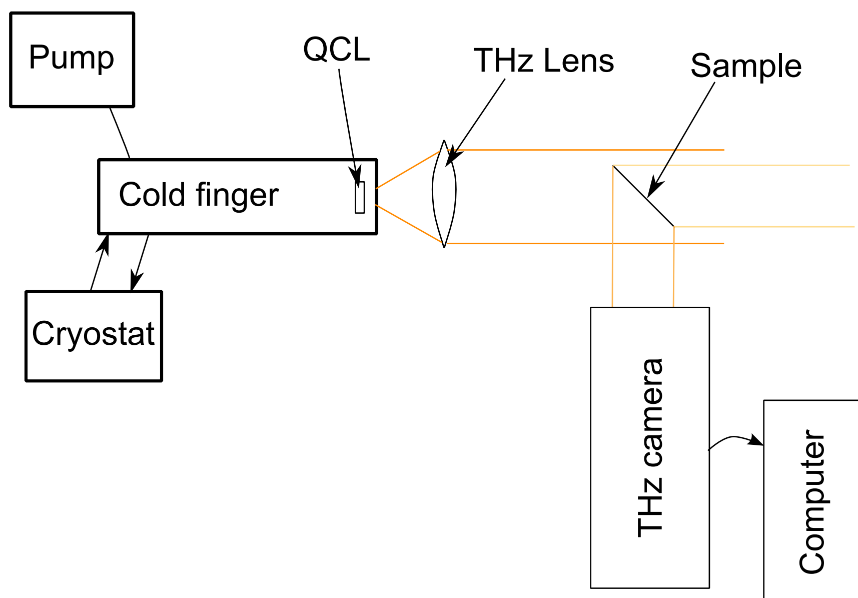

Figure A.5: Imaging experiments setup in reflection mode

Figure A.6: Imaging experiments in reflection mode with a 1 Canadian dollar coin

Appendix B

Transmission Coefficient Derivation in the WKB approximation

B.1 Square barrier

We consider a square barrier potential such as pictured in figure B.1. By solving Schrödinger

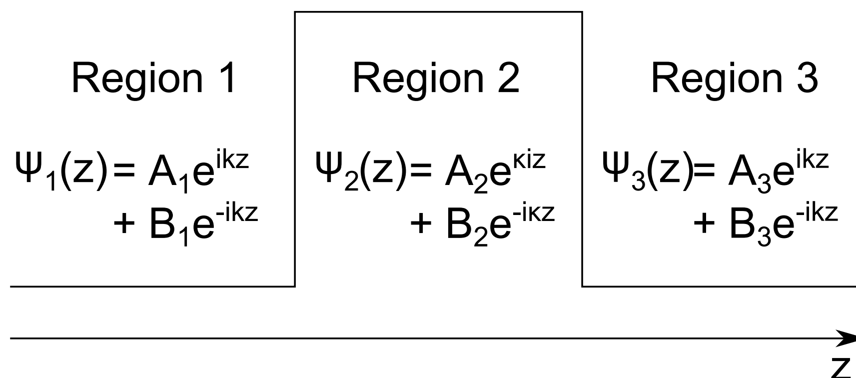

Figure B.1: Square potential barrier and wavefunctions corresponding to each region

equation, we find the stationary states in each region:

$$\Psi_1 = A_1 e^{ikz} + B_1 e^{-ikz} \tag{B.1}$$

$$\Psi_2 = A_2 e^{i\kappa z} + B_2 e^{-i\kappa z} \tag{B.2}$$

$$\Psi_3 = A_3 e^{ikz} + B_3 e^{-ikz} \tag{B.3}$$

where $k = \sqrt{2m_w E}/\hbar$ and $\kappa = \sqrt{2m_w(V_b - E)}/\hbar$. We assume that there is no wave incoming from the right side ($B_3 = 0$). We use the continuity of $\Psi(z)$ and $\dfrac{\partial \Psi(z)}{m^*(z)\partial z}$ at each interface ($z = 0$ and $z = t_b$) to find the transmission coefficient:

$$T(E) = \left|\frac{A_3}{A_1}\right| = \frac{4E(V_b - E)}{4E(V_b - E) + V_b^2 \sinh^2(\kappa t_b)} \tag{B.4}$$

$$\approx \frac{16E(V_0 - E)}{V_0^2} e^{-2\kappa t_b} \tag{B.5}$$

The approximation holds when we have a thick barrier ($\kappa t_b \ll 1$) and $E(V_b - E) \ll V_b^2 \sinh^2(\kappa t_b)$.

B.2 Arbitrary barrier

We divide the potential in $N = \dfrac{z_2 - z_1}{\mathrm{dz}}$ steps and assume the potential is constant over each dz subdivisions such as shown in figure B.2. Within the approximation of a thick

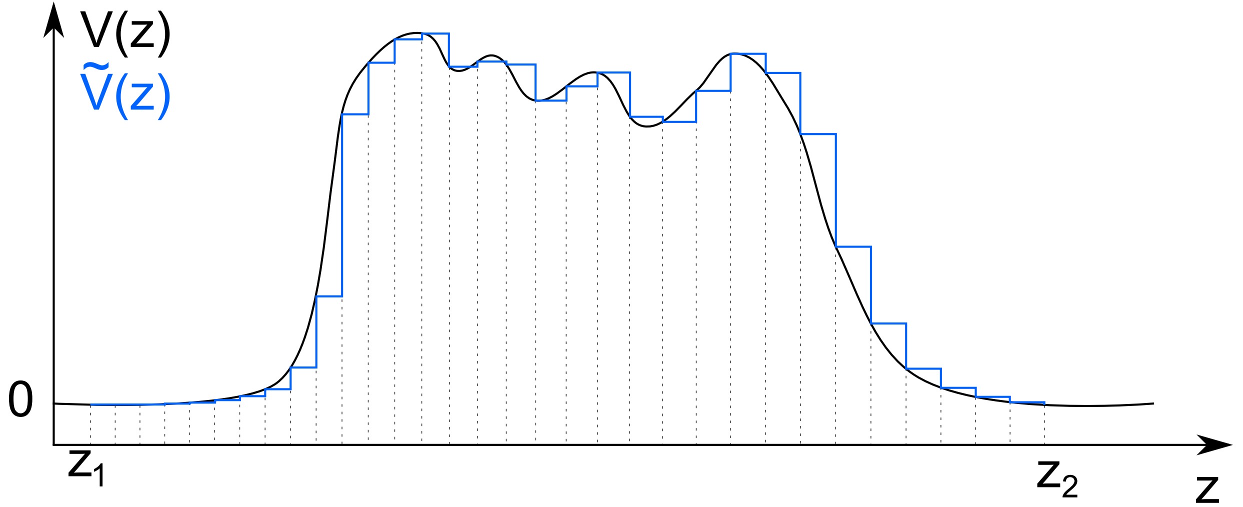

Figure B.2: Discretization of the potential barrier for an arbitrary shape

barrier, we can further simplify the transmission coefficient of equation B.5 into:

$$T(E,z) = e^{-2k(z)\mathrm{dz}} \text{ with } k(z) = \frac{\sqrt{2m^*(z)\,(V(z)-E)}}{\hbar} \tag{B.6}$$

$m^*(z)$ and $V(z)$ are the electron effective mass and potential at position z. The probability of finding the electron at $z + \mathrm{d}z$ is its probability to be at x multiply by the transmission probability:

$$P(z + \mathrm{dz}) = T(z)P(z) \tag{B.7}$$

We apply the logarithm function to solve this equation, and by defining $\widetilde{P} = \ln P(z)$ and $\widetilde{T} = \ln T(z) = -2k(z)\mathrm{dz}$:

$$\mathrm{d}\widetilde{P} = \widetilde{P}(z + \mathrm{dz}) - \widetilde{P}(z) = -2k(z)\mathrm{dz} \tag{B.8}$$

Which is integrated from z_1 to z_2 to get the resulting transmission coefficient:

$$\widetilde{T}(E) = \ln \frac{P(z_2)}{P(z_1)} \tag{B.9}$$

$$= \widetilde{P}(z_2) - \widetilde{P}(z_1) \tag{B.10}$$

$$= -2\int_{z_1}^{z_2} k(z)\mathrm{dz} \tag{B.11}$$

We finally deduce the transmission coefficient for the barrier:

$$T(E) \approx \exp\left(-2\int_{z_1}^{z_2} \frac{\sqrt{2m_e(z)(\widetilde{V}(z) - E)}}{\hbar}\mathrm{dz}\right) \tag{B.12}$$

The integral is evaluated numerically for energies from the ground state to the barrier height V_b. $T(E)$ is set to 1 for $E \geq V_b$.

Appendix C

Interferences phenomenon in the active region

C.1 Power density of the electric field growth axis component

In case we have a metal covering the whole device, the electric field can be written:

$$\mathbf{F}^m = \begin{pmatrix} F_x \\ F_y \\ F_z \end{pmatrix} = 2F \exp\left(ik_x x - i\omega t\right) \begin{pmatrix} i\cos\theta\sin(k_z z) \\ 0 \\ \sin\theta\cos(k_z z) \end{pmatrix} \tag{C.1}$$

If their were no metal but only air surrounding the devices, total internal reflection (TIR) would happen as explained in section 2.4. Taking into account the $\pi/2$ phase shift introduced by the TIR and neglecting the phase shift caused by the expansion of the electric field in the air, the electric field would be:

$$\mathbf{F}^d = 2F \exp\left(ik_x x - i\omega t\right) \begin{pmatrix} \cos\theta\cos(k_z z) \\ 0 \\ i\sin\theta\sin(k_z z) \end{pmatrix} \tag{C.2}$$

If we cover only $x\%$ of the device with metal, the light impinging through the facet with an angle θ, the resulting electric field can be estimated by:

$$\mathbf{F}^t = \mathbf{F}^m\sqrt{x} + \mathbf{F}^d\sqrt{1-x} \tag{C.3}$$

According to the polarization rule, only its component along the growth direction z can be absorbed. The power density of this component is:

$$\left|F_z^t\right|^2 = |2F\sin\theta|^2 \left|\cos(k_z z)\sqrt{x} + i\sin(k_z z)\sqrt{1-x}\right|^2 \tag{C.4}$$
$$= |2F\sin\theta|^2 \left(x\cos^2(k_z z) + (1-x)\sin^2(k_z z)\right) \tag{C.5}$$
$$= |2F\sin\theta|^2 \left(\sin^2(k_z z) + x\left(\cos^2(k_z z) - \sin^2(k_z z)\right)\right) \tag{C.6}$$
$$= |2F\sin\theta|^2 \left(\sin^2(k_z z) + x\left(1 - 2\sin^2(k_z z)\right)\right) \tag{C.7}$$
$$= |2F\sin\theta|^2 \left(\sin^2(k_z z)(1-2x) + x\right) \tag{C.8}$$
$$\tag{C.9}$$

C.2 Interpretation

The first variable is the light angle of incidence θ. When the light is shining perpendicularly to the device surface ($\theta = 0$) we verify that the z-component power density is going to zero. Hence no light is absorbed.
The second parameter is the percentage of the device covered with metal x. Three cases have to be distinguished:

1. $x > 50\%$, the metal occupy more than half the mesa surface.
2. $x = 50\%$, the metal occupy exactly than half the mesa surface.
3. $x < 50\%$, the metal occupy less than half the mesa surface.

In the first case, the power density is maximum at the top contact and decreases until it reaches a minimum. The behavior of the third case is opposite, the power density is minimum at the top contact and starts to increase while going further in the device. We note that the power density is periodic, of period $\lambda = \lambda_0/n$ (λ_0 is the wavelength is the vacuum). Examples are given in figure C and the variations of the power density depending on x are given in figure C.1. When we are in the intermediate case ($x = 50\%$), the term $\sin^2(k_z z)(1-2x)$ goes to 0 and the power density is then constant throughout the device.

z	0	$\lambda/4\cos\theta$	$\lambda/2\cos\theta$
$\lvert F_z^t \rvert^2$ when $x > 0.5$	$2xF^2$	$2(1-x)F^2$	$2xF^2$
$\lvert F_z^t \rvert^2$ when $x < 0.5$	$2xF^2$	$2(1-x)F^2$	$2xF^2$

Figure C.1: Variation of the power density through the device, $z = 0$ being the top contact

Appendix D

Fabrication

D.1 Fabrication and packaging

Devices with different mesa sizes have been fabricated. Each mesa are square and their rims are 200 μm , 400 μm , 600 μm , 800μm , 1 mm and 1.5 mm. The four smaller mesas are duplicated twice to optimize the wafer use. The relative positions of the mesas is represented in figure D.1 which is the mask used for their etching.

The wafer is first cleaved into pieces of around 2cm$\times$2cm by using a diamond scribe. A

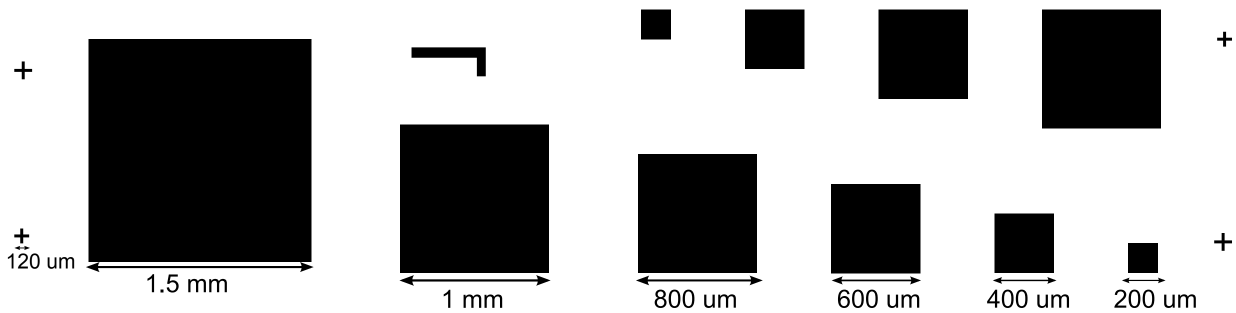

Figure D.1: Disposition of the devices in one bar

niche is made on the wafer side and a force is applied to cleave it. This piece will be used to make 3 rows of devices according to the mask pattern in appendix D.2. The procedure is described in more details in the process sheet in appendix D.3 and represented in figure D.2. We use a standard cleaning procedure on the piece (Acetone, Isopropanol and RIE). A first layer of photoresist is deposited by spin-coating and exposed. The device is plunged

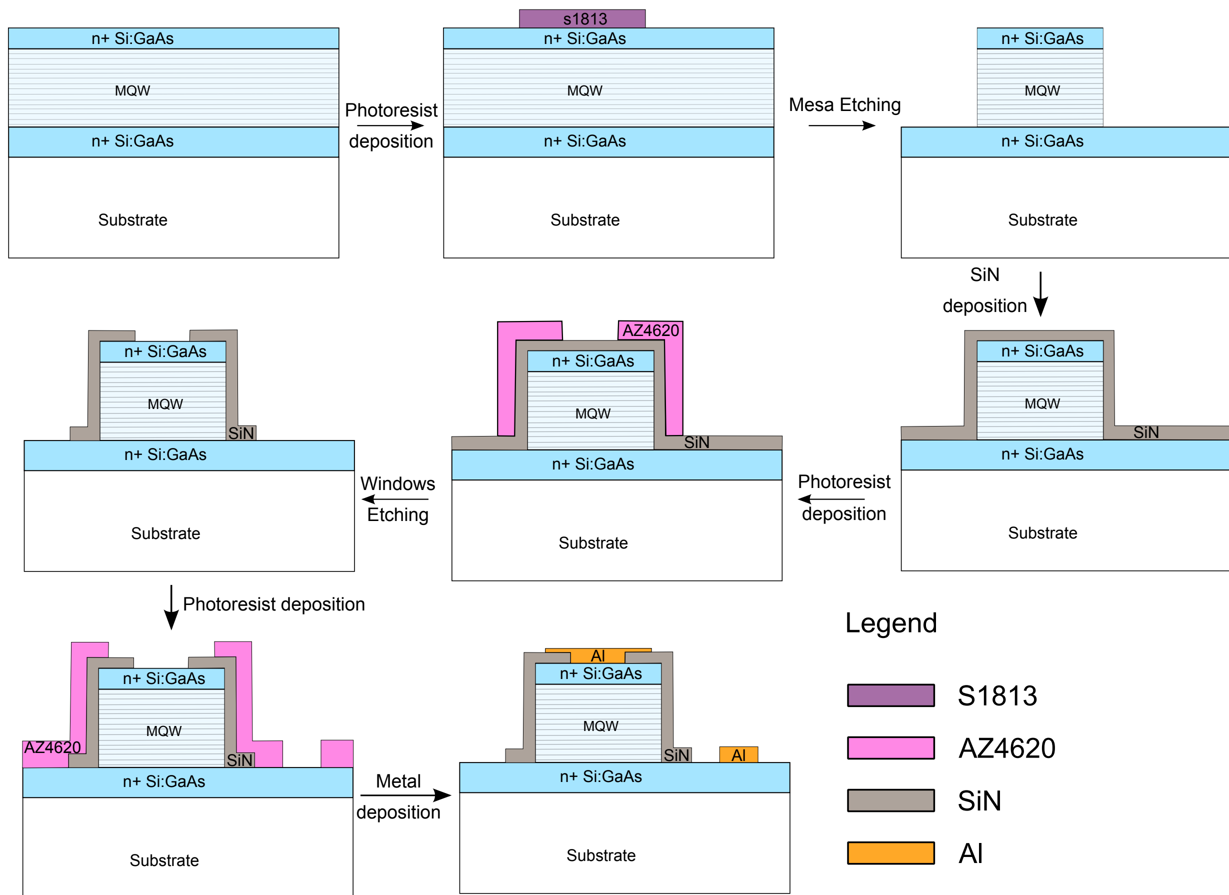

Figure D.2: Fabrication steps

in $H_2SO_4 : H_2O_2 : H_2O$ (piranha solution) to etch the areas of the device not covered by the photoresist down to the bottom highly doped layer and thus form the mesas. The etching rate has been measured and fluctuates between 220 and 390 nm/min for a piece in the center of the wafer after 3 minutes of etching. The overall rate value is 308 nm/min and the final value is 318 nm/min. The total depth etched is between 3.19 nm and 3.21 nm. Clean and sharp results are obtained as we can see on the microscope pictures D.3 and D.4 of the smallest features (alignment and identification marks).

The next step is to deposit a passivation layer of SiN, protect the side walls of the mesa with photoresist and etch the rest with CF_4/O_2 RIE. Finally, Aluminum bottom and top contacts are deposited at the same time by usual liftoff techniques. In appendix D.2, we show all the mask at our disposal. We have only one mask for the mesa etching and one

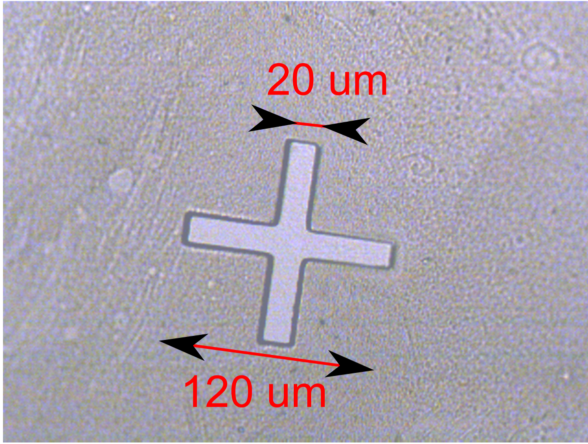

Figure D.3: Alignment mark after etching

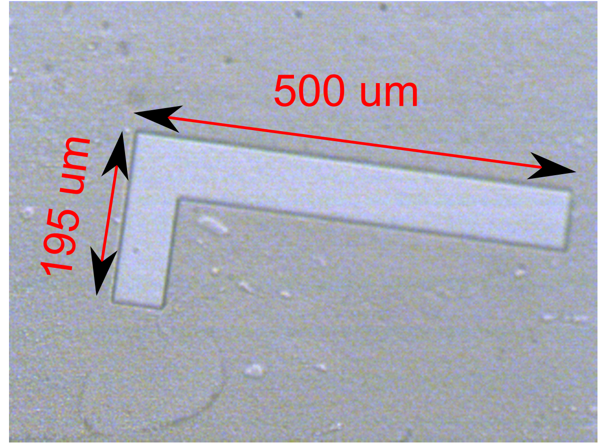

Figure D.4: Alignment mark after etching

for the SiN passivation layer. Nevertheless, we designed 5 masks for the metal contact deposition. Each of them produces a top contact with a mesa coverage varying from 50 to 90 % with a step of 10 % to experimentally confirm the discussion lead in section 2.4.
The packaging is separated in four steps: bar dicing, 45° facet polishing, mounting and wire-bounding. Those steps are synthesized in figure D.5. The 3 rows of devices are then

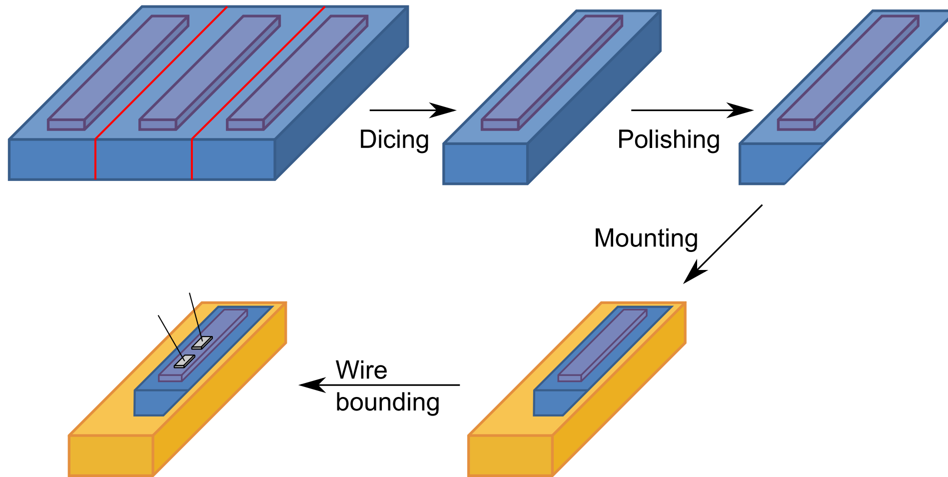

Figure D.5: Packaging steps

diced from each other by using a micromaterial process laser. The model we use is a LPFK Protolaser U3. The resulting cleaving is sharp but the facet we obtain is dirty

over $\approx 100\mu m$. Devices being $500\mu m$ away from the facet after cleaving, the dirty layer is consequently not in contact with the devices, far by $\approx 400\mu m$. The facet on which the light will impinge is then polish at 45° for each of these bars. A rectangular cuboid with one facet milled at 45° metallic sample holder has been realized for this procedure. The sample is glued with wax at the top edge of the holder angled facet and mounted into a sample holder. Hand-polishing is performed by hand by pressing the sample holder successively onto 600, 800 and 1200 grits sandpapers rotating at approximately 50 rpm on a standard lapping machine. The edge of the holder with the glued device is held in the opposite direction of the rotating sandpaper in order to avoid to loosen the device from the holder. Finally, $3\mu m$ diamond paste polishing is performed to reach an atomic-flat facet. The resulting polished sample is dismounted from the sample holder with an acetone bath at 50°C.
The sample is then mounted on a device carrier and connection is made with gold wire-bounding.
Two package holder and cold finger has been designed. The cold fingers are represented in figure D.7. On one hand, The first cold finger is inclined by 45°and is mounted for IV and absorption spectrum measurement. On the second hand, the other cold finger has an angle of 72°with the vertical and is used to measure the absorption spectrum with a TDS setup. In this setup, we look a the modification of a femtosecond signal after traveling through the studied sample. As a consequence, a window is made in the second cold finger to allow the light to go through the sample.

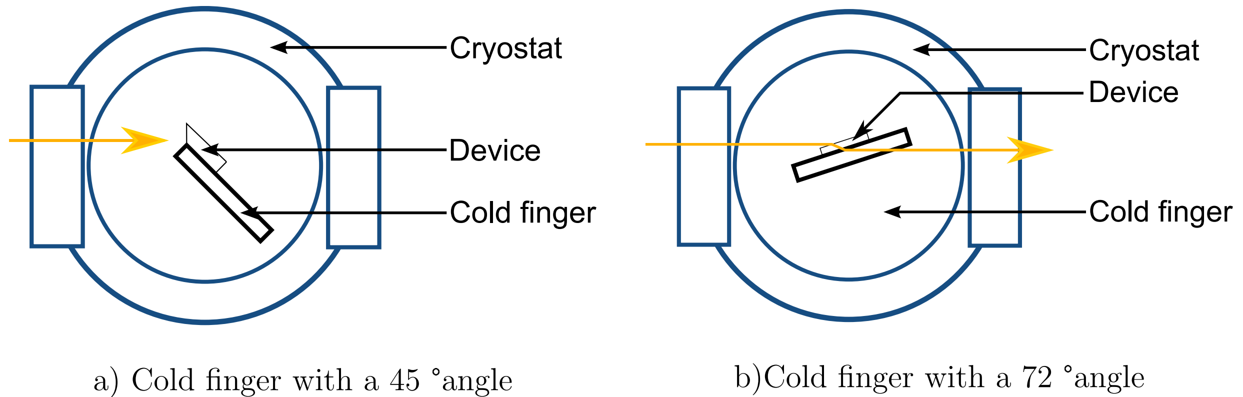

a) Cold finger with a 45 °angle

b)Cold finger with a 72 °angle

Figure D.6: Position of the cold finger and device in the cryostat

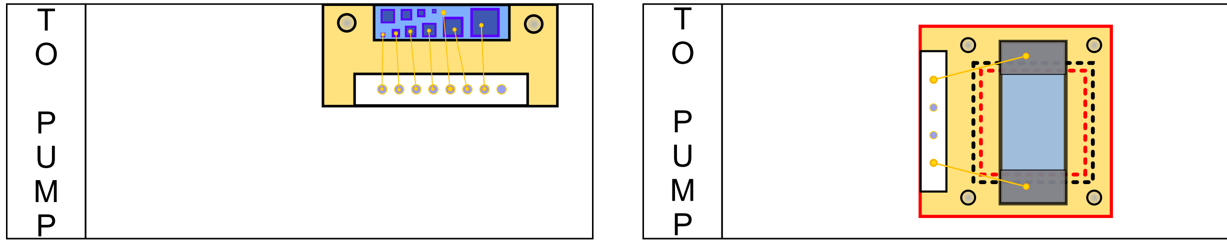

a) Cold finger tilted a 45 °angle b)Cold finger tilted a 72 °angle

Figure D.7: Top view of the cold fingers used for QWP characterization

D.2 Mask

We represent in figure D.8 the mask that we have used for the fabrication. The center pattern is used for the mesa etching, the center left pattern for the SiN passivation layer and the other patterns (apart from the bottom and top left pattern) for top metal deposition.

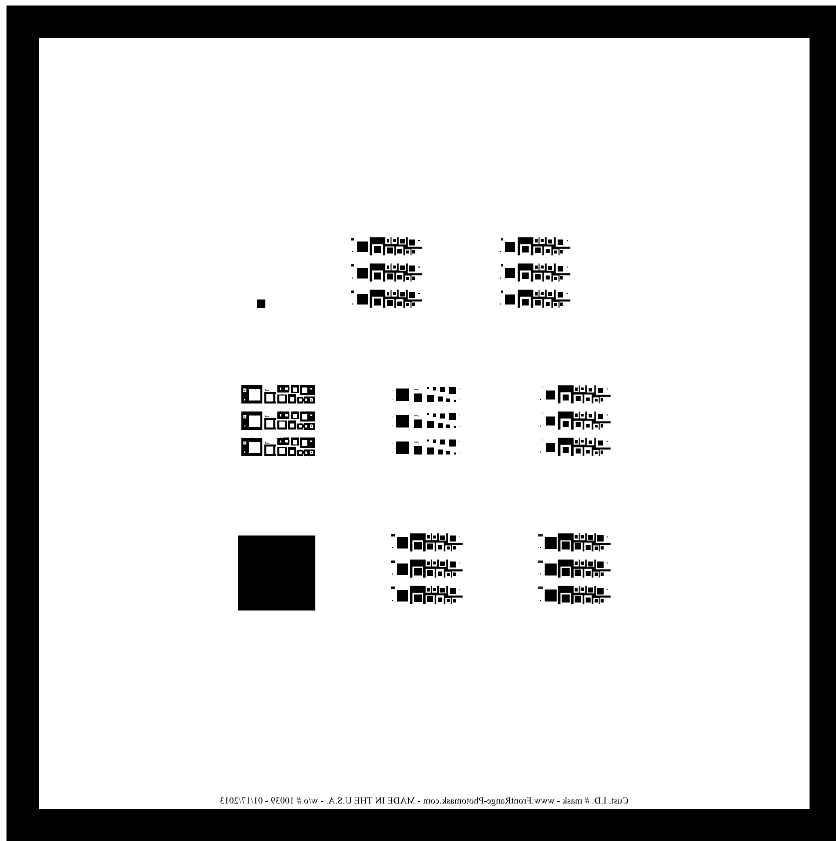

Figure D.8: Mask used for the fabrication

D.3 Process sheet

I. Wafer Structure

This table sum up all the parameters of the design

Parameter	Name	Value
Well width	L_w	195 Å
Barrier	L_b	951 Å
Electron sheet density	n_{2D}	$4 \times 10^{10}\ cm^{-2}$
Aluminum fraction	x	1.9%
Number of modules	N	23
Doping (over 10 nm)	N_D	$4 \times 10^{16}\ cm^{-3}$
Designed frequency	f	2.94 THz

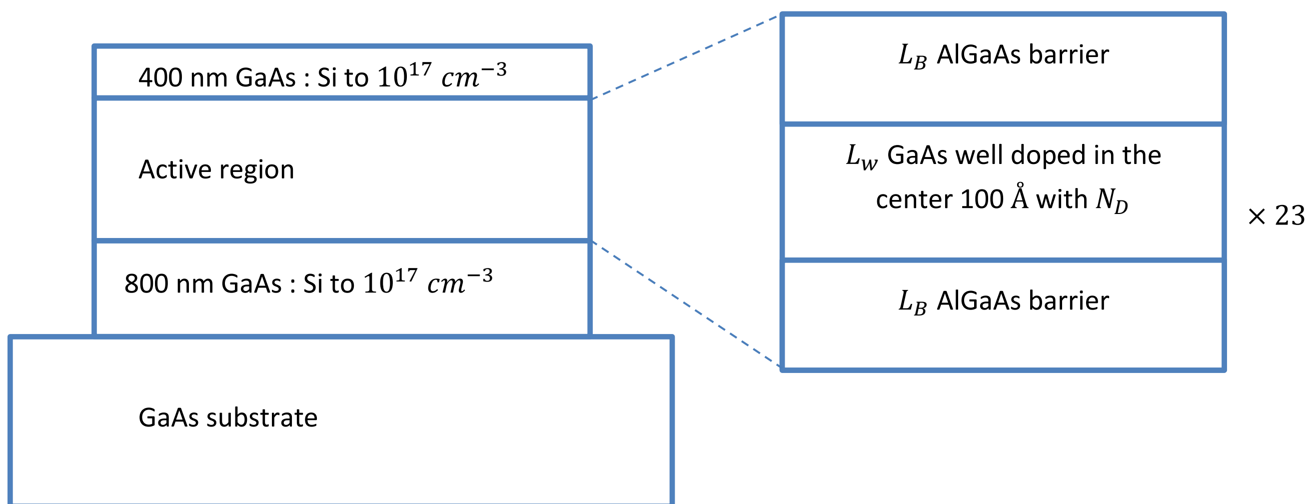

II. Device fabrication

No	Process Step	Date	Comments
1	**Initial clean (standard)**		
	Acetone, 5 min (50 °C)		
	Isopropanol, 5 min (50 °C)		
	DI rinse, repeat steps 1 and 2		
	Ni blow dry		
	O2 plasma RIE **2** min: 20-20-20 (set-pressure-power)		
	Ni blow		

2	**Photoresist spinning**		
	Ni blow		
	HDMS spin, 40 sec (500 rpm)		
	HDMS bake, 3 min (90 °C)		
	S1813 spin (3 steps, continuous):		
	5 sec (900 rpm)		
	1 min (4000 rpm)		~1.3 micron
	Pre-bake, 3 min (90 °C)		Acetone to remove poor film
3	**Exposure**		Mask 1 (mesas)
	Set soft contact, 36 micron alignment gap		
	Expose, 8 sec (364 nm)		
4	**Development**		
	MIF 314 developer, ~30 sec (watch for features)		
	Feature inspection		
	Post-bake, 5 min (110 °C)		Check the features
5	**Mesa wet etch**		
	Piranha is explosive and corrosive, extra safety steps: Email notification of all lab users, signs on doors Full face and hand protection, Perform during low-traffic hours Neutralize with KOH pellets, DO NOT STORE		
	H_2SO_4:H_2O_2:H_2O, 1:8:320, monitor every 30 sec until target depth of 3.2 micron		~300 nm/min into GaAs, will slow down and oscillate +/- 30%, monitor closely
6	**SiN deposition**		Passivation layer
	PECVD nitride deposition, 6000 A, (350 °C)		
7	**Photoresist spinning**		
	Ni blow		
	HDMS spin, 40 sec (500 rpm)		
	HDMS bake, 3 min (90 °C)		
	AZ 3312 spin (3 steps, continuous):		
	1 min (4000 rpm)		
	10 sec (500 rpm)		
	1 min (3000 rpm)		
	Pre-bake, 5 min (90 °C)		
8	**Exposure**		Mask 2 (nitride windows)

	Set soft contact, 36 micron alignment gap, align		
	Expose, 4 sec (364 nm)		
9	**Development**		
	AZ developer, ~30 sec (watch for features)		
	Feature inspection		
	Post-bake, 5 min (110 °C)		
10	**Window etching**		
	CF4/O2 plasma RIE, 10 min 15/5-40-75 (set-pressure-power)		
11	**Photoresist removal**		
	AZ developer, 5 min		Confirm with microscope
12	**Photoresist spinning**		
	Ni blow		
	HDMS spin, 40 sec (500 rpm)		
	HDMS bake, 3 min (90 °C)		
	AZ 3312 spin (3 steps, continuous):		
	1 min (4000 rpm)		
	10 sec (500 rpm)		
	1 min (3000 rpm		
	Pre-bake, 5 min (90 °C)		
13	**Exposure**		Mask 3 (metal contacts)
	Set soft contact, 36 micron alignment gap, align		
	Expose, 4 sec (364 nm)		
14	**Development**		
	AZ developer, ~30 sec (watch for features)		
	Feature inspection		
	Post-bake, 5 min (110 °C)		
15	**Metal deposition**		
	EB deposition of Al (450 nm)		
16	**Metal liftoff**		
	AZ developer, ~10 min		Confirm with microscope

References

[1] Masayoshi Tonouchi. Cutting-edge terahertz technology. *Nature photonics*, 1(2):97–105, 2007.

[2] Jason Sun, Kwong-Kit Choi, and Unchul Lee. Fabrication of pyramidal corrugated quantum well infrared photodetector focal plane arrays by inductively coupled plasma etching with bcl3/ar. *Journal of Micro/Nanolithography, MEMS, and MOEMS*, 11(4):043003–1–043003–4, 2012.

[3] H. Malmberg. Infrared spectroscopy in failure analysis. In *Reliability, Maintainability and Safety (ICRMS), 2011 9th International Conference on*, pages 1021–1025, 2011.

[4] David Trnqvist Fredrik Gustafsson Per Skoglar, Umut Orguner. Pedestrian tracking with an infrared sensor using road network information, 2012.

[5] Jane Wang, King-Jen Chang, Chin-Yu Chen, Kuo-Liong Chien, Yuh-Show Tsai, Yuh-Ming Wu, Yu-Chuan Teng, Tiffany Ting-Fang Shih, et al. Evaluation of the diagnostic performance of infrared imaging of the breast: a preliminary study. *Biomedical engineering online*, 9(3):1–10, 2010.

[6] RM Woodward, VP Wallace, DD Arnone, EH Linfield, and M Pepper. Terahertz pulsed imaging of skin cancer in the time and frequency domain. *Journal of Biological Physics*, 29(2-3):257–259, 2003.

[7] Joo-Hiuk Son. Terahertz electromagnetic interactions with biological matter and their applications. *Journal of Applied Physics*, 105(10):102033, 2009.

[8] E Pickwell and VP Wallace. Biomedical applications of terahertz technology. *Journal of Physics D: Applied Physics*, 39(17):R301, 2006.

[9] Christian Jansen, Steffen Wietzke, Ole Peters, Maik Scheller, Nico Vieweg, Mohammed Salhi, Norman Krumbholz, Christian Jördens, Thomas Hochrein, and Martin Koch. Terahertz imaging: applications and perspectives. *Appl. Opt.*, 49(19):E48–E57, Jul 2010.

[10] MJ Fice, E Rouvalis, L Ponnampalam, CC Renaud, and AJ Seeds. Telecommunications technology-based terahertz sources. *Electronics Letters*, 46(26):28–31, 2010.

[11] M Bolduc, L Marchese, B Tremblay, M Doucet, M Terroux, H Oulachgar, L Le Noc, C Alain, H Jerominek, and A Bergeron. Video-rate thz imaging using a microbolometer-based camera. In *Infrared Millimeter and Terahertz Waves (IRMMW-THz), 2010 35th International Conference on*, pages 1–2. IEEE, 2010.

[12] Thomas G Phillips and Jocelyn Keene. Submillimeter astronomy (heterodyne spectroscopy). *Proceedings of the IEEE*, 80(11):1662–1678, 1992.

[13] Peter H Siegel. Terahertz technology. *Microwave Theory and Techniques, IEEE Transactions on*, 50(3):910–928, 2002.

[14] Phil McKenna. Terahertz video transfer is foretaste of future wireless, March 2008. url: http://www.newscientist.com/article/dn13500.

[15] Brian J. Drouin, Shanshan Yu, John C. Pearson, and Harshal Gupta. Terahertz spectroscopy for space applications: 2.52.7 thz spectra of hd, {H2O} and {NH3}. *Journal of Molecular Structure*, 1006(13):2 – 12, 2011. ¡ce:title¿STRUCTURAL {APPLICATIONS} {OF} {TERAHERTZ} SPECTROSCOPY¡/ce:title¿.

[16] D. Saeedkia. *Handbook of Terahertz Technology for Imaging, Sensing, and Communications*. Woodhead Publishing Series in Electronic and Optical Materials. Woodhead Publishing Limited, 2013.

[17] INO. Irxcam-thz, camera module, June 2010. http://www.ino.ca/Docs/Documents/publications/techniques/Bolometres-module-ir/COMM-100128_FICHE%20TECH_IRXCAM-THz_EN.pdf.

[18] Marcel JE Golay. A pneumatic infra-red detector. *Review of Scientific Instruments*, 18(5):357–362, 1947.

[19] AG Chynoweth. Dynamic method for measuring the pyroelectric effect with special reference to barium titanate. *Journal of applied physics*, 27(1):78–84, 1956.

[20] J Cooper. A fast-response pyroelectric thermal detector. *Journal of Scientific Instruments*, 39(9):467, 1962.

[21] Irmantas Kašalynas, Aurèle JL Adam, Tjeerd O Klaassen, Niels J Hovenier, Grégory Pandraud, Ventzeslav P Iordanov, and Pasqualina M Sarro. Some properties of a room temperature thz detection array. In *Advanced Optical Materials, Technologies, and Devices*, pages 65960J–65960J. International Society for Optics and Photonics, 2006.

[22] Neal Erickson. A fast, very sensitive calorimetric power meter for millimeter to submillimeter wavelengths. In *Thirteenth international symposium on space terahertz technology, harvard university*, 2002.

[23] MA Kinch. Compensated silicon-impurity conduction bolometer. *Journal of Applied Physics*, 42(13):5861–5863, 1971.

[24] HT Nguyen, P Ringold, PAR Ade, J Battle, JW Beeman, JJ Bock, SC Elliott, PC Hargrave, B Schulz, AD Turner, et al. A report on laboratory performance of the bolometric detector arrays for spire/hso: Part ii. In *Astronomical Telescopes and Instrumentation*, pages 627518–627518. International Society for Optics and Photonics, 2006.

[25] Frank J Low. Low-temperature germanium bolometer. *JOSA*, 51(11):1300–1304, 1961.

[26] Adrian T Lee, Paul L Richards, Sae Woo Nam, Blas Cabrera, and KD Irwin. A superconducting bolometer with strong electrothermal feedback. *Applied Physics Letters*, 69(12):1801–1803, 1996.

[27] D Rutledge and S Schwarz. Planar multimode detector arrays for infrared and millimeter-wave applications. *Quantum Electronics, IEEE Journal of*, 17(3):407–414, 1981.

[28] Tien-Lai Hwang, SE Schwarz, and DB Rutledge. Microbolometers for infrared detection. *Applied Physics Letters*, 34(11):773–776, 1979.

[29] JW Beeman, WL Hansen, OD Dubon, and EE Haller. High performance antimony-doped germanium photoconductors. *Infrared physics & technology*, 37(7):715–721, 1996.

[30] SJ Fray and JFC Oliver. Photoconductive detector of radiation of wavelength greater than 50 μ. *Journal of Scientific Instruments*, 36(4):195, 1959.

[31] Mikio Fujiwara and Norihisa Hiromoto. Ge: Ga far-infrared photoconductor with a low ga concentration of 1 x 1014 cm-3. *Japanese journal of applied physics*, 36(part 1):4262–4266, 1997.

[32] WJ Moore and H Shenker. A high-detectivity gallium-doped germanium detector for the 40–120μ region. *Infrared Physics*, 5(3):99–106, 1965.

[33] NM Haegel, EE Haller, and PN Luke. Performance and materials aspects of ge: Be photoconductors. *International journal of infrared and millimeter waves*, 4(6):945–954, 1983.

[34] JR Sandercock. Energy exchange between hot carriers and the lattice in indium antimonide. *Proceedings of the Physical Society*, 86(6):1221, 1965.

[35] GE Stillman, CM Wolfe, and JO Dimmock. Semiconductors and semimetals. *Willardson and Beer (ed)*, 12:291, 1977.

[36] Jean Leotin. Far infrared photoconductive detectors. In *1986 Quebec Symposium*, pages 81–100. International Society for Optics and Photonics, 1986.

[37] Jeffrey W Beeman, Supriya Goyal, Lothar A Reichertz, and Eugene E Haller. Ion-implanted ge: B far-infrared blocked-impurity-band detectors. *Infrared Physics & Technology*, 51(1):60–65, 2007.

[38] F. Sizov and A. Rogalski. {THz} detectors. *Progress in Quantum Electronics*, 34(5):278 – 347, 2010.

[39] Erik Bründermann, Heinz-Wilhelm Hübers, and Maurice Fitzgerald Kimmitt. *Terahertz Techniques*. Springer, 2012.

[40] Créidhe M O'Sullivan, J Anthony Murphy, and Spiral Bound. Field guide to terahertz sources, detectors, and optics (spie press book). 2012.

[41] Lorenzo Romeo, Dominique Coquillant, Leonardo Viti, Daniele Ercolani, Lucia Sorba, Wojciech Knap, Alessandro Tredicucci, and Miriam S Vitiello. Room-temperature nanowire terahertz photodetectors. In *SPIE OPTO*, pages 86312E–86312E. International Society for Optics and Photonics, 2013.

[42] Tsuneya Ando, Alan B Fowler, and Frank Stern. Electronic properties of two-dimensional systems. *Reviews of Modern Physics*, 54:437–672, 1982.

[43] GA Sai-Halasz, LL Chang, J-M Welter, C-A Chang, and L Esaki. Optical absorption of $In_{1-x}Ga_xAs/GaSb_{1-y}As_y$ superlattices. *Solid State Communications*, 27(10):935–937, 1978.

[44] JS Smith, LC Chiu, S Margalit, A Yariv, and AY Cho. A new infrared detector using electron emission from multiple quantum wells. *Journal of Vacuum Science & Technology B: Microelectronics and Nanometer Structures*, 1(2):376–378, 1983.

[45] LC Chiu, JS Smith, S Margalit, A Yariv, and AY Cho. Application of internal photoemission from quantum-well and heterojunction superlattices to infrared photodetectors. *Infrared Physics*, 23(2):93–97, 1983.

[46] LC West and SJ Eglash. First observation of an extremely large-dipole infrared transition within the conduction band of a gaas quantum well. *Applied Physics Letters*, 46:1156, 1985.

[47] BF Levine, KK Choi, CG Bethea, J Walker, and RJ Malik. New 10 μm infrared detector using intersubband absorption in resonant tunneling gaalas superlattices. *Applied Physics Letters*, 50(16):1092–1094, 1987.

[48] BF Levine. Quantum-well infrared photodetectors. *Journal of applied physics*, 74(8):R1–R81, 1993.

[49] Antoni Rogalski. Quantum well photoconductors in infrared detector technology. *Journal of Applied Physics*, 93(8):4355–4391, 2003.

[50] Harald Schneider and Hui Chun Liu. Quantum well infrared photodetectors: physics and applications. 2007.

[51] KK Choi. *The physics of quantum well infrared photodetectors*, volume 7. World Scientific Publishing Company, 1997.

[52] LC Lenchyshyn, HC Liu, M Buchanan, and ZR Wasilewski. An asymmetric quantum well infrared photodetector with voltage-tunable narrow and broad-band response. *Journal of applied physics*, 79(6):3307–3311, 1996.

[53] A Kastalsky, T Duffield, SJ Allen, and J Harbison. Photovoltaic detection of infrared light in a gaas/algaas superlattice. *Applied physics letters*, 52(16):1320–1322, 1988.

[54] AR Ellis, Amlan Majumdar, KK Choi, JL Reno, and DC Tsui. Binary superlattice quantum-well infrared photodetectors for long-wavelength broadband detection. *Applied physics letters*, 84(25):5127–5129, 2004.

[55] Jung-Hee Lee, Sheng S Li, MZ Tidrow, WK Liu, and K Bacher. Quantum-well infrared photodetectors with digital graded superlattice barrier for long-wavelength and broadband detection. *Applied physics letters*, 75(20):3207–3209, 1999.

[56] E Luna, M Hopkinson, JM Ulloa, A Guzman, and E Munoz. Dilute nitride based double-barrier quantum-well infrared photodetector operating in the near infrared. *Applied physics letters*, 83(15):3111–3113, 2003.

[57] BS Ma, WJ Fan, YX Dang, WK Cheah, WK Loke, W Liu, DS Li, SF Yoon, DH Zhang, H Wang, et al. Gainnas double-barrier quantum well infrared photodetector with the photodetection at¡ equation¿ 1.24¡ span style=. *Applied Physics Letters*, 91(5):051102–051102, 2007.

[58] Hi Schneider, C Schonbein, M Walther, K Schwarz, J Fleissner, and P Koidl. Photovoltaic quantum well infrared photodetectors: The four-zone scheme. *Applied physics letters*, 71(2):246–248, 1997.

[59] Robert Rehm1a, Martin Walthera, Joachim Fleißnera, Johannes Schmitza, Johann Zieglerb, Wolfgang Cabanskib, and Rainer Breiterb. Bispectral thermal imaging with quantum well infrared photodetectors and inas/gasb type-ii superlattices. In *Proc. of SPIE Vol*, volume 6206, pages 62060Y–1, 2006.

[60] Laure Gendron, M Carras, A Huynh, V Ortiz, C Koeniguer, and V Berger. Quantum cascade photodetector. *Applied physics letters*, 85(14):2824–2826, 2004.

[61] A Vardi, G Bahir, F Guillot, C Bougerol, E Monroy, SE Schacham, M Tchernycheva, and FH Julien. Near infrared quantum cascade detector in gan/ algan/ aln heterostructures. *Applied Physics Letters*, 92:011112, 2008.

[62] Fabrizio R Giorgetta, Esther Baumann, Marcel Graf, Quankui Yang, Christian Manz, Klaus Kohler, Harvey E Beere, David A Ritchie, Edmund Linfield, Alexander G Davies, et al. Quantum cascade detectors. *Quantum Electronics, IEEE Journal of*, 45(8):1039–1052, 2009.

[63] HC Liu, CY Song, AJ SpringThorpe, and JC Cao. Terahertz quantum-well photodetector. *Applied physics letters*, 84(20):4068–4070, 2004.

[64] Marcel Graf, Giacomo Scalari, Daniel Hofstetter, Jerome Faist, Harvey Beere, Edmund Linfield, David Ritchie, and Giles Davies. Terahertz range quantum well infrared photodetector. *Applied Physics Letters*, 84(4):475–477, 2004.

[65] Giacomo Scalari, Marcel Graf, Daniel Hofstetter, Jérôme Faist, Harvey Beere, and David Ritchie. A thz quantum cascade detector in a strong perpendicular magnetic field. *Semiconductor science and technology*, 21(12):1743, 2006.

[66] JC Cao, HC Liu, et al. Chapter 4 terahertz semiconductor quantum well photodetectors. *Semiconductors and Semimetals*, 84:195, 2011.

[67] X Guo, J Cao, R Zhang, Z Tan, and H Liu. Recent progress in terahertz quantum-well photodetectors. 2013.

[68] Xuguang Guo, Rong Zhang, Juncheng Cao, and Huichun Liu. Surface plasmon-enhanced absorption in metal grating coupled terahertz quantum well photodetectors. *Quantum Electronics, IEEE Journal of*, 48(9):1113–1119, 2012.

[69] Xuguang Guo, Rong Zhang, Juncheng Cao, and Huichun Liu. Numerical study on metal cavity couplers for terahertz quantum-well photodetectors. *Quantum Electronics, IEEE Journal of*, 48(5):728–733, 2012.

[70] F Wu, W Tian, WY Yan, J Zhang, SC Sun, JN Dai, YY Fang, ZH Wu, and CQ Chen. Terahertz intersubband transition in gan/algan step quantum well. *Journal of Applied Physics*, 113(15):154505–154505, 2013.

[71] Daniel Feezell, Yagya Sharma, and Sanjay Krishna. Optical properties of nonpolar iii-nitrides for intersubband photodetectors. *Journal of Applied Physics*, 113(13):133103–133103, 2013.

[72] T Zhou, R Zhang, XG Guo, ZY Tan, Z Chen, JC Cao, and HC Liu. Terahertz imaging with quantum-well photodetectors. *Photonics Technology Letters, IEEE*, 24(13):1109–1111, 2012.

[73] ZHOU Tao, ZHANG Rong, GUO Xu-Guang, TAN Zhi-Yong, and CAO Jun-Cheng. Thz imaging using a quantum-well photodetector with background limited performance. *Chinese Physics Letters*, 29(10):104202, 2012.

[74] PD Grant, SR Laframboise, R Dudek, M Graf, A Bezinger, and HC Liu. Terahertz free space communications demonstration with quantum cascade laser and quantum well photodetector. *Electronics letters*, 45(18):952–954, 2009.

[75] Z Chen, ZY Tan, YJ Han, R Zhang, XG Guo, H Li, JC Cao, and HC Liu. Wireless communication demonstration at 4.1 thz using quantum cascade laser and quantum well photodetector. *Electronics letters*, 47(17):1002–1004, 2011.

[76] H Schneider, C Mermelstein, R Rehm, C Schönbein, A Saar, and M Walther. Optically induced electric-field domains by bound-to-continuum transitions in n-type multiple quantum wells. *Physical Review B*, 57(24):R15096–R15099, 1998.

[77] M Ryzhii, V Ryzhii, R Suris, and C Hamaguchi. Periodic electric-field domains in optically excited multiple-quantum-well structures. *Physical Review B*, 61(4):2742, 2000.

[78] HC Liu, CY Song, AJ SpringThorpe, and JC Cao. Terahertz quantum-well photodetectors. *Infrared physics & technology*, 47(1):169–174, 2005.

[79] H Luo, HC Liu, CY Song, and ZR Wasilewski. Background-limited terahertz quantum-well photodetector. *Applied Physics Letters*, 86(23):231103–231103, 2005.

[80] ZY Tan, XG Guo, JC Cao, H Li, X Wang, SL Feng, ZR Wasilewski, and HC Liu. Temperature dependence of current–voltage characteristics of terahertz quantum-well photodetectors. *Semiconductor Science and Technology*, 24(11):115014, 2009.

[81] Harald Schneider and Hui Chun Liu. Quantum well infrared photodetectors: physics and applications. 2007.

[82] Paul Harrison. *Quantum wells, wires and dots: theoretical and computational physics of semiconductor nanostructures*. John Wiley & Sons, 2005.

[83] Virginie Trinité, Ezzeddine Ouerghemmi, Vincent Guériaux, Mathieu Carras, Alexandru Nedelcu, Eric Costard, and Julien Nagle. Modelling of electronic transport in Quantum Well Infrared Photodetectors. *Infrared Physics & Technology*, 54(3):204–208, May 2011.

[84] DF Nelson, RC Miller, and DA Kleinman. Band nonparabolicity effects in semiconductor quantum wells. *Physical Review B*, 35(14):7770, 1987.

[85] KH Yoo, LR Ram-Mohan, and DF Nelson. Effect of nonparabolicity in gaas/ga_ {1-x} al_ {x} as semiconductor quantum wells. *Physical Review B*, 39(17):12808, 1989.

[86] Lars Hedin and BI Lundqvist. Explicit local exchange-correlation potentials. *Journal of Physics C: Solid state physics*, 4(14):2064, 1971.

[87] Walter L Bloss. Effects of hartree, exchange, and correlation energy on intersubband transitions. *Journal of Applied Physics*, 66(8):3639–3642, 1989.

[88] Marcel Graf, Emmanuel Dupont, Hui Luo, Soufien Haffouz, Zbig R Wasilewski, Anthony J Spring Thorpe, Dayan Ban, and HC Liu. Terahertz quantum well infrared detectors. *Infrared Physics & Technology*, 52(6):289–293, 2009.

[89] Shun Lien Chuang et al. Physics of optoelectronic devices. 1995.

[90] Dong Pan, Elias Towe, and Steve Kennerly. Normal-incidence intersubband (In, Ga)As/GaAs quantum dot infrared photodetectors. *Applied Physics Letters*, 73(14):1937, 1998.

[91] Frank Szmulowicz and Gail J Brown. Calculation and photoresponse measurement of the bound-to-continuum infrared absorption in p-type GaAs/Al_xGa{1-x}As quantum wells. 51(19), 1995.

[92] Larry S Yu and Sheng S Li. A metal grating coupled bound-to-miniband transition gaas multiquantum well/superlattice infrared detector. *Applied physics letters*, 59(11):1332–1334, 1991.

[93] CP Lee, KH Chang, and KL Tsai. Quantum well infrared photodetectors with biperiodic grating couplers. *Applied physics letters*, 61(20):2437–2439, 1992.

[94] Alfredo De Rossi, Eric Costard, Nicolas Guerineau, and Sylvain Rommeluere. Effect of finite pixel size on optical coupling in qwips. *Infrared physics & technology*, 44(5):325–330, 2003.

[95] JY Andersson, L Lundqvist, and ZF Paska. Quantum efficiency enhancement of algaas/gaas quantum well infrared detectors using a waveguide with a grating coupler. *Applied physics letters*, 58(20):2264–2266, 1991.

[96] Heinz Raether. *Surface plasmons on smooth surfaces*. Springer, 1988.

[97] Dror Sarid and William Challener. *Modern introduction to surface plasmons: theory, Mathematica modeling, and applications*. Cambridge University Press, 2010.

[98] Kwong-Kit Choi, David P Forrai, Darrel W Endres, and Jason Sun. Corrugated quantum-well infrared photodetector focal plane arrays. *Quantum Electronics, IEEE Journal of*, 45(10):1255–1264, 2009.

[99] H Schneider, C Schonbein, M Walther, P Koidl, and G Weimann. Influence of optical interference on quantum well infrared photodetectors in a 45 waveguide geometry. *Applied physics letters*, 74(1):16–18, 1999.

[100] Carlo Sirtori, Federico Capasso, Jérôme Faist, and Sandro Scandolo. Nonparabolicity and a sum rule associated with bound-to-bound and bound-to-continuum intersubband transitions in quantum wells. *Physical Review B*, 50(12):8663, 1994.

[101] Takeya Unuma, Teruyuki Takahashi, Takeshi Noda, Masahiro Yoshita, Hiroyuki Sakaki, Motoyoshi Baba, and Hidefumi Akiyama. Effects of interface roughness and phonon scattering on intersubband absorption linewidth in a gaas quantum well. *Applied Physics Letters*, 78(22):3448–3450, 2001.

[102] Takeya Unuma, Masahiro Yoshita, Takeshi Noda, Hiroyuki Sakaki, and Hidefumi Akiyama. Intersubband absorption linewidth in gaas quantum wells due to scattering by interface roughness, phonons, alloy disorder, and impurities. *Journal of applied physics*, 93(3):1586–1597, 2003.

[103] BF Levine, CG Bethea, G Hasnain, VO Shen, E Pelve, RR Abbott, and SJ Hsieh. High sensitivity low dark current 10 μm gaas quantum well infrared photodetectors. *Applied physics letters*, 56(9):851–853, 1990.

[104] Vaidya Nathan. Dark current in GaAs/$Ga_{1-x}Al_xAs$ quantum well infrared detectors. In *SPIE OPTO*, pages 86310T–86310T. International Society for Optics and Photonics, 2013.

[105] HC Liu, Hui Luo, Chun-ying Song, Zbig R Wasilewski, AJ SpringThorpe, and JC Cao. Terahertz quantum well photodetectors. *Selected Topics in Quantum Electronics, IEEE Journal of*, 14(2):374–377, 2008.

[106] VWL Chin, T Osotchan, MR Vaughan, TL Tansley, GJ Griffiths, and Z Kachwalla. Hall and drift mobilities in molecular beam epitaxial grown gaas. *Journal of electronic materials*, 22(11):1317–1321, 1993.

[107] W Walukiewicz, J Lagowski, and HC Gatos. Electron mobility in n-type gaas at 77 k: Determination of the compensation ratio. *Journal of Applied Physics*, 53:769, 1982.

[108] MS Kiledjian, JN Schulman, and KL Wang. Absorption in GaAs/$Ga_{1-x}Al_xAs$ quantum wells with resonant barriers for improved responsivity. *Physical Review B*, 44(11):5616, 1991.

[109] Alexandre Delga. *Du phénomène quantique au dispositif macroscopique, transport électronique dans les détecteurs inter-sousbandes.* PhD thesis, Université Paris-Diderot-Paris VII, 2012.

[110] Alexandre Delga, Laetitia Doyennette, Vincent Berger, Mathieu Carras, Virginie Trinité, and Alexandru Nedelcu. Performances of quantum cascade detectors. *Infrared Physics & Technology*, 2012.

[111] Simon Ferré, Seyed Ghasem Razavipour, Chao Xu, and Dayan Ban. Many-body effects in terahertz quantum well infrared photodetectors. In *CLEO: QELS_Fundamental Science*. Optical Society of America, 2013.

[112] Simon Ferré, Seyed Ghasem Razavipour, and Dayan Ban. Terahertz quantum well photodetectors with improved designs by exploiting many-body effects. Accepted by Applied Physics Letters, to be published, 2013.

[113] VD Jovanović, P Harrison, Z Ikonić, and D Indjin. A microscopic model of quantum well infrared photodetectors (qwip). *Infrared physics & technology*, 47(1):3–8, 2005.

[114] VD Jovanović, P Harrison, Z Ikonić, and D Indjin. Modelling and simulation of electronic and optical responses of quantum well infrared photodetectors (qwips). *Journal of Physics D: Applied Physics*, 39(9):1773, 2006.